Battery Electrode Properties of Quinone and Halogen Molecules Encapsulated in Single-walled Carbon Nanotubes

単層カーボンナノチューブに内包されたキノンおよびハロゲン分子の電池電極特性

2019

Canghao Li

Battery Electrode Properties of Quinone and Halogen Molecules Encapsulated in Single-walled Carbon Nanotubes

単層カーボンナノチューブに内包されたキノンおよびハロゲン分子の電池電極特性

By

Canghao Li

李苍昊

Department of Life Science and Applied Chemistry

Nagoya Institute of Technology, Japan

January, 2019

ABSTRACT

The hollow space inside a single-walled carbon nanotube (SWCNT) gives rise to a very unique adsorption field as the surface potentials from all inner walls overlap. The encapsulated molecules are stabilized by the above-mentioned strong adsorption field of SWCNTs. This stabilizing effect of SWCNTs can be used to develop new battery electrode active materials. Previous studies revealed that molecules that have high potential as electrode materials but easily dissolve in the electrolyte and have low conductivity, work as good electrode active materials when encapsulated in SWCNTs.

Chapter 2 explores the reason why polyiodide ions encapsulated in SWCNTs drastically improve the electric conductivity and the water dispersibility of SWCNTs at low temperature, through performing in situ Raman measurements on polyiodide ions encapsulated in three kinds of SWCNTs of different mean tube diameters under low temperature down to -100ºC. It was found that for all the three samples, the Raman peak intensities of polyiodide ions increase, and the G-band peak position of SWCNTs shifts toward higher wavenumber side with decreasing temperature. It means that the charge transfer from SWCNTs to the encapsulated iodine molecules increased with decreasing temperature and that the hole doping level of SWCNTs increased at low temperature. Furthermore, the Raman peak profiles drastically changed with temperature for polyiodide ions encapsulated in the SWCNT sample having the largest mean tube diameter of 2.5 nm. The change indicates the structural transformation of polyiodide ions in SWCNTs. These experimental results can be explained by the promotion of chain-like polyiodide ion formation at low temperature. It was discussed with the control experiment using amylose, that the promotion of the polyiodide ion formation at low temperature is characteristic for iodine molecules encapsulated in SWCNTs.

In addition, an electrolyte redox electrochemical capacitor (EREC) using the redox reaction of bromide ions in SWCNTs was demonstrated. The maximum cell voltage of Br EREC increased up to about 1.5 V without oxygen evolution. The energy density of EREC was greatly improved by using the redox reaction of bromide ions instead of iodide ions used in a previous work. It was found by monitoring the capacitance retention that SWCNT electrode can firmly hold the inserted Br molecules. The structure and insertion site of the Br molecules inserted in SWCNTs was also investigated by Raman and XRD measurements. Raman measurements revealed the existence of $(Br_2)_n$ chain-like molecules and Br_3^- ions. Br molecules are likely to occupy the triangular lattice space of SWCNT bundles, because the diffraction lines of SWCNT bundle structure disappeared after Br insertion.

In chapter 3, Li and Na ion charge–discharge experiments of 9,10-phenanthrene quinone (PhQ) molecules encapsulated in SWCNTs with mean tube diameters of 1.5 and 2.5 nm were performed at room temperature and also at low temperatures. The Na ion reversible capacity of PhQ encapsulated in the larger diameter SWCNTs, measured at 0°C, remained as high as that measured at room temperature (RT), while the capacity of PhQ in the smaller diameter SWCNTs at 0°C was about a half of that at RT. The diameter dependence of the capacity should be attributed to the difference in the interactions between the encapsulated PhQ molecules and the host SWCNTs, which was revealed by Raman peak profile analysis. Charge-transfer reaction from metallic tubes to PhQ molecules encapsulated in the smaller diameter SWCNTs was detected by Raman measurements. The electrostatic interaction between charged SWCNTs and PhQ molecules, induced by the charge transfer reaction, would partly contribute to the stabilization of PhQ molecules in the smaller diameter SWCNTs, while only van der Waals interaction stabilizes PhQ molecules in the larger diameter SWCNTs. The difference in the stability was confirmed by thermogravimetric (TG), X-ray photoelectron spectroscopy (XPS), and Raman measurements. Charge–discharge

curves of PhQ encapsulated in SWCNTs were also discussed based on the stability difference.

In chapter 4, 9,10-anthraquinone (AQ) and PhQ were grafted onto two kinds of SWCNTs samples having different mean tube diameters by diazo coupling reaction. The structural details of PhQ grafted SWCNT (PhQ/SWCNT) samples were analyzed by XRD and Raman measurements. It was discussed that a few nanometer-thick layer of polymerized PhQs covers the outside of SWCNT bundles. The obtained PhQ/SWCNT samples worked very well as electrodes for lithium-ion battery (LIB) and sodium-ion battery (SIB), not only at room temperature but also at 0°C. It should be noted that the cycle performance of PhQ/SWCNT electrode was much better than that of PhQ encapsulated in SWCNT (PhQ@SWCNT). The molecular base reaction energies were calculated by DFT calculations to gain qualitative insight into the observed discharge potentials of PhQ/SWCNT electrode.

Finally, in chapter 5, a new-concept aqueous electrolyte secondary battery was developed by combining redox reactions of iodide ions in SWCNTs and alkali metal ions with quinone molecules. The new-concept battery consisting only of abundant elements utilizes the fast ion movements of both the cation and anion in a safe aqueous-electrolyte medium. AQ and PhQ were used as active quinone molecules. Both redox reactions of the cation and anion of an alkali metal halide aqueous electrolyte were investigated by electrochemical measurements, such as cyclic voltammetry and chronopotentiometry. The redox reaction of iodide ion was observed by chronopotentiometry, revealing a very flat charge/discharge potential plateau at about 0.45 V vs. Ag/AgCl. On the other hand, PhQ redox reactions showed a gradient potential plateau. It was also found that the discharge plateau potential of PhQ electrode measured with NaI aqueous electrolyte is about 0.1 V lower than that with LiI.

ACKNOWLEDGEMENT

I start to convey my gratitude to all the people who kindly provided me with help and guidance throughout the course of conducting this study.

I wish to express my sincerest gratitude my supervisor, **Professor Shinji Kawasaki**, for accept me as a member of research group and providing me with guidance and encouragement, which not only ensured successful completion of my research work but also give me a positive and novel living experience in Japan.

I would like to present my utmost appreciation to my teacher, **Dr. Yosuke Ishii**, for his continuing scientific guidance and advice. I am also grateful to him for introducing me to various aspects of Japanese culture, history and society, which enriched my knowledge and understanding of Japan, and deepened my appreciation of Japanese culture.

I thank for the operators at the **Instrument and Research Technology center** for their valuable assistance in the analysis of sample used in this study.

I express my gratitude to **Kawasaki research group members** for their kindly help.

Finally, I express my deep appreciation to my family for their constant assistances and encouragement.

TABLE OF CONTENTS

LIST OF FIGURES

CHAPTER 1

General Introduction

1.1 Electrochemical Energy Storage Devices

1.1.1 Lithium ion battery

1.1.1.1 Overview

Lithium-ion secondary batteries (LIBs) were commercialized by SONY in 1991 and developed rapidly in recent years [1]. Benefiting from the highest energy density among other successful rechargeable batteries like Nickel metal hydride battery, Lead acid battery and other traditional batteries, LIBs have been used as the major power source in portable electric devices such as mobile phone, portable computer [2,3]. However, with the development of new electric vehicles (EVs) in recent years, it is becoming increasingly difficult for commonly used LIBs to meet demand, due to demerits [4-6].

LIBs include a cathode, an anode, an electrolyte and a separator. During the discharge process, lithium ions are extracted from the anode material to pass through the separator between the anode and cathode, then be inserted into the cathode material. At the same time, a flow of electrons from the anode to the cathode occurs through the external circuit. The opposite happens during the charge process. A typical LIBs is usually made with lithium cobaltate ($LiCoO_2$) as the cathode material and graphite as the anode material. The total reaction schemes are shown as follows:

$$2Li_{0.5}CoO_2 + Li^+ + e^- \leftrightharpoons LiCoO_2 \quad (1.1)$$

$$LiC_6 \leftrightharpoons C_6 + Li+ e^- \quad (1.2)$$

$$2Li_{0.5}CoO_2 + LiC_6 \leftrightharpoons 2LiCoO_2 + C_6 \quad (1.3)$$

Right arrows and left arrows represent the processes of discharge and charge. The theoretical capacity of graphite is calculated to be 372 mAh/g. On the other hand, $LiCoO_2$ cannot deeply release Li ion less than $Li_{0.5}CoO_2$ results in capacity fade. This capacity fade has been attributed to the structural distortions around x=0.5 in $Li_{1-x}CoO_2$. Therefore, the practical capacity is only 140 mAh/g, although the theoretical capacity is about 280 mAh/g.

Lithium ions move back and forth between the cathode and the anode, and there is no lithium metal produced in the whole process. Because of their working characteristics, lithium ion batteries are also called "Rocking-chair Batteries" [7]. Benefiting from this process, LIBs can be repeatedly charged and discharged for hundreds of times. Namely, LIBs own a very long cycle life. Unlike the traditional energy storage battery, LIBs use organic liquid as electrolyte. The organic electrolyte can safely operate at high voltage, and the average output voltage of LIBs is more than 3.6 V, which is three times greater than those of traditional energy storage batteries [8].

1.1.1.2 Cathode material

Layered lithium transition metal oxides represent the most successful category of cathode material. Their composition is expressed by the formula $LiMO_2$ (M: Mn, Co, and Ni), and they crystallize in a layered structure in which the Li^+ and M ions occupy the alternate (111) planes of the rock salt structure, to give a layer sequence of -O-Li-O-M- as shown in Fig. 1.1. The gaps between the MO_2 sheets allow the reversible extraction/insertion of lithium ions from/into the lithium planes and diffusion pathways. The Li ion extraction/insertion process can continue for hundreds of cycles whilst retaining a high energy density. Among these $LiMO_2$ materials, considerable research focused on $LiCoO_2$ because of its high energy density and good cycle performance [9].

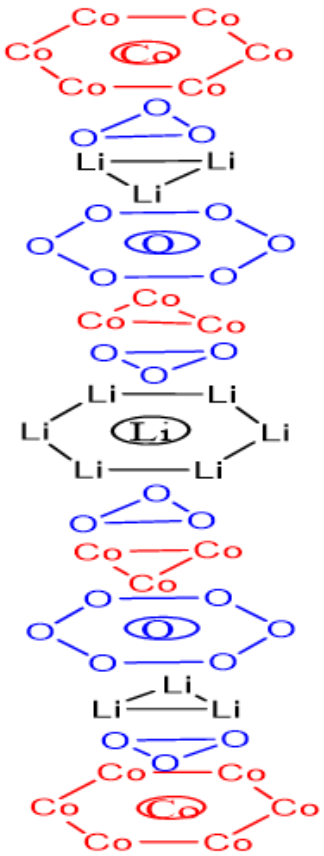

Fig. 1. 1: Structure picture of $LiCoO_2$.

$LiCoO_2$ exhibits many of the essential properties required for a reliable cathode material. The most important point is the potential of $LiCoO_2$ which is sufficiently high to guarantee a high energy density. Although lithium ion battery can work on high voltage, the organic electrolyte does not decompose even on this voltage. Furthermore, the Li extraction/insertion process causes only little structural change in Li_2CoO_2. Fig.1.1 shows the crystal structure of $LiCoO_2$ having layered structure. The excellent ordering structure should be synthesized at temperatures higher than 800℃. Li^+ and Co^+ ions arranged on the alternate (111) planes of the rock salt lattice.

1.1.2 Sodium ion battery

According to the U. S. Geological Survey report [10], lithium resources are mainly distributed in South America. The abundance of lithium in the earth crust is 0.002 %. With the rapid expansion in the EVs market, lithium resources will not be able to satisfy

the demand of EVs that need to be equipped with large-scale LIBs. Therefore, the development of alternative rechargeable batteries is required for the expansion in the production of EVs.

Sodium and lithium are located in the first main family of the Periodic Table and their properties have many similarities. The abundance of sodium in the earth crust is 2.83 %, far more than lithium, and it's widely distributed around the world. Sodium ion batteries (SIBs) should be one of the most promising candidates, because the risk of exhausting sodium resources can be ignored. Additionally, the price of sodium is much cheaper than lithium. If sodium-ion batteries can replace lithium-ion batteries, EVs will be widely used in the world. It is foreseeable that the price of EVs will be greatly reduced, thereby decreasing the use of fossil fuels.

There are still many challenges on the road towards the successful commercial rocking-chair type SIBs [11-13]. One of the reasons is that sodium ion hardly intercalates into graphite (which is the most common anode material used in LIBs), probably due to the larger ion size of sodium compared to that of lithium. The low sodium storage capacity hinders the use of graphite as anode of SIBs. Therefore, there is a need for other ion-storing strategies for SIBs electrode. The development of new anode material is one of these strategies.

1.1.3 Electric double layer capacitors

The electric double-layer capacitor (EDLC) is an electrochemical system that is used as energy storage system. EDLC can be described as an electrolyte (solid or liquid) that fills the space between two electrodes separated by an ion-conducting but electron-insulating membrane that prevents facing electrodes from contacting each other. Upon the application of electric potential on the one of the electrodes, the two opposite charges accumulate on the interface between the electrode and surrounding electrolyte. The electrode side has a real surface made of an electronically conducting material

(metal, semiconductor and carbon material). In the electrolyte phase, there exists a virtual surface that consists of charged particles traveling from the bulk of the electrolyte. By loading voltage to the EDLC, ions are drawn to the surface of the electrical double layer and the EDLC is charged. Conversely, they move away when discharging EDLC. This is how the EDLC is charged and discharged.

Compared to commercially available secondary batteries (e.g. Ni-MHs, LIBs), EDLCs have much higher power density and longer cycle life, which makes them suitable for occasions requiring high power delivery. Benefiting from their mechanism of charge storage, which is mainly a physical process, EDLCs are capable of fast delivery of stored charge without any limitations caused by the electrochemical kinetics found in batteries. On the other hand, the major drawback of EDLCs is their lower energy density, which is bound by the available surface area for ion adsorption, resulting in less energy stored per unit mass compared to that of rechargeable batteries [14].

1.2 Organic molecules as battery's electrode

Organic molecules such as quinones, disulfides, nitroxides, and hydrazides offer merits that are not easily available in inorganic compounds. They are potentially low in cost due to the absence of expensive rare-metal elements from their structure. Also, since most of them are lighter in molecular weight than existing cathode materials, they have higher theoretical Li ion storage capacity per unit weight. Therefore, organic molecules are fascinating materials as electrode materials for LIBs. With intercalation materials reaching their intrinsic limits, finding new electrode materials among inorganics becomes more and more difficult and a renaissance of organic electrodes is called upon. Among all organic electrode materials, radical compounds and conducting polymers have long been investigated [15, 16]. On the other hand, non-radical and non-polymeric organic molecules have recently been adapted not only to LIBs, but also to

sodium, magnesium, zinc ion batteries and air batteries. However, it is not very easy to use the organic molecules as electrode materials because most of them are easily dissoluble into organic electrolytes [17].

Quinone -hydroquinone couples are the examples of organic redox systems, and their electrochemical behavior has been studied in recent years. Usually one quinone molecule includes two carbonyl groups, and each carbonyl group undergoes reversible one-electron reduction to form a radical monoanion that can bind to a cation (H, Li, Na). PhQ that consists of only C, O and H, can store two Li ions per one molecule. The theoretical Li ion storage capacity of PhQ can be calculated to be 258 mAh/g. Therefore, PhQ would be a good candidate as a high-capacity and low-cost electrode material. However, the storage capacity of PhQ bulk sample greatly decreases with charge-discharge cycles because of the dissolution of PhQ molecules in organic electrolytes. In order to suppress the dissolution, several solutions have been attempted. The most effective method is polymerization [18]. In fact, organic polymers having redox active functional groups show superior cyclability compared to simple organic molecules. This method also suffers from the demerit of the observed practical capacity of organic polymers being usually much smaller than the theoretical capacity [19]. The poor electron conductivity and low ion accessibility might cause this deterioration of performance. To address that hypothesis, a single-walled carbon nanotubes (SWCNTs) encapsulation system has been used to attempt to solve the above-mentioned problems.

1.3 Single-walled carbon nanotubes encapsulation system

Since carbon nanotubes (CNTs) were discovered by Dr. Iijima of the Japanese electronics company (NEC) in 1991, they received extensive attention due to their excellent electrical conductivity, high surface area and good mechanical properties. CNTs are currently classified by the number of walls into multi-walled carbon

nanotubes, double-walled carbon nanotubes, and single-walled carbon nanotube (SWCNT). Among them, single-walled carbon nanotubes received much more attention, because of their light weight, easy modification, huge surface area, and also tunable porosity.

1.3.1 The basic structure of Single-walled carbon nanotubes

A SWCNT can be described as a graphene sheet that is rolled up into a continuous cylinder whose tip ideally terminates with a fullerene-like cap or hemisphere. Being one atom in thickness and about micron in length, a single-walled carbon nanotube has a high aspect ratio [104 – 105], due to which it can be classified as a one-dimensional nanostructured material [20]. Carbon atoms in SWCNTs are bound by sp^2 hybrid orbitals that allow them to form hexagons, and occasionally pentagon and heptagon units by in-plane σ bonding and out-of-plane π bonding. The tube curvature results in σ-π rehybridization or mixing, in which three σ bond are slightly out of plane [21]. That makes SWCNTs mechanically stronger, and electrically and thermally more conductive than graphite.

SWCNTs can be open-end or closed-end with caps of fullerene hemispheres, depending on the synthesis process. Each cap contains six pentagons and an appropriate number and placement of hexagons that are selected to fit perfectly into the long cylindrical section [20]. The process of rolling a graphene to form a SWCNT results in a cylinder with axial symmetry and a spiral conformation, called chirality. The tube chirality is the outcome of the different possible orientations of the six-membered carbon ring (hexagon) in the honeycomb lattice relative to the axis of the nanotube. It is the most important feature that defines SWCNTs, and separates them from other graphitic allotropes, because it reflects directly on their electronic structure and – as will be revealed for the first time in the next chapter – their electrochemical behavior as well. The manner of rolling the graphene sheet determines its chirality as will be

explained in more detail below. SWCNTs do not exist individually; rather, they tend to group into bundle-like structures because they are held together by the non-covalent Van der Waals forces to form a two-dimensional triangular lattice with a lattice constant of 1.7 nm, and an inter-tube separation of 0.315 nm at closest approach within a rope.

The unit cell of SWCNT is shown in Fig. 1.2 as the rectangle bound by two vectors, the chiral vector C_h and the translation vector T [22].

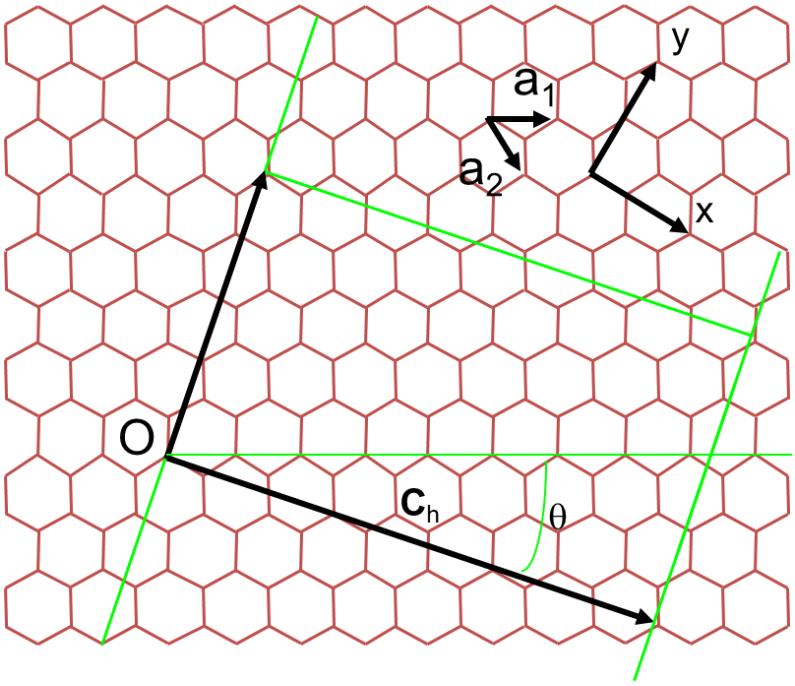

Fig. 1. 2: 2D graphene sheet shown along with the chiral vector that specifies the chiral nanotube and translation vector

The chiral vector C_h is described as the vector that joins two equivalent points on the original graphene lattice. The chiral vector is defined on the honeycomb lattice as follows:

$$C_h = na_1 + ma_2 \tag{1.4}$$

Where (n, m) are two integer indices $(n \geq m)$ that demote the number if unit vectors na_1 and ma_2 in the hexagonal honeycomb lattice contained in the vector, and taken respectively in the direction of a_1 and a_2, which are the unit cell base vectors of

the graphene sheet. The vector a_1 lies along the "zigzag", while vectors can be mathematically determined as follow:

$$a_1 = (\frac{\sqrt{3}}{2}a, \frac{a}{2}) \text{ , } a_2 = (\frac{\sqrt{3}}{2}a, -\frac{a}{2}) \quad (1.5)$$

Where a is the here $a = a_{c\text{-}c} \times \sqrt{3} = 2.46$ Å the lattice constant of the honeycomb lattice in the rolled graphene layer, where $a_{c\text{-}c}$ is the nearest-neighbor C-C distance (1.42 Å in SWCNT)

1.3.2 Single walled carbon nanotubes encapsulation system

As described in section 1.3.1, SWCNTs have a huge hollow space that gives rise to a very unique adsorption field as the surface potentials from all inner walls overlap. In 1998, Smith et al. reported the synthesis of C_{60} peapods in which C_{60} molecules exist in the hollow core of SWCNT in a very stable state, due to that unique adsorption field [23]. Since the discovery of C_{60} peapod, a variety of foreign molecules have been inserted inside SWCNTs. So far, fullerenes (e.g. C_{60}, C_{70}, metal encapsulated fullerenes), water [24], organic molecules (e.g. tetracyanoquinodimethane [25], carotene [26], coronene [27, 28]) and elemental molecules (e.g. iodine [29, 30], sulphur [31], phosphorus [32]) are known to have been encapsulated in SWCNTs. The encapsulated molecules are stabilized by the strong adsorption of the above-mentioned field inside SWCNTs. For example, C_{60} molecules in C_{60} peapods do not exit from the tubes to dissolve in organic solvents such as toluene, in which they usually dissolve very easily [33]. Recently, this stabilizing effect of SWCNTs has been used to develop new battery electrode active materials [34, 35]. Namely, molecules that have high potential as electrode materials but dissolve easily, can be used as electrode materials. In order to improve the electrochemical performance of these molecules, they are encapsulated inside the inner hollow core of SWCNTs. Interestingly, some of the molecules encapsulated in nanopores show unique structural and physicochemical properties different from their bulk forms. That difference is worth discussing in future chapters.

1.4 Aqueous electrolyte secondary battery

In order to ensure a wider spread of EVs, we have to solve some of the problems of LIBs. The major problems of LIBs are safety, cost and slow-charging speed. There have recently been frequent fire and explosion accidents involving LIBs, which researchers believe to be caused by the use of flammable organic electrolytes. On the other hand, organic electrolytes also cause LIBs to charge slowly. EVs usually need few hours to charge the battery, while normal cars only need a few minutes to fill up the fuel tank. Due to the ion mobility in organic electrolytes that is much lower than that in aqueous electrolytes, this time-consuming charging process of LIBs hinders the market growth of EVs.

Aqueous electrolyte rechargeable LIBs were promoted by some researchers as providing a possible long-term solution. However, there are shortcomings that still need to be overcome. An electric motive force (EMF) of LIBs higher than 3.5V leads to the high energy density. Compared to LIBs, the voltage of batteries which use aqueous electrolytes should be less than 2V, because aqueous electrolytes would decompose by such high EMF, making aqueous batteries incapable of delivering enough instantaneous power to drive the EVs. In order to overcome this flaw, aqueous electrolyte rechargeable lithium batteries need new electrode materials which can provide high current density.

The high cost of LIBs is another problem for the wider distribution of EVs. One of the main reasons behind the high cost is the use of rare metals such as Co, Ni, Li in LIBs. Therefore, and as pointed out above, the wider distribution of EVs requires us to solve the problems of safety, cost and slow-charging.

Here, I propose a new secondary battery having the following three specifications to solve the three problems mentioned above. (i) The new battery uses alkali metal halide aqueous electrolytes instead of the flammable organic electrolytes used in LIBs.

The use of aqueous electrolytes is not only much safer than organic electrolytes, but also advantageous to cost and fast-charging, because alkali metal halides such as NaCl, LiCl, NaI consist only of abundant elements, and the ion mobilities of both alkali metal ions and halogen ions in water are much faster than those in organic electrolytes. (ii) I used quinone molecules as a negative electrode in the new battery. Quinone molecules, which consist of only abundant elements, can catch/release alkali metal ions effectively. (iii) I used empty single-walled carbon nanotubes (SWCNTs) as the positive electrode. Halogen ions are oxidized inside the empty SWCNTs, and caught as a form of diatomic molecule inside SWCNTs [29, 30]. The redox reactions of halogen ions inside SWCNTs are much faster than the intercalation reaction in LIBs. By combining (i)-(iii), It is possible to develop safe, economical and fast-charging secondary batteries.

The energy density of the new aqueous electrolyte battery using quinone electrode is estimated to be about 50 Wh/kg which is much smaller than that of LIBs, because the EMF obtained by the combinations of the quinone electrode and iodine electrode would be very small (< 0.5 V). However, it is possible to improve the energy density of the new battery by developing new quinone molecules. Then, the expected energy density of the safe, economical and fast-charging aqueous electrolyte battery would be comparable to that of the LIBs intended for high power usage.

1.5 Objectives and outline of this thesis

In order to construct the next generation energy society, high performance of the storage device is required. Quinone and halogen molecules are known to perform fast redox reactions. However, the quinone molecule and the halogen molecule have fatal defects that is low electron conductivity and easily dissolved in the organic electrolyte. In my current study, I tried to overcome demerits mentioned above by adopting the SWCNTs encapsulation system to increase the conductivity and stability of molecules.

In chapter 2, I clarified the phase transformation of halogen molecules with the change of temperature in SWCNT. I also evaluated the performance of the new type of capacitor (electrolytic redox capacitor) using the redox reaction.

In chapter 3, I inserted quinone molecules in two kinds of SWCNT samples with different mean tube diameters, and examined the diameter dependence of Li and Na ion battery electrode properties of the quinone molecules encapsulated in SWCNTs, both at room temperature (RT) and at low temperatures as well.

In chapter 4, I grafted PhQ molecules onto SWCNTs (PhQ/SWCNT) to endow them with higher stability, and investigated the Li and Na ion storage performance of PhQ/SWCNT electrode at low temperature. Furthermore, I used density functional theory (DFT) calculations to understand the detailed features of charge-discharge profiles of PhQ/SWCNT electrode. Based on the calculations, I discussed the difference in discharge potential between Li and Na ions.

Finally, in chapter 5, I developed a safe, low cost, fast rechargeable aqueous electrolyte secondary battery, by combining redox reactions of iodide ions in SWCNTs and alkali metal ions with quinone molecules. I investigated both electrode reactions by CV and charge/discharge experiments in LiI and NaI aqueous electrolyte

Chapter 2

The physical property and electrochemistry of halogen molecules encapsulated in single walled carbon nanotube

2.1 Overview

As mentioned on the chapter 1, EDLCs have attracted much interest from researchers because of their much higher power properties compared to secondary batteries [39-41]. However, the energy density stored in EDLCs is much lower than that of secondary batteries, which makes increasing the capacitance of EDLCs a crucial requirement for their successful implementation in renewable energy systems. To that end, an approach to improve the energy density of EDLC is through the addition of pseudo-capacitance. Pseudo-capacitors realize high energy densities owing to the redox reactions of the electrode active materials.

Recently, a new type of electrochemical capacitor which can work using redox reactions of iodide ions in SWCNTs is demonstrated [30]. The schematic picture of the electrolyte redox electrochemical capacitor (EREC) shown in Fig. 2.1, shows that the redox reaction of anions and the physisorption of cations occur at the positive and negative electrodes, respectively. In conventional EDLCs, both anions and cations are physically adsorbed at electrodes during charge process, so both negative and positive electrode potentials change with the amount of the adsorbed ions (Fig. 2.2 (A)). However, in the case of EREC, the positive electrode potential should be fixed at the redox potential of anions (Fig. 2.2 (B)). If I charge EDLC and EREC up to the same cell voltages, whose limit should be determined by the potential window of the electrolyte (e.g. ca. 1.5 V for aqueous electrolyte), the stored energy of EREC can be much greater than that of EDLC as shown in Fig. 2.2.

On the other hand, EREC can use the redox reaction of iodide ions in a neutral NaI aqueous electrolyte as positive electrode reaction [29]. In this case, the negative electrode potential can be decreased down to the lower limit of the potential window of the electrolyte, which is the hydrogen gas evolution potential. The hydrogen electrode potential E depends on the pH value of the electrolyte, and can be expressed as E = -0.059 pH (Fig. 2.3). As shown in Fig. 2.3, the maximum cell voltage of iodine EREC is estimated to be about 1 V, which was nearly achieved for the iodine EREC in previous study. A glance at Fig. 2.3 shows that it may be very difficult to increase the cell voltage of EREC beyond this value. However, we should take into consideration the overpotential required for hydrogen and oxygen gas evolutions, and the actual potential windows of aqueous electrolytes, which are much greater than 1.23 V especially in the high pH region. Furthermore, the oxygen overpotential is much greater than the hydrogen overpotential in general. It would therefore be a good idea to increase the cell voltage by replacing iodide ions with other ions that have higher redox potentials. This chapter reported on Br EREC. The redox potential of Br is about 0.5 V higher than that of I. Therefore, the cell voltage of Br EREC to be much higher than the other EREC that uses the redox reaction of iodide ions.

On the other hand, the iodine molecules inserted into SWCNTs, which have cylinder pores as amylose has, and reported that the iodine doping greatly improve the electric conductivity and the water dispersibility of SWCNTs [29]. The improvement of the dispersibility can be explained by the electrostatic repulsion between SWCNTs due to the surface charges induced by the charge transfer from SWCNTs to the encapsulated iodine molecules. It should be noted that the dispersibility of SWCNTs increased with decreasing temperature. The increase of the dispersibility at low temperature indicates the increase of charge-transfer at low temperature. However, the mechanism why the charge-transfer increases at low temperature has not been clarified yet. It has not been clarified yet on how polyiodide ions behave at low temperature in a confined nano-space of SWCNTs. Therefore, I investigate in this chapter the low temperature structure

changes of polyiodide ions encapsulated in SWCNTs, by performing in-situ Raman measurements at low temperature for polyiodide ions encapsulated in three kinds of SWCNT samples having different mean tube diameters.

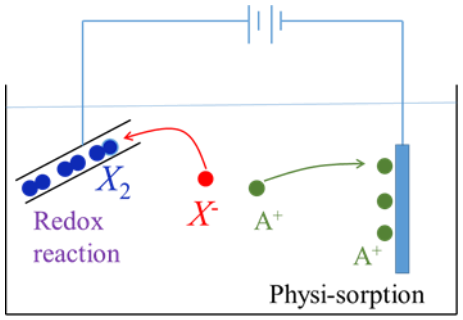

Fig. 2. 1: Schematic picture of EREC using SWCNT electrode. A^+ and X^- refer to alkali metal ions and halogen ions, respectively.

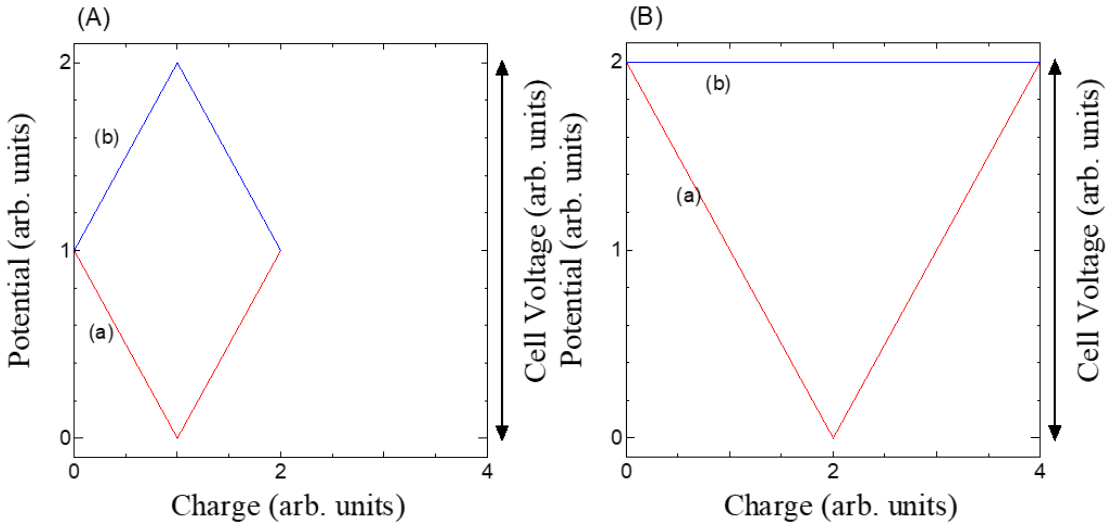

Fig. 2. 2: Electrode potentials of (A) EDLC and (B) EREC as a function of stored charge. In both (A) and (B), (a) and (b) corresponds to negative and positive electrodes, respectively.

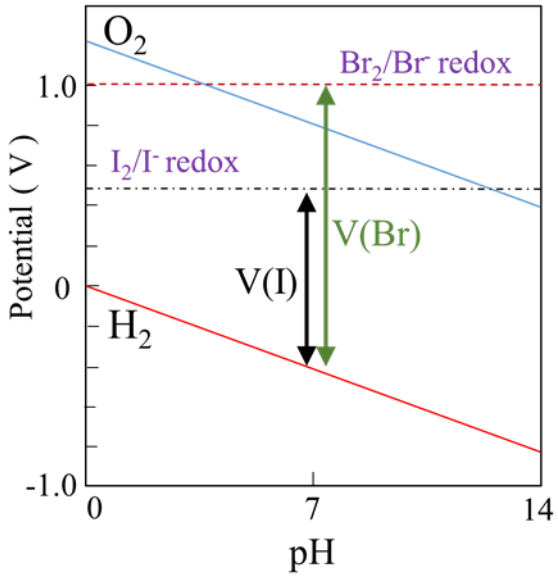

Fig. 2. 3: Expected maximum cell voltages of Br and I EREC. Red and blue lines indicate the potential of hydrogen and oxygen evolutions, respectively.

2.2 Experimental

2.2.1 Iodine molecules encapsulated in SWCNTs

Three kinds of SWCNT samples having different mean tube diameters: HiPco type (supplied by NanoIntegris Technologies Inc.), and SO type and EC type (both supplied by Meijo NanoCarbon Co.) has been used. All the three samples were annealed at high temperature under vacuum. The high temperature annealing not only decreases the surface defects of SWCNTs but also closes the tube ends by forming half fullerene caps at the ends [42]. Subsequently, air-oxidation treatments performed to open the closed ends by burning the half fullerene caps at an appropriate temperature for each SWCNT sample that was carefully determined by prior thermogravimetric (TG) measurement. The tube openings were confirmed by N_2 adsorption measurements. By these series of treatments, high crystalline open-end SWCNT samples prepared. The Raman measurements performed to check the crystallinity and synchrotron by high brightness synchrotron X-ray diffraction (XRD) measurements at BL-18C at the Photon Factory (PF; High Energy Accelerator Organization, Tsukuba, Japan, employing X-rays (λ =

0.614 Å), monochromatized by a Si (111) double-crystal monochromator.) to determine the mean tube diameter. The nanostructure of the obtained samples was observed using a TEM (JEOL z-2500) operated at 100 kV.

Iodine molecules were inserted into SWCNTs by electrochemical oxidation of iodide ions in electrolytic solution. To achieve electrochemical iodine doping, three-electrode configuration cells were fabricated: paper form SWCNT working, Pt counter, and Ag/AgCl reference electrodes. 1 M NaI aqueous solution was used as an electrolyte, and applied 1.8 V to SWCNT electrode for a few minutes. After the encapsulation treatments, the SWCNT samples were washed by distilled water to remove the iodine molecules deposited on the outer surfaces of SWCNTs and I dried the washed samples. The amounts of the encapsulated iodine molecules were determined by TG measurements.

2.2.2 Bromine molecules encapsulated in SWCNTs

SO type and EC type of SWCNTs having different mean tube diameters were used as samples in the present study. The diameter distribution and level of defects of the samples were obtained from Raman spectra excited with two excitation sources: green Nd:YAG laser (λ = 532 nm, EL = 2.33 eV), and red helium-neon laser (λ = 633 nm, EL = 1.96 eV), collected using an NRS-3300 (JASCO) spectrometer. The structural characterization was performed using a JEOL z2500 transmission electron microscope (TEM) operated at 200 kV.

The Br insertion experiments were done in H-shaped glass tubes. One end of the H-type tube was filled with a sufficient amount of pure bromine liquid, and a paper-form SWCNT sample was placed in the other end. Then, the H-shaped glass tube was evacuated while keeping the Br side at liquid nitrogen temperature to freeze the Br liquid, and the SWCNT side at 100ºC to remove the water and gases adsorbed in SWCNTs. After the evacuation of the reaction glass tube, liquid nitrogen was removed

from the Br side, and Br vapor was formed in the reaction tube. The obtained Br-inserted SWCNT samples were thoroughly characterized by Raman, XRD, thermogravimetric (TG) experiments and so on.

2.2.3 Low temperature Raman measurements

In order to know the structure changes of polyiodide ions encapsulated in SWCNTs, low temperature Raman measurements were performed using a JASCO NRS-3300 spectrometer and a Linkam 10036L temperature control stage. I@SWCNTs sample was sealed in a glass capillary, which is originally used for XRD measurement, and the glass capillary was set on the cooling metal block. Temperature sensor was attached with the cooling block. I started Raman measurements at each temperature a few minutes after temperature reached to the target temperature. The low temperature Raman measurements of I@SWCNTs samples were done with two excitation lasers (λex = 532 nm and 633 nm).

In order to assign the vibration mode of Raman peaks, ab initio calculations were performed. Structural optimizations and vibrational frequency calculations of polyiodide ions were performed based on the second order Møller–Plesset (MP2) perturbation theory using Gaussian09 software [43]. Dunning's augmented double-zeta correlation consistent basis set with small-core relativistic pseudopotentials [44] (aug-cc-pVDZ-PP) was used for the calculation.

2.2.4 EREC measurement

For charge-discharge experiments, a three-electrode cell was used. A self-supported paper-form SWCNT sample (Bucky paper) was used as the cathode. The electrode sheet used as the anode was prepared by kneading a mixture of 8 : 1 : 1 of activated carbon (Kuraray YP50F) : carbon black : polytetrafluoroethylene (PTFE). Platinum mesh current collectors were used for both electrode samples. An Ag/AgCl

was used as reference electrode, and 1 M NaBr aqueous solution was used as the electrolyte solution. Charge-discharge experiments were conducted using a potentiostat/galvanostat (VersaSTAT3, Princeton Applied Research) controlled by a computerized system.

2.3 The phase transformation of polyiodide ions encapsulated in SWCNTs on the low temperature

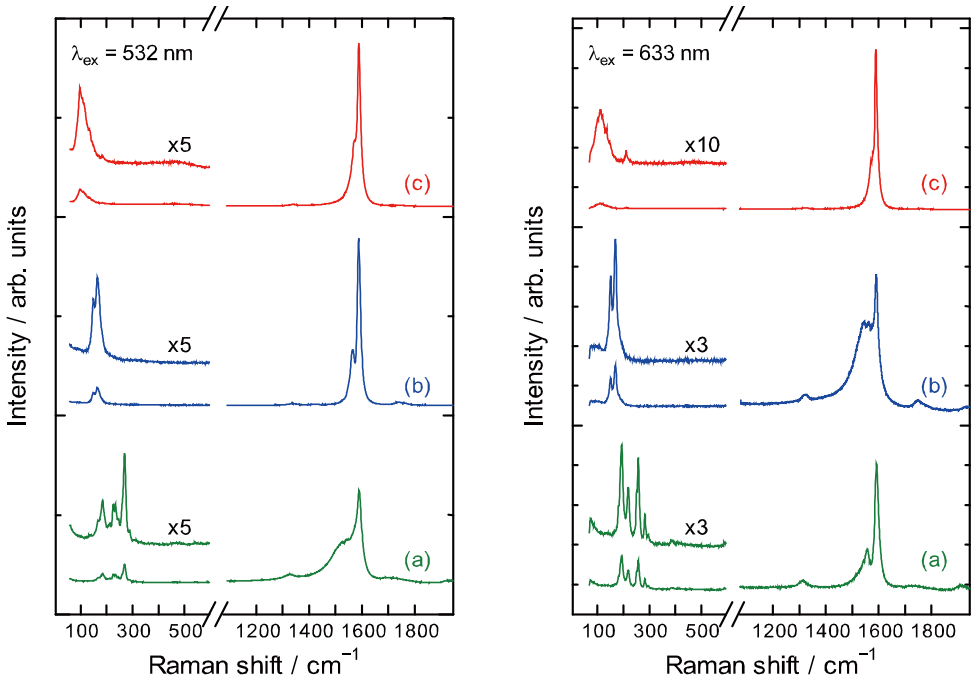

Fig. 2. 4: Room temperature Raman spectra of (a) HiPco, (b) SO, and (c) EC SWCNTs. Two types of excitation laser were used for the measurements: (left panel) 532 nm, (right panel) 633 nm.

Fig. 2.4 shows Raman spectra of three SWCNT samples (HiPco, SO, EC) used in the present study. D-band peaks observed at around 1330 cm^{-1} are so weak that it is very hard to find D-band peaks for SO and EC samples. Although D-band peak of HiPco sample is relatively high compared to the other two samples, its intensity ratio to G-band peak observed at around 1590 cm^{-1} is quite small. Therefore, I can judge that all the three SWCNT samples have high crystallinity. In low wavenumber region (<500 cm^{-1}), radial breathing modes (RBMs) were observed. It is well known that the peak

position of RBM of a SWCNT is in inverse proportion to its tube diameter and that some empirical equations were proposed to evaluate tube diameter (dSWCNT) from RBM peak position (ω_{RBM}) [45-47]. Among the equations, tube diameter is often evaluated by a simple equation ($d_{SWCNT} = 248/\omega_{RBM}$) proposed by A. Jorio [46]. However, since the Raman scattering from SWCNTs is dominantly in resonance process and only a very small set of tubes in diameter distribution participate in this process for a single excitation laser, I should avoid to discuss the diameter distribution based on a single Raman spectrum. So, I also observed Raman spectra for the SWCNT samples using different excitation lasers, and estimated tube diameters of three SWCNT samples: HiPco (1.0 ± 0.3 nm), SO (1.5 ± 0.2 nm), EC (2.5 ± 0.3 nm). I also observed XRD patterns of the SWCNT samples. As shown in Fig. 2.5, clear XRD patterns due to ordered bundle structures were observed for SO and EC samples. However, only broad halo pattern was observed for HiPco sample because tube diameter of HiPco sample is not uniform and thereby an ordered bundle structure is hardly formed. I performed XRD pattern simulation using two parameters [48, 49] (mean tube diameter d_{mean} and tube center-to-center distance a) for SO and EC samples. The tube diameter value determined by XRD simulation is closer to the average tube diameter than that determined by Raman measurement, because XRD pattern reflects over all the tubes in the samples. It is known that distance between two tubes is less than layer distance (0.335 nm) of graphite. In the present study, I could get best fit of simulation pattern to observed pattern with tube distance of about 0.31 nm. The mean tube diameters of SO and EC samples were determined to be 1.5 ± 0.1 nm and 2.5 ± 0.2 nm, respectively. These values are consistent with the diameter distributions determined by Raman measurements. For convenience, I will refer to SO and EC samples as SWCNT-1.5 and -2.5 to express their mean tube diameter. Although I could not determine the mean tube diameter for HiPco sample, by XRD simulation, I will express it as SWCNT-1.0 using the representative diameter value. TEM observations (Fig. 2.6) confirmed that these three SWCNT samples have high purity.

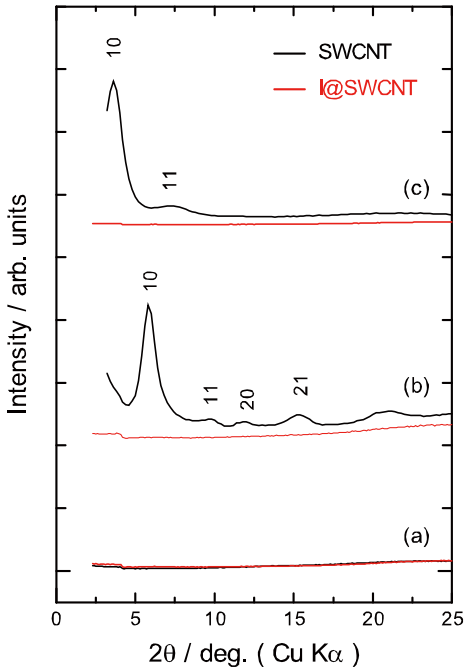

Fig. 2. 5: Powder XRD patterns of (a) SWCNT-1.0, (b) SWCNT-1.5, and (c) SWCNT-2.5, before (black lines) and after (red lines) the encapsulation of iodine molecules.

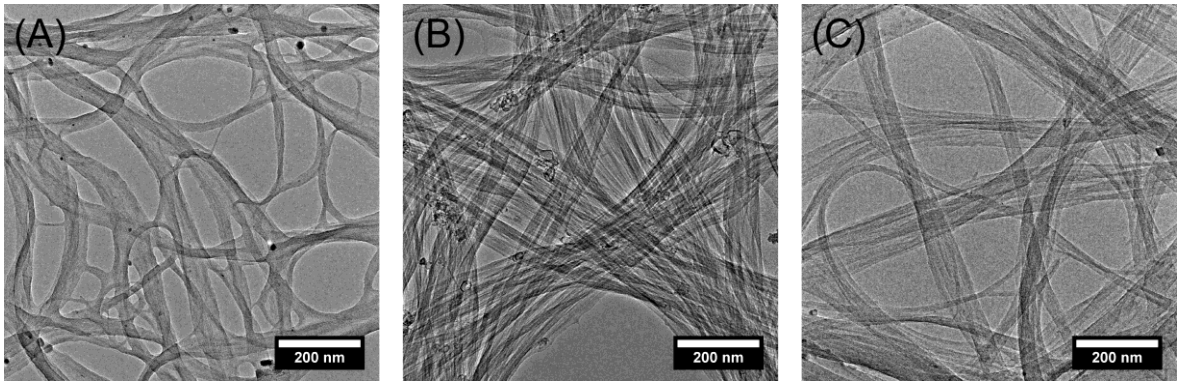

Fig. 2. 6: TEM images of (A) HiPco, (B) SO, and (C) EC SWCNTs.

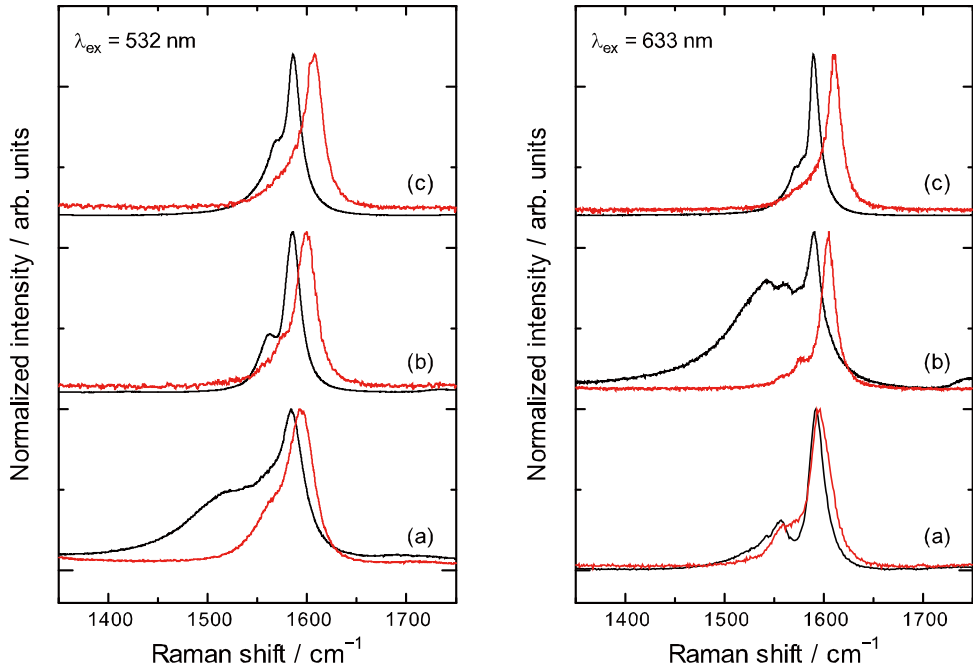

Fig. 2. 7: Room temperature Raman spectra of (a) SWCNT-1.0, (b) SWCNT-1.5, and (c) SWCNT-2.5, before (black lines) and after (red lines) the encapsulation of iodine molecules. Two types of excitation laser were used in the measurements: (left panel) 532 nm, (right panel) 633 nm.

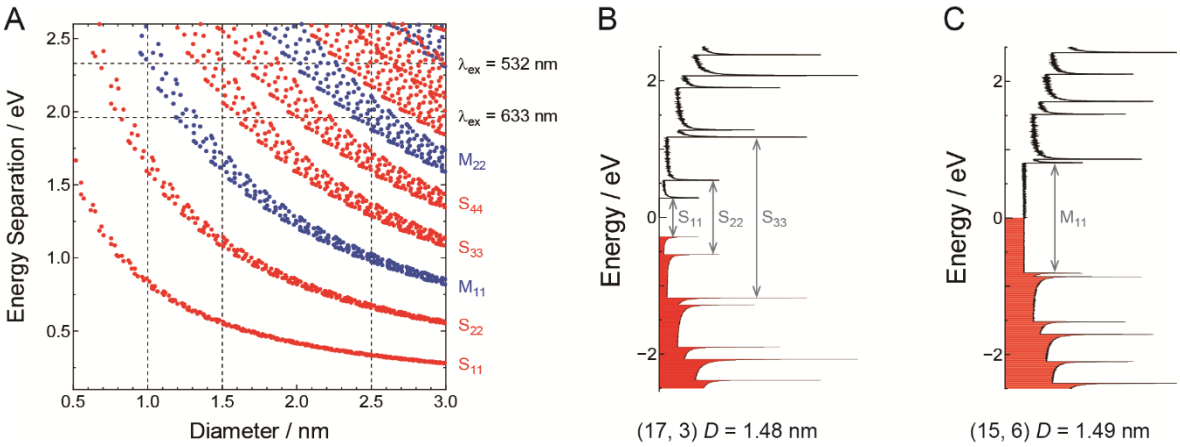

Fig. 2. 8: (A) Kataura plot, and electronic density of states (DOSs) of (B) semiconducting and (C) metallic SWCNTs. In the DOS figures, the positions of Fermi energy (EF) are set as 0 eV and Valence levels are filled with red.

Raman spectra of the SWCNT samples drastically changed by iodine encapsulation. First, I discuss the changes in G-bands (Fig. 2.7). Using the Kataura

plots (Fig. 2.8) that summarizes the relations between tube diameters and the energy gaps of van Hove (vH) singularity points of several chirality SWCNTs, the chirality of SWCNT can be predicted in relation to its diameter [50]. Using the diameter values estimated from the XRD and Raman measurements, I find that the 532 nm laser is resonant with metallic tubes in SWCNT-1.0, semiconducting tubes in SWCNT-1.5, and semiconducting tubes in SWCNT -2.5. On the other hand, 633 nm laser was resonant with semiconducting tubes in SWCNT-1.0, metallic tubes in SWCNT-1.5, and metallic tubes in SWCNT-2.5. As expected above, the G-bands of SWCNT-1.5 (532 nm excited) and SWCNT-1.5 (633 nm excited) show broad profiles having long tails on the lower wavenumber side that are Breit-Wigner-Fano (BWF) profiles seen for metallic SWCNTs [51]. On the other hand, BWF profile of SWCNT-2.5 (633 nm excited) is not very clear probably because metallic tubes of SWCNT-2.5 might have less number of free electrons than those of SWCNT-1.0 and -1.5. The BWF profiles of SWCNT-1.0 (532 nm) and -1.5 (633 nm) disappeared by iodine encapsulations and sharp G-band profiles were observed (Fig. 2.7). These profile changes indicate the removal of free electrons of SWCNTs, that is, charge-transfer from SWCNTs to iodine molecules [52,38]. With these profile changes, the peak positions of G-bands shifted toward higher wavenumber side by iodine encapsulations. The G-band peak shifts were observed not only for metallic tubes but also for semiconducting tubes. The blue-shifts of G-bands of SWCNTs by iodine or other acceptor doping have been reported in previous papers and it has been discussed that the magnitude of the shift is highly dependent on the hole doping level corresponding to the charge-transfer level [53-56]. It is interesting that the G-band shift of metallic tubes is greater than that of semiconducting tubes for the same SWCNT sample. It means that the amount of charge-transfer from metallic tubes to iodine molecules is greater than that from semiconducting tubes probably because active electrons at around of Fermi level of metallic tubes are easier to move to iodine molecules.

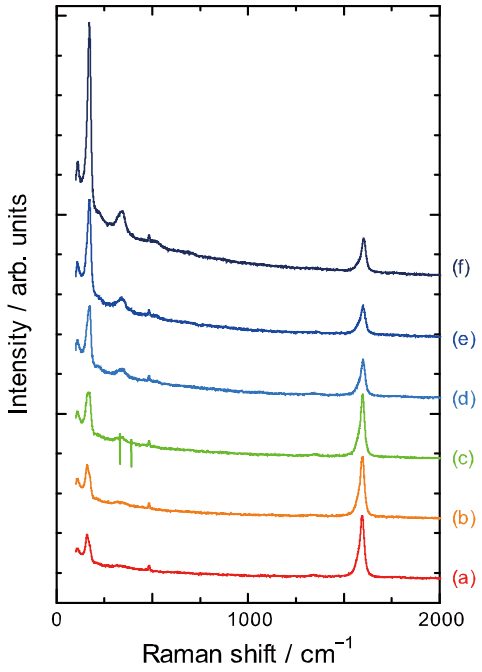

Fig. 2. 9: Raman spectra of I@SWCNT-2.5 measured at (a) 25°C, (b) −20°C, (c) −40°C, (d) −60°C, (e) −80°C, and (f) −100°C. A 532-nm laser was used as the excitation source.

Fig. 2.9 shows change in Raman spectra of I@SWCNT-2.5 (532 nm excited) with decreasing temperature. In low wavenumber region, several Raman peaks of polyiodide ions were observed: Raman peak of I_3^- was observed at about 110 cm^{-1} and peaks in 160–175 cm^{-1} should be assigned to I_5^- and/or longer polyiodide ions. These polyiodide ions are made by the charge-transfer from SWCNTs to I_2 molecules after iodine encapsulation because previous electrochemical quartz-crystal microbalance (EQCM) measurements revealed that iodine molecules are inserted into SWCNTs as a form of I_2 molecule by the electrochemical oxidation treatments [30]. The polyiodide ion formation by the charge-transfer was also observed for I@SWCNTs produced by I_2 gas phase reaction [57]. Some overtones of the polyiodide ion peaks are often observed in higher wavenumber region. The peak intensities of polyiodide ions (relative to the SWCNT G-band peak intensity) increase with decreasing temperature. Furthermore, it was also observed that the G-band peak position of I@SWCNT-2.5 shifted toward higher wavenumber side with decreasing temperature. Although the G-band peak of

empty SWCNTs also shows blue shift at low temperature, the shift is much smaller than that of I@SWCNTs. These experimental data indicate that the number of polyiodide ions and the magnitude of the charge-transfer from SWCNTs to iodine molecules increase with decreasing temperature. These two phenomena can be explained if the following reactions (e.g. $5I_2 + 2e^- \rightarrow 2I_5^-$ or $7I_2 + 2e^- \rightarrow 2I_7^-$) would be promoted with decreasing temperature. The assumption is plausible because the reactions are exothermic reactions and are promoted at low temperature.

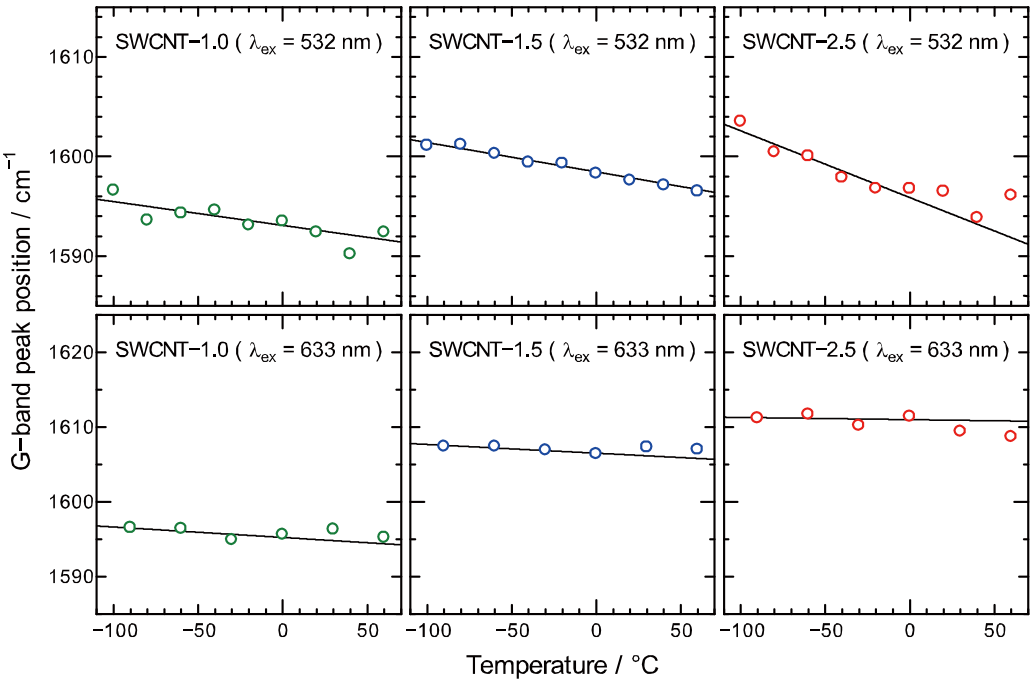

Fig. 2. 10: G-band peak position vs. temperature plots of (left panels) SWCNT-1.0, (center panels) SWCNT-1.5 and (right panels) SWCNT-2.5 observed with two excitation lasers (upper panels: 532 nm, lower panels: 633 nm).

Fig. 2.10 summarizes the G-band peak shifts with temperature for three SWCNT samples observed with two excitation lasers. As shown in Fig. 2.10, the peak shifts of SWCNT-1.5 (532 nm) and -2.5 (532 nm) are much greater than others. Both two Raman spectra of SWCNT-1.5 (532 nm) and -2.5 (532 nm) are mainly from semiconducting tube. The temperature-induced shift in the G-band position of SWCNT-1.5 (532 nm) and -2.5 (532 nm) in the range of −100 – 0°C are −0.029 and −0.067 cm^{-1}/K,

respectively. In the same temperature range, the slope of SWCNT-1.0 (633 nm) is −0.014 cm^{-1}/K. It means that semiconducting SWCNTs having greater tube diameter show the greater temperature gradient of G-band shift. On the other hand, the gradients of metallic tubes regardless of tube diameter are very small. These phenomena should relate to the electronic structures of I@SWCNTs. One of the characteristic points of electronic structure of SWCNTs is an appearance of vH singularity points where density of states (DOSs) greatly increases. The depth from fermi level to the highest vH point in the valence band (or the energy gap between this vH point and the corresponding energy levels in the conduction band: S_{11} for semiconducting tube and M_{11} for metallic tube) decreases with increasing tube diameter. It is also known that M_{11} is much larger than S_{11} for SWCNTs having similar diameters. (See Fig. 2.8) For SWCNT-1.0, -1.5 and -2.5, S_{11} is about 0.85, 0.59 and 0.34 eV, and M_{11} is about 2.45, 1.68 and 1.01 eV, respectively. These energy relations might explain the temperature gradients of G-band shifts. At room temperature where charge-transfer from SWCNTs to iodine molecules is small, as I already wrote, the reason why the G-band shifts of metallic tubes are greater than those of semiconducting tubes can be explained by that active electrons of metallic tubes at around of fermi energy are easier to be transferred to iodine molecules. On the other hand, the temperature dependence of G-band shift of semiconducting tubes are greater than those of metallic tubes at low temperature. The magnitude of charge-transfer from SWCNTs to iodine molecules increases with decreasing temperature and thereby the polyiodide ion formation is promoted at low temperature. It means that the energy levels of the SWCNT electrons transferring to iodine molecules decrease with decreasing temperature. If the energy level goes down to the first vH singularity point of semiconducting SWCNTs, semiconducting SWCNTs have the greater number of electrons that can move to iodine molecules than metallic tubes have. Such a situation might occur in SWCNT-1.5 and -2.5. It would be the reason for the greater temperature dependence of G-band shifts of SWCNT-1.5 and -2.5. In the case of SWCNT-1.0, the first vH singularity point of semiconducting tubes is too

deep to increase the charge-transfer electrons. Of course, the first vH points of metallic tubes of three SWCNT samples are much deeper than the first vH point of semiconducting SWCNT-1.0.

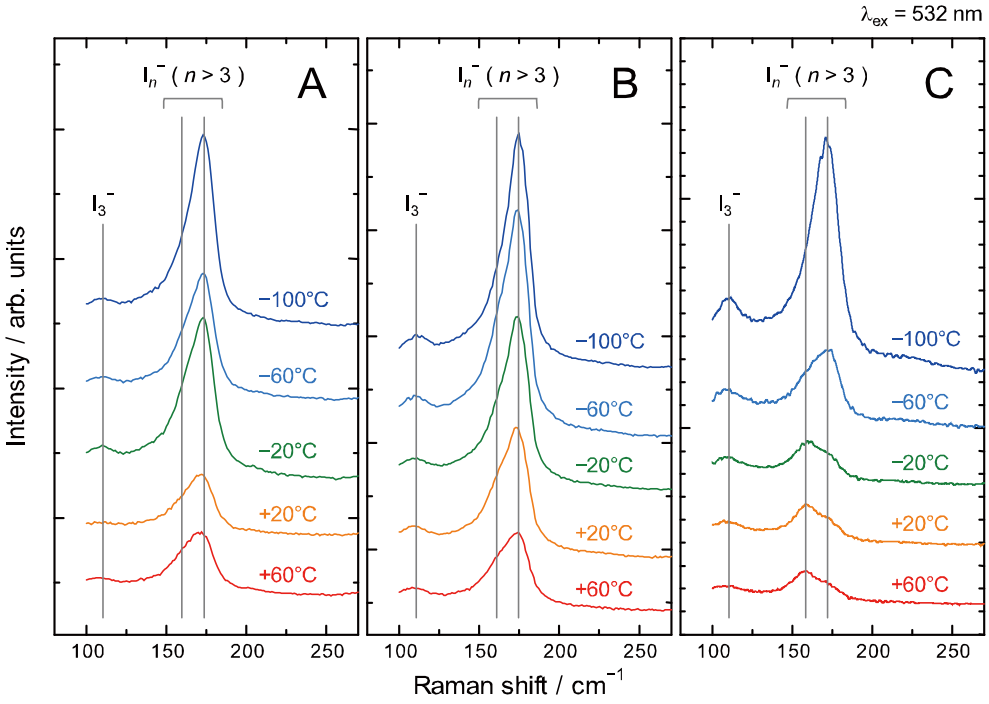

Fig. 2. 11: Temperature dependent Raman spectra of (A) I@SWCNT-1.0, (B) I@SWCNT-1.5 and (C) I@SWCNT-2.5 measured with 532-nm excitation laser.

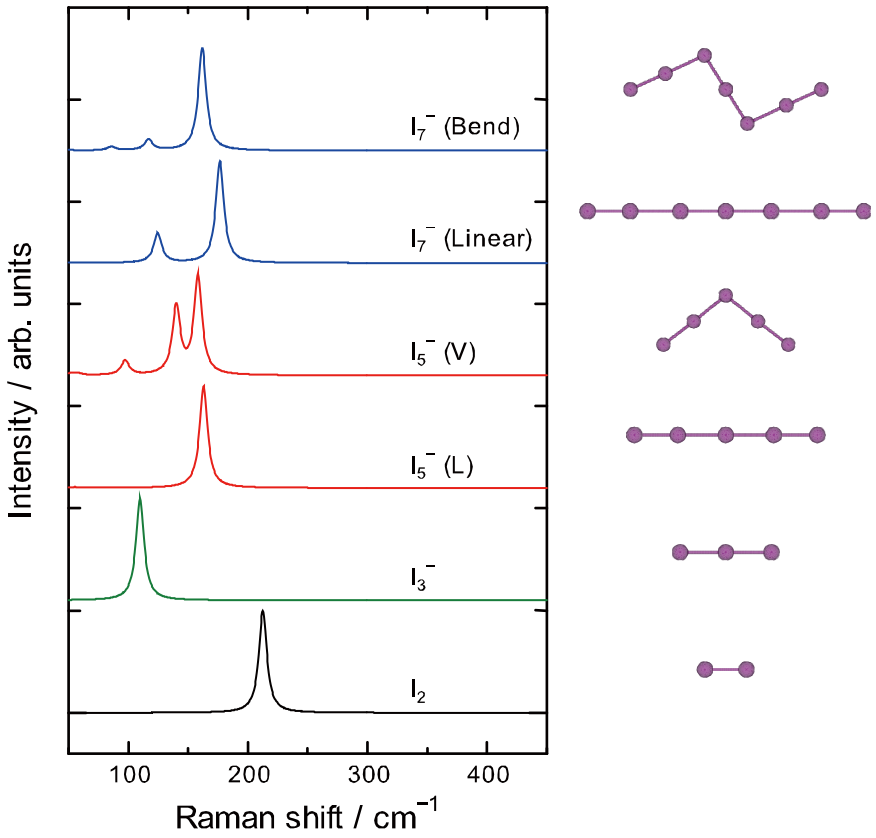

Fig. 2. 12: Theoretical Raman spectra of polyiodide ions.

Next, I will see change in Raman peak profiles of polyiodide ions with temperature. As I wrote already, Raman peak observed at about 110 cm^{-1} and peaks in 160–175 cm^{-1} should be assigned to I_3^- and longer polyiodide ions, respectively. Fig. 2.11 shows change in Raman spectrum (532 nm excited) of polyiodide ions encapsulated in SWCNT-2.5. For longer iodide ions, peak profile consists of two peaks of 160 cm^{-1} and 175 cm^{-1}. At room temperature, the peak of 160 cm^{-1} has greater intensity than 175 cm^{-1} peak. However, the peak of 175 cm^{-1} grows with decreasing temperature and it becomes to be the dominant peak at low temperature. For SWCNT-1.0 and -1.5, already at room temperature, 175 cm^{-1} peaks are the main peak and 160 cm^{-1} peaks are observed as shoulder peaks. It should be noted for the peak profile observed in the wavenumber region that the peak profile observed by 532 nm excitation laser is very different from that observed by 633 nm for all the three SWCNT samples. For example, for SWCNT-2.5, doublet peak profile of 160 cm^{-1} and 175 cm^{-1} peaks were clearly observed by 532 nm laser while singlet peak of 160 cm^{-1} was observed by 633 nm. It

means that 175 cm^{-1} peak is a resonant Raman peak. Although I wrote 160 and 175 cm^{-1} peaks are of longer polyiodide ions I_n^- ($n > 3$), I'll discuss possible forms for these two peaks. One possibility is to assign these two peaks to different forms of I_5^-. In the previous papers, V-shape and Linear I_5^- have different Raman peak positions [58]. However, the peak positions of I_5^-(V) and I_5^-(L) were reported to be 157.4 and 165.0 cm^{-1}, respectively, which are not in good agreement with 160 and 175 cm^{-1} observed in the present study. It would be possible that the frequency modes of I_5^-(V) and I_5^-(L) were hardened in SWCNTs. This possibility is dismissed as follows. The frequency mode of I_5^-(L) was always observed at higher wavenumber side of I_5^-(V) peak. In fact, the order of the wavenumbers of I_5^-(V) and I_5^-(L) frequencies is reproduced by our ab initio calculations as shown in Fig. 2.12. Therefore, if the 160 and 175 cm^{-1} peaks are attributed to two forms of I_5^-, I have to assign 160 and 175 cm^{-1} peaks to I_5^-(V) and I_5^-(L), respectively. In this case, Raman peak of I_5^-(L) should be in resonance with 532 nm laser, as I discussed that 175 cm^{-1} peak is a resonant Raman peak. In order to check whether the Raman peak of I_5^-(L) is resonant process or not, I performed an experiment using amylose. Amylose has a helix structure and polyiodide ions are encapsulated in amylose [59-65]. The observed Raman spectra of amylose having linear polyiodide ions in its helix pores are shown in Fig. 2.13. In the Raman spectra, 110 cm^{-1} peak of I_3^- and 160 cm^{-1} peak, which is assigned to I_5^-(L), are observed. The relative intensity of 160 cm^{-1} peak to I_3^- peak at 110 cm^{-1} observed by 532 nm laser is almost the same as that observed by 633 nm. It means that the frequency mode of I_5^- (L) is not in a resonance process for 532 nm excitation. The resonance wavelength of I_5^- might be smaller than 532 nm. In the previous papers, it was reported that 110 cm^{-1} and 160 cm^{-1} peaks are enhanced by 458–477 nm and 488–514 nm lasers, respectively [66]. Therefore, the assignments of 160 cm^{-1} and 175 cm^{-1} peaks to different forms of I_5^- should be wrong.

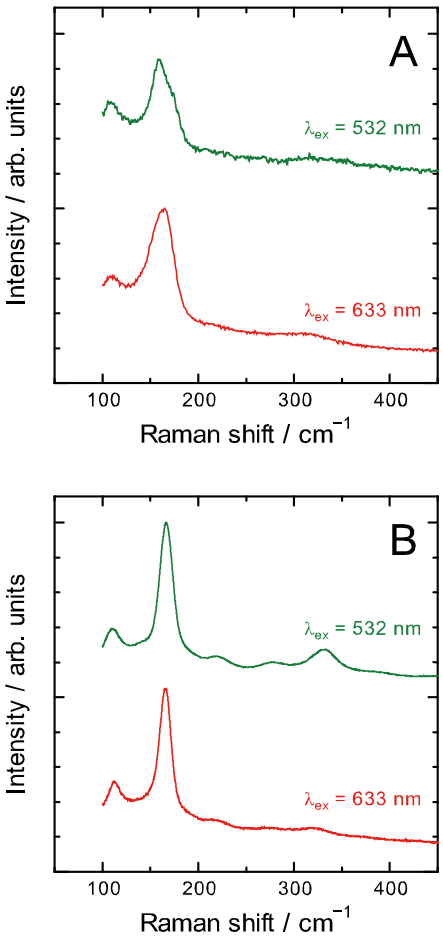

Fig. 2. 13: Raman spectra of (A) I@SWCNT-2.5 and (B) I@amylose. Excitation wavelength of green and red lines are 532 nm and 633 nm, respectively.

I'll think about second possibility: 160 and 175 cm^{-1} peaks are assigned to I_5^- and I_7^-, respectively. In this case, the frequency mode of I_7^- should be in resonance to 532 nm. It would be reasonable that the resonance wavelength of I_7^- should be longer than that of I_5^- (488–514 nm), because larger polyiodide molecules should have smaller HOMO-LUMO gaps. Based on this assignment, I'll discuss the following observations: (1) 175 cm^{-1} peak intensity increases compared to 160 cm^{-1} peak with decreasing temperature for SWCNT-2.5, (2) 175 cm^{-1} peaks are the dominant peak for SWCNT-1.0 and -1.5 already at room temperature. For the former observation, one can explain it by the transformation from I_5^- to I_7^- through the reaction of $I_5^- + I_2 \rightarrow I_7^-$. However, as shown in the Raman spectra observed by 633 nm, 160 cm^{-1} peak intensity does not change with temperature. It means that the number of I_5^- does not decrease with

decreasing temperature. Therefore, instead of the transformation from I_5^- to I_7^-, I have to think simple increase of I_7^- (e.g. $7I_2 + 2e^- \rightarrow 2\ I_7^-$). This idea is consistent with the observation that the relative peak intensity of polyiodide ions to SWCNT G-band increases with decreasing temperature. Since the peak intensity of I_5^- in amylose does not change with temperature, the increase of polyiodide Raman peak is characteristic feature of SWCNTs. As I wrote already, iodine molecules are inserted into SWCNTs as a form of I_2 molecule. Therefore, in the case of iodine molecules encapsulated in SWCNTs, certain amounts of I_2 molecules exist in SWCNTs. Although no strong Raman peak of I_2 molecules was observed, it does not indicate the absence of I_2 molecules, but it is due to the small extinction coefficient of I_2: Raman scattering activities of I_2 molecule estimated by an ab initio calculation performed on the present study is about 140 times smaller than that of the linear I_5^- molecule. It should be due to the existence of I_2 molecules in SWCNTs that the intensity of polyiodide Raman peaks of I@SWCNTs increases with decreasing temperature unlike in the case of amylose. Although the I_2 molecules are probably randomly adsorbed in the hollow cores of SWCNT-2.5 at room temperature, they would be gathered on the inner surface of SWCNTs with decreasing temperature and transformed to polyiodide ions by charge-transfer from SWCNTs. On the other hand, since tube diameters of SWCNT-1.0 and -1.5 are so small, long polyiodide ions having Raman peak of 175 cm^{-1} are dominantly formed by capillary condensation effect even at room temperature.

2.4 Bromine aqueous electrolyte redox capacitor using SWCNTs

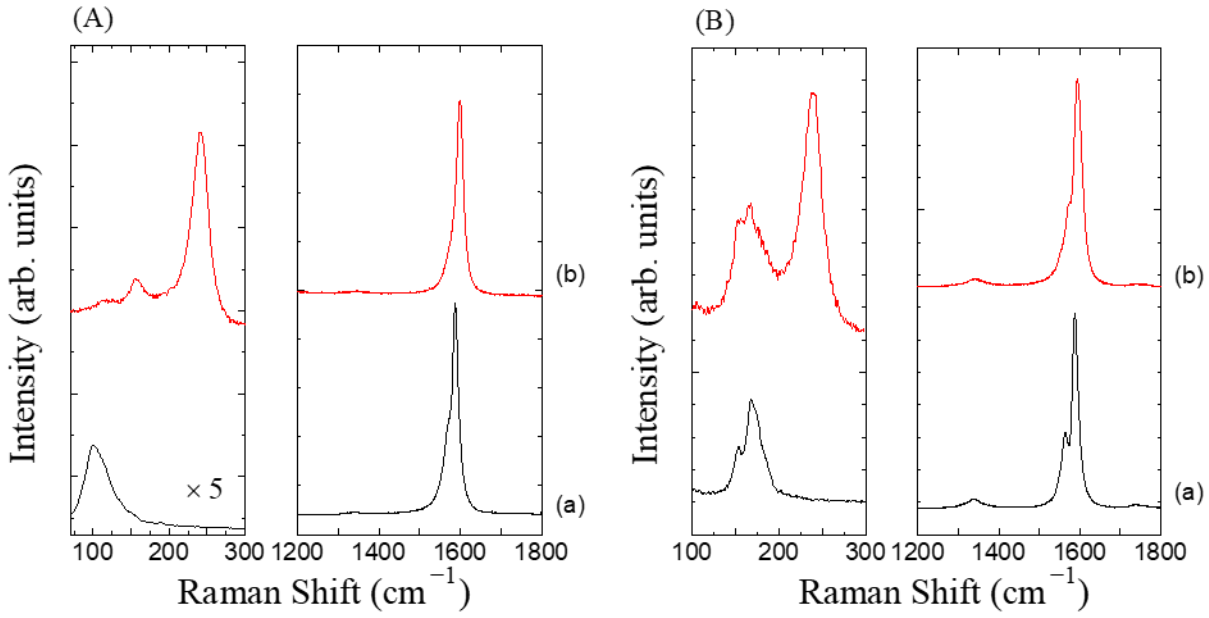

Fig. 2. 14: Raman spectra of (A) SWCNT-2.5 and (B) SWCNT-1.5, (a) before and (b) after Br insertion.

The Fig. 2.14 shows the observed Raman spectra of Br-inserted SWCNT sample. Since the peak intensity of D-band at about 1330 cm^{-1} does not increase, the Br insertion treatment does not cause damage to the crystallinity. On the other hand, in low-wavenumber region, I observed strong Raman peaks due to Br insertion. For SWCNT-2.5, I observed two peaks at around 240 and 160 cm^{-1}. The peak at about 240 cm^{-1} was also observed in Raman spectrum of Br-inserted SWCNT-1.5. Although the peak at 160 cm^{-1} was not very clear because of the overlapping with RBM peaks, the change of the RBM peak profile might indicate the existence of the Br peak at 160 cm^{-1} in Br-inserted SWCNT-1.5. The two Br Raman modes observed at 240 and 160 cm^{-1} can be assigned to the Br-Br stretching modes in $(Br_2)_n$ chains and Br_3^- poly-bromide ions, respectively [67]. However, it should be noted that the $(Br_2)_n$ chain might carry a charge due to charge transfer reaction with SWCNTs, and that long poly-bromide ions (e.g. Br_5^- ($Br_3^-\cdot Br_2$)) can be included in the charged $(Br_2)_n$ chain [67]. As mentioned above the

structure and its temperature change of the inserted iodine molecules depend on the diameter of the host SWCNTs. However, in the case of Br, and as shown in Fig. 2.14, the structures of the Br molecules inserted in SWCNT-1.5 and -2.5 should be the same, because the observed Raman patterns of the inserted Br molecules are identical to each other. Furthermore, I confirmed that the temperature changes of these Br Raman peaks are almost the same for SWCNT-1.5 and -2.5. Therefore, Br and I molecules are likely to be inserted in different sites of SWCNTs. Namely, the insertion position of iodine molecules in SWCNTs is the hollow core of each nanotube. On the other hand, bromine molecules might be preferentially inserted in the triangle lattice space of SWCNT bundles, because the ion size of Br is much smaller than that of I.

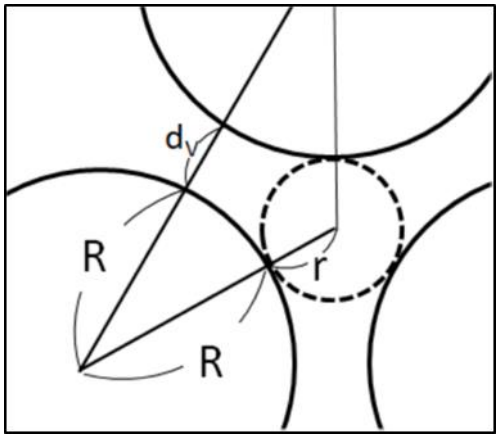

Fig. 2. 15: Schematic picture of SWCNT (solid circle) bundle triangular space (dashed circle).

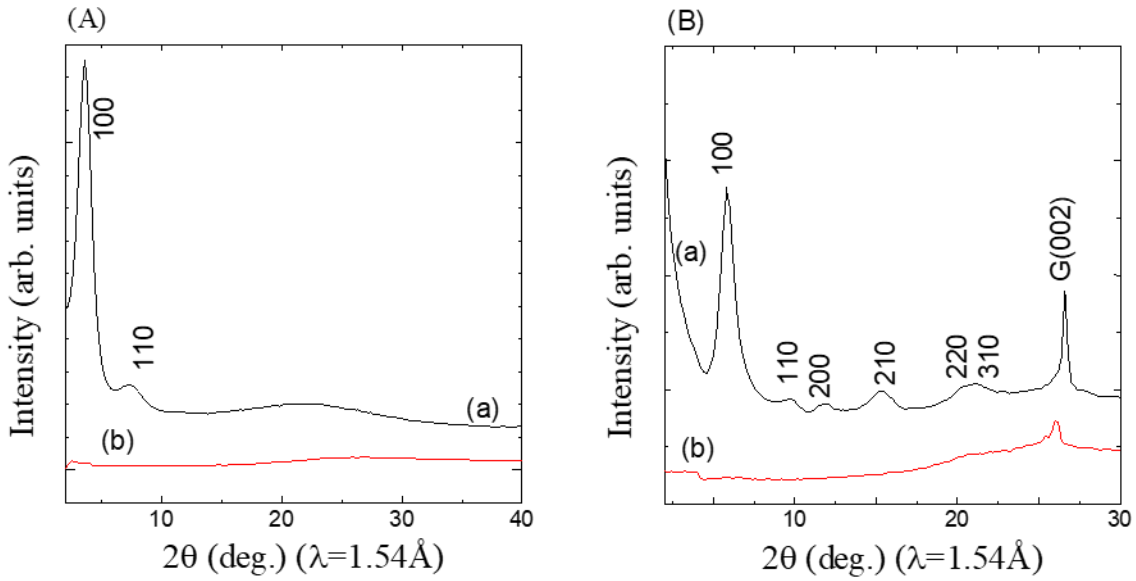

Fig. 2. 16: XRD pattern of (A) SWCNT-2.5 and (B) SWCNT-1.5, (a) before and (b) after Br insertion. G(002) indicates the 002 diffraction of graphitic impurities.

Both SWCNT-1.5 and -2.5 samples used in the present study have good crystallinity and form well-ordered bundle structure (Fig. 2.15). Therefore, I observed strong diffraction patterns from the quasi-two-dimensional bundle structures (Fig. 2.16). Fig. 2.15 shows a part of the bundle triangle lattice, where R is the radius of SWCNT, d_v is van der Waals distance between two tubes, and r is the radius of the triangular space surrounded by three tubes. The three parameters can be related to each other by equation 2.1.

$$r = \left(\frac{2}{\sqrt{3}} - 1\right) R + \frac{1}{\sqrt{3}} dv \qquad (2.1)$$

It is well known that the interlayer distance of graphite is 0.335 nm, and that the intertubular distance of SWCNTs is quite smaller than that value. If I assume that d_v is 0.33 nm, the value of r can be determined to be 0.3 and 0.38 nm for SWCNT-1.5 and -2.5, respectively. The obtained values indicate that Br might be preferentially inserted in the triangular lattice space. It is plausible that the insertion of Br molecules in triangular space would cause disorder in the SWCNT bundle structure. In my study, the diffraction lines of the bundle structures completely disappeared after Br insertion for

both SWCNT-1.5 and -2.5. It should be noted that only 100 diffraction loses its intensity and that higher order diffractions are usually observed when guest molecules are inserted in the hollow cores of SWCNTs [68]. This was shown in section 2.3 in which higher order diffractions were observed for iodine molecules encapsulated in SWCNTs. In other words, iodine and bromine molecules are likely inserted in the hollow cores and bundle triangular spaces of SWCNTs, respectively. The diffraction line observed at around 26.5º in Fig. 2.16 is the diffraction of graphitic impurities. The peak was still observed after the Br insertion, although the peak position shifted to lower angle side. The shift to lower angle is probably due to Br intercalation into the layered structure of the graphitic impurities.

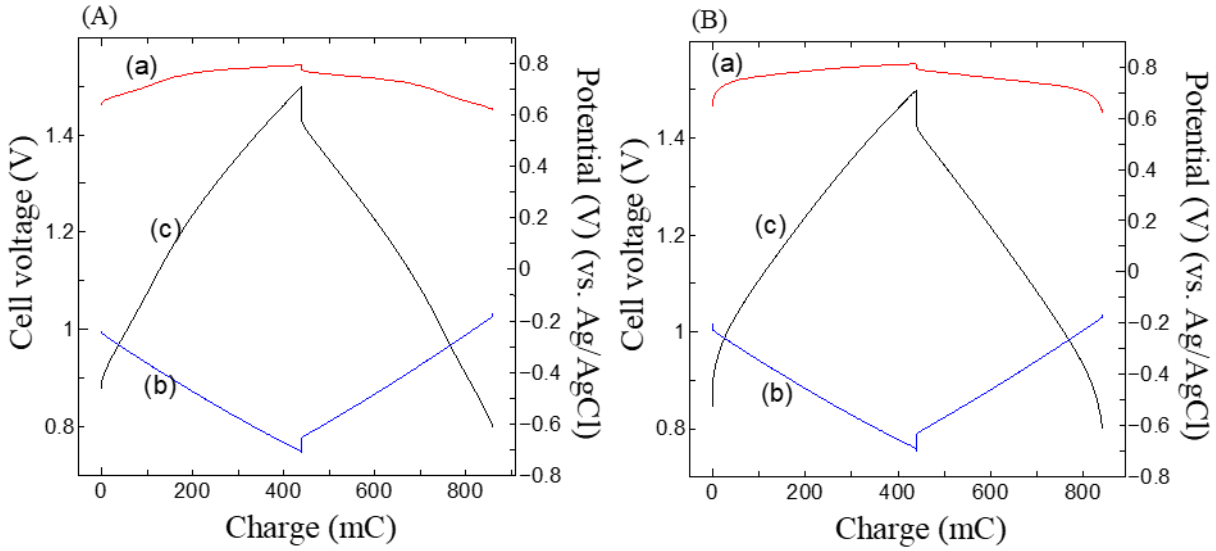

Fig. 2. 17: (a) Positive electrode and (b) negative electrode potentials, and (c) cell voltage of the EREC cell as a function of accumulated/released charges, using (A) SWCNT-2.5 and (B) SWCNT-1.5. The profiles were measured at a constant current density of 1 A/g.

Fig. 2.17 shows charge-discharge curves obtained with a test cell consisting of SWCNT positive electrode and activated carbon negative electrode. Fig. 2.17 shows that the negative electrode potential changes proportionally with accumulated charge. Namely, the negative electrode behaves as a typical EDLC electrode. On the other hand,

the values of the positive electrode potential are almost constant irrespective of the value of charge. Also, these values were almost the same for both SWCNT-1.5 and -2.5, and were found to correspond to the redox potential of bromide ions. Namely, I was able to operate Br EREC in a neutral NaBr aqueous electrolyte without oxygen evolution, probably due to the large overpotential. As I expected, I was able to increase the cell voltage up to 1.5 V, which is about 0.5 V higher than that of the iodine EREC reported in the previous paper [30]. As the energy stored in EREC is proportional to the square of the cell voltage, the 0.5 V increase leads to a large improvement of the energy density of the device.

In the section 2.1, I explained with Fig. 2.3 how EREC can store much more energy than EDLC. Here, I would like to add another advantage point of EREC towards storing high energy density. The specific capacitance of general carbon materials is about 5-10 μF/cm^2 [69]. Assuming 1 g carbon materials having a specific capacitance of 5 μF/cm^2 and specific surface area of 1000 m^2/g is used as negative electrode for EREC, the negative electrode will store 75 C (5 (μF/cm^2) ×1000(m^2/g) × 1.5 (V)), when the cell is charged to 1.5 V.

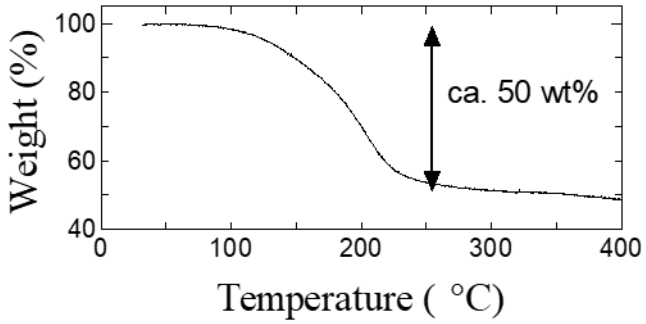

Fig. 2. 18: TG curve of the Br-inserted SWCNT-2.5 sample.

To determine the amount of SWCNTs required to store the charge of 75 C at positive electrode, I analyze the TG curve of the Br-inserted SWCNT-2.5 shown in Fig. 2.18. The TG curve shows that SWCNT-2.5 can store 50 wt.% Br. To charge 75 C, about 0.062 g (79.9(g/mol) × 75 (C)) / F(C/mol)) Br is required. To store 0.062 g Br,

0.062 g SWCNTs is required. Namely, the active materials for positive electrode (redox electrode) can be significantly less than that for EDLC electrode. The smaller amount of electrode material is another factor that contributes to improving the energy density of the device.

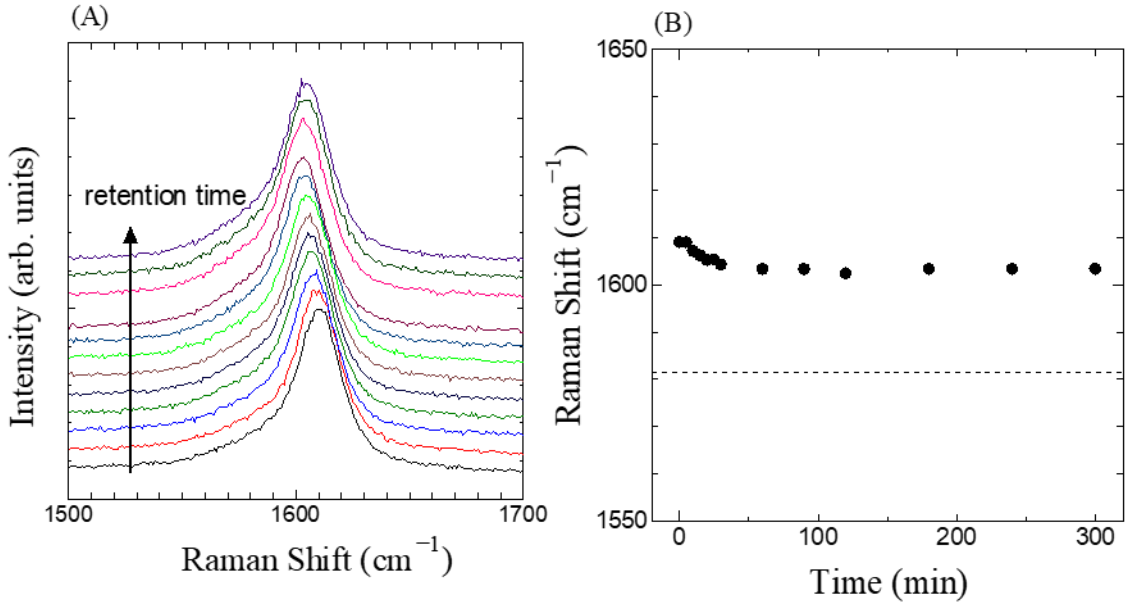

Fig. 2. 19: (A) The observed Raman spectra for leakage test. (B) The observed G-band peak positions as a function of time after Br insertion.

Finally, I investigated the capacity retention of the positive electrode (Br redox electrode). Usually, the capacity retention of the electrode is measured by the electrode potential change with time. However, this method is not applicable in the case of EREC, because the positive electrode potential should be kept at the Br redox potential. Therefore, I monitored the Raman G-band peak position of SWCNT positive electrode after electrochemical Br insertion. As I already mentioned, the G-band peak position of SWCNT is blue-shifted by Br insertion because of the charge transfer from SWCNTs to Br molecules. The amount of shift corresponds to the amount of the inserted Br molecules. Fig. 2.19 (A) shows the G-band peak position of the SWCNT electrode as a function of time after the Br insertion, and Fig. 2.19 (B) shows the magnitude of that shift with time. The peak position in Fig. 2.19 (B) up-shifted to 1610 cm^{-1} by Br insertion. After the circuit was opened (i.e. oxidation of Br ions was stopped), the peak

position gradually decreased. However, no significant change in the peak position was observed after 30-40 min. Assuming the encapsulation amount to be proportional to the G-band shift, about 70% of the inserted Br molecules remained in SWCNTs after removing the externally applied potential. So, about 30% Br molecules might leak from SWCNTs. However, the leaking Br molecules are likely to have remained near the electrode, because no significant irreversible capacity was observed.

2.5 Conclusion

In conclusion, polyiodide ion formation in SWCNTs at low temperature is summarized as follows. First, I_2 molecules are encapsulated in SWCNTs and they start to aggregate by inter-molecular interactions. Charge-transfer from SWCNTs to the aggregated I_2 molecules adsorbed on the inner surface of SWCNTs produces polyiodide ions. At low temperature, the aggregation and polyiodide ion formation are promoted because the formation reaction is exothermic. The polyiodide ions, on the whole, would have a chain-like structure along to the hollow core of SWCNTs while the microscopic structures of the polyiodide ions should be written as small units (e.g. I_3^-, I_5^-, I_7^-).

An electrolyte redox electrochemical capacitor (EREC) using the redox reaction of bromide ions in single-walled carbon nanotubes (SWCNTs) was demonstrated. I was able to increase the cell voltage of Br EREC up to about 1.5 V without oxygen evolution. The energy density of EREC was greatly improved by using the redox reaction of bromide ions instead of iodide ions used in a previous work. It was found by monitoring the capacity retention, that SWCNT electrode can firmly hold the inserted Br molecules. I also investigated the structure and insertion site of the Br molecules inserted in SWCNTs by Raman and XRD measurements. Raman measurements revealed the existence of $(Br_2)n$ chain-like molecule and Br_3^- ions. The Br molecules are likely to be inserted into the triangular lattice space of SWCNT bundles, because the diffraction lines of SWCNT bundle structure disappeared after the Br insertion.

Chapter 3

Quinone molecules encapsulated in SWCNTs for low-temperature Na ion batteries

3.1 Overview

As discussed in chapter 1, there have some problems should be overcome in order to extend the use of Lithium ion battery (LIB) to large-scale applications. One of the problems is high cost of LIBs caused partly by the usage of rare-metals in cathode electrode materials. In order to solve this problem, Itried to develop electrodes using rare-metal-free materials like organic molecule. Quinone molecule as one kind of organic molecule has big Li ion storage capacity (258 mAh/g). However, the quinone molecules are easily dissolved in electrolyte and this demerit is very hard to solve. LIBs can't choose quinone molecules for electrode as long as researcher can't stop the dissolution of quinone molecules into electrolyte. There has a method to solve this problem, which is single-walled carbon nanotube encapsulation system. On this chapter, quinone encapsulated in two kinds of SWCNTs having different mean tube diameters are prepared and discuss the difference of the stabilization of the two samples. Charge-discharge curves of PhQ encapsulated in SWCNTs were also discussed based on the stability difference.

3.2 Experimental

Annealed and opened SWCNT-1.5 and -2.5 had been used and the preparation method mentioned on the chapter 2. PhQ molecules were inserted into the two kinds of SWCNTs by heat-treatment at 200°C of the opened SWCNTs and PhQ molecules in an evacuated glass-tube. After the heat-treatment, recovered samples were washed with

organic solvents to remove excess quinones deposited on outer side of the SWCNTs. Self-supported films (buckypaper) were obtained in this step.

The paper-form PhQ@SWCNT sample on a Cu-foil was used for Li and Na ion charge-discharge experiments. Li and Na metal foils were used as counter electrodes. 1 mol L^{-1} $LiClO_4$ in a mixture of ethylene carbonate (EC) and diethyl carbonate (DEC) solution (EC : DEC = 1 : 1 in volume ratio) and 1 mol L^{-1} $NaClO_4$ dissolved in propylene carbonate (PC) were used as electrolytes for Li and Na ion charge-discharge experiments, respectively. The charge-discharge measurements using a conventional two-electrode-type cell (Hohsen, HS-Cell) were conducted by a galvanostat (Toyo System, TOSCAT-3200). The cell assembly was performed in an Ar-filled glove box in order to avoid air exposure and contamination. Charge-discharge experiments were done with a temperature chamber (Espec SU-241) to control the temperature of the test cell.

3.3 results and discussion

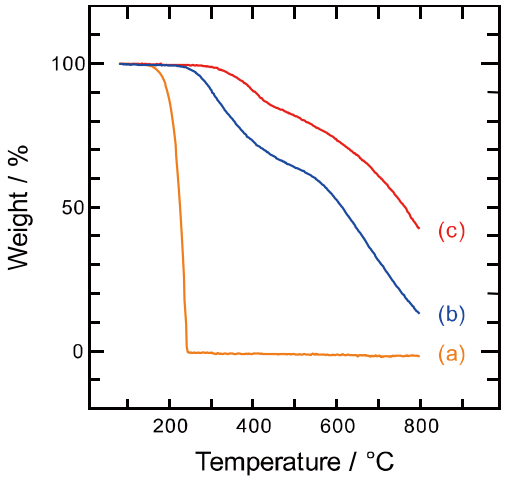

Fig. 3. 1: TG of (a) bulk PhQ, (b) PhQ@SWCNT-2.5, (c) PhQ@SWCNT-1.5.

Fig. 3.1 shows the TG curves of PhQ@SWCNT-1.5, PhQ@SWCNT-2.5, and also of bulk PhQ sample. While the weight loss due to sublimation of PhQ molecules starts at around 200 °C for the PhQ bulk sample, the threshold temperatures of weight loss of PhQ@SWCNT-1.5 and PhQ@SWCNT-2.5 are shifted toward higher temperatures.

This indicates that PhQ molecules are stabilized in SWCNTs. Since the threshold temperature of sublimation of PhQ in SWCNT-1.5 is higher than that in SWCNT-2.5, PhQ molecules might be more stabilized in smaller SWCNTs than in the larger ones. The stabilization difference of PhQ molecules in SWCNT-1.5 and -2.5 is discussed in the following section. The shifts of the threshold temperature of PhQ molecule sublimation indicate that the washing treatment after encapsulation treatment removed PhQ molecules deposited on the outer surface of SWCNTs very well, because the threshold temperature of PhQ molecules on the outer surface should be similar to that of the PhQ bulk sample. In the TG curves taken subsequent to the sublimation of PhQ molecules encapsulated in SWCNTs (Fig. 3.1), the onset of weight loss for SWCNTs is seen at 550 °C and 600 °C for PhQ@SWCNT-1.5 and PhQ@SWCNT-2.5, respectively. Since SWCNT-1.5 and SWCNT-2.5 were produced by arc-discharge and e-Dips methods, respectively, SWCNT-1.5 has slightly better crystallinity than SWCNT-2.5, and so the threshold temperature at which SWCNT-1.5 starts to burn is higher than that for SWCNT-2.5. The weight loss observed prior to the burning temperature of SWCNTs, corresponds to the amount of the encapsulated PhQ molecules. The PhQ amounts were evaluated to be 22% and 38% for SWCNT-1.5 and SWCNT-2.5, respectively.

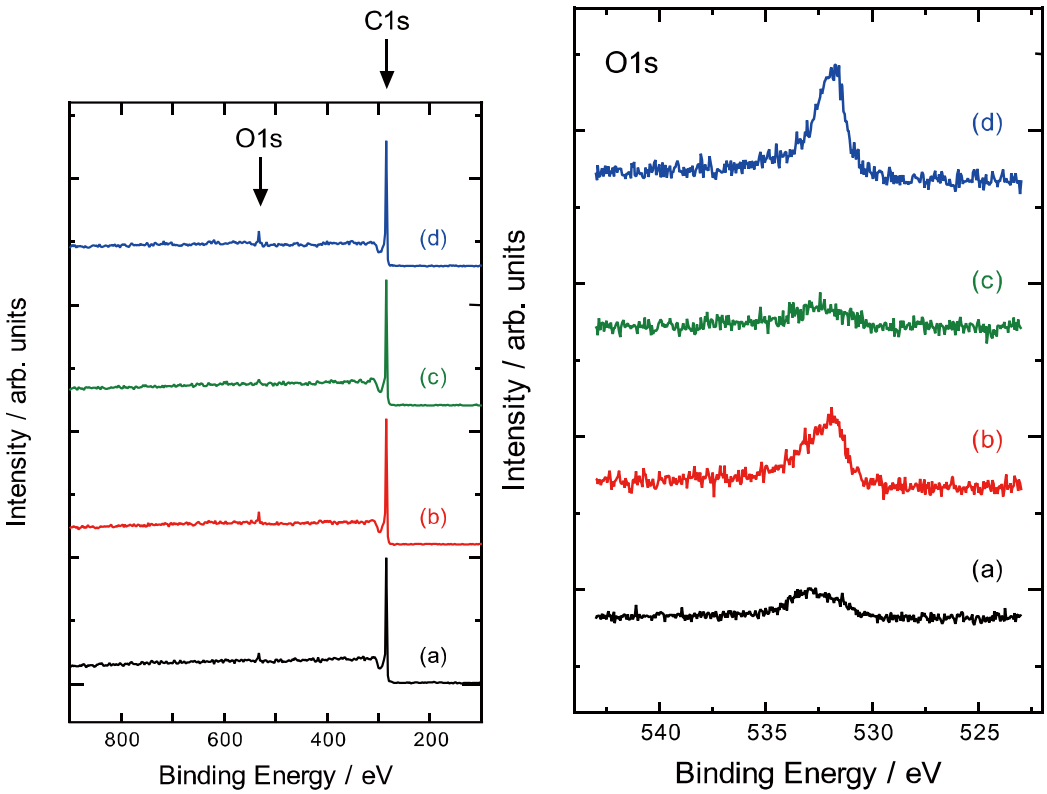

Fig. 3. 2: XPS spectra of (a) SWCNT-1.5, (b) PhQ@SWCNT-1.5, (c) SWCNT-2.5 and (d) PhQ@SWCNT-2.5.

Tab. 3. 1: O/C ratio of obtained samples estimated by the XPS spectra.

	C1s (atomic %)	O1s (atomic %)	O/C
SWCNT-1.5	96.5	3.46	0.0358
PhQ@SWCNT-1.5	95.4	4.51	0.0473
SWCNT-2.5	98.0	1.99	0.0203
PhQ@SWCNT-2.5	93.1	6.01	0.0645

The PhQ amounts can also be estimated by x-ray photoelectron spectroscopy (XPS) measurement. Figure 3.2 shows XPS spectra of SWCNT-1.5 and SWCNT-2.5 before and after the encapsulation treatment. For both samples, O/C atomic ratio increases after PhQ encapsulation treatment (table 3.1). The amounts of PhQ in SWCNT-1.5 and SWCNT-2.5 evaluated by the increase of O/C ratio after the encapsulation are 6.5% and 27.9%, respectively. Although these values are slightly different from the values determined by TG measurements, the PhQ amount in SWCNT-2.5 is greater than that in SWCNT-1.5 for both measurements. In the

following sections, the ion storage capacities of the encapsulated PhQ molecules are discussed based on the PhQ amounts determined by TG measurements, because XPS data might reflect only local surface information. As shown in figure Fig. 3.2, both O1s peak positions of SWCNT-1.5 and -2.5 shift toward the low energy side after PhQ encapsulation. The energy shift can be explained as follows. For PhQ@SWCNT samples, the observed O1s XPS spectra correspond to oxygen atoms of PhQ, namely oxygen atoms of C=O, while slightly included impurity oxygen atoms such as the oxygen atom of the C−O−H group were observed for pristine SWCNTs. On the other hand, no significant change was observed for C1s spectra by PhQ encapsulation. It indicates that the encapsulation treatment does not cause any changes to the SWCNT framework structure.

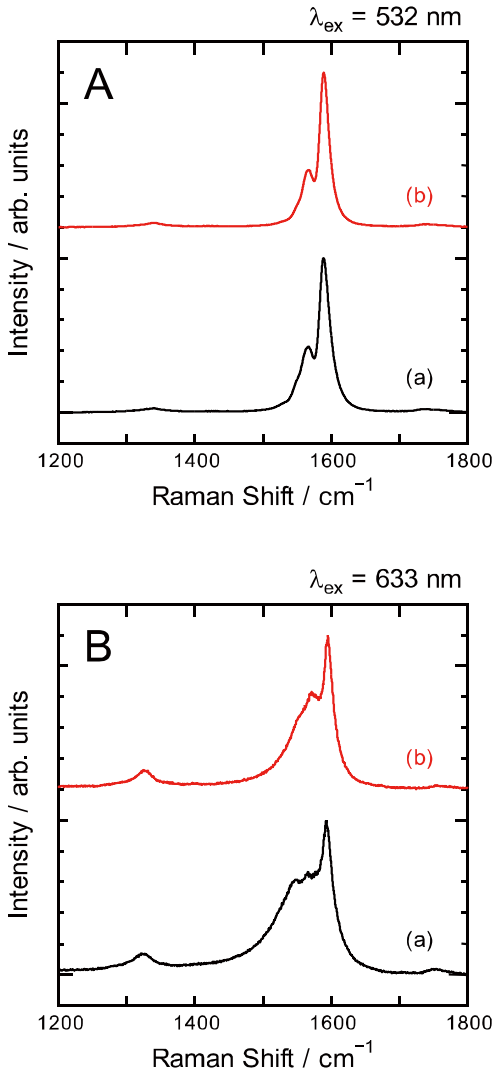

Fig. 3. 3: Raman spectra of (a) SWCNT-1.5 and (b) PhQ@SWCNT-1.5. Two types of excitation laser were used: (A) 532 nm, (B) 633 nm.

Next, I discuss the changes in Raman spectrum of SWCNTs by PhQ encapsulation. As discussed in the chapter 2, I used two kinds of lasers having the wavelengths of 532 and 633 nm. According to the Kataura plot, for both SWCNT-1.5 and -2.5 samples, semiconducting and metallic tubes are in resonance with 532 and 633 nm laser, respectively. This is consistent with the observed G-band of SWCNT-1.5 in figure 3.3(B), which shows a broad profile having a long tail on the lower wavenumber side, and is known as the Breit–Wigner–Fano (BWF) profile, typically seen for metallic SWCNTs. On the other hand, the G-band of SWCNT-1.5 observed by the 532 nm laser (figure 3.3(A)) is relatively sharp. The G-band peak profile of SWCNT-1.5 probed

using the 532 nm laser does not change by PhQ encapsulation. Contrary to that, the G-band peak profile probed with the 633 nm laser changes greatly by the encapsulation. The profile becomes sharp, by losing the BWF feature after the encapsulation. As chapter 2 discussed, The BWF feature comes from the plasma oscillation of free electrons of metallic tubes. Therefore, the loss of the BWF feature means the decrease of the number of free electrons in metallic tubes by PhQ encapsulation. It indicates charge-transfer from metallic SWCNTs to the encapsulated PhQ molecules and This transfer also occurred in the sample of iodine molecules encapsulated in SWCNTs. Since active electrons near the Fermi level of metallic tubes are easier to move to PhQ molecules, the charge-transfer reaction is likely to have occurred only from metallic tubes, and not from semiconducting tubes. On the other hand, in the case of SWCNT-2.5, the G-band peak profile does not change by PhQ encapsulation regardless of the excitation laser (figure 3.3). Namely, the charge-transfer reaction does not seem to occur from metallic nor from the semiconducting SWCNTs of PhQ@SWCNT-2.5. The reason for the threshold temperature of PhQ sublimation of SWCNT-1.5 being higher than that of SWCNT-2.5, may be related to the stabilization of PhQ molecules in SWCNTs, as a result of the charge transfer induced electrostatic interaction between charged SWCNTs and PhQ molecules of PhQ@SWCNT-1.5, in addition to the stronger interaction that smaller tubes have with the encapsulation molecules.

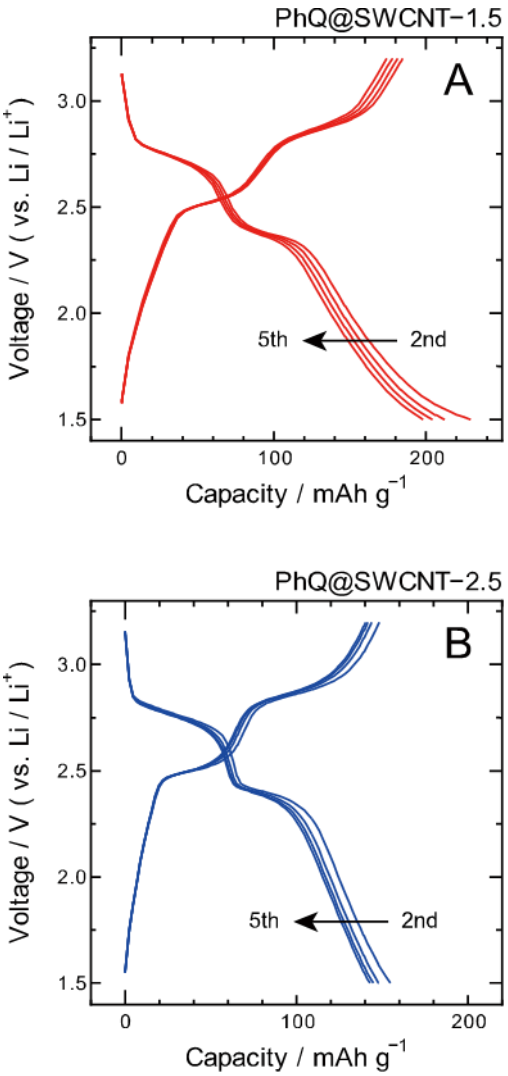

Fig. 3. 4: Charge-discharge curves of the (A) PhQ@SWCNT-1.5 and (B) PhQ@SWCNT-2.5 electrodes used for LIB. The measurements were performed at room temperature. Horizontal axes are calculated from the weight of PhQ molecules in the electrodes. All the measurements were performed at a constant current density of 100 mA/g.

Here, I discuss Li ion charge–discharge properties of PhQ@SWCNT-1.5 and -2.5 (Fig. 3.4). As discussed in a previous report, the capacity fading with charge–discharge cycle observed for the bulk PhQ sample diminished greatly by encapsulation [34]. The improvement of the cycle performance was found for both SWCNT-1.5 and SWCNT-2.5. However, the reversible capacities of PhQ@SWCNT-1.5 and PhQ@SWCNT-2.5 are quite different. In the case of PhQ@SWCNT-1.5, the observed reversible capacity

is almost as high as the theoretical capacity of the PhQ molecule (258 mAh g^{-1}), while the reversible capacity of PhQ@SWCNT-2.5 is about a half of the theoretical value. In other words, only half of the encapsulated PhQ molecules in SWCNT-2.5 worked as electrode materials. The low utilization rate may be explained by kinetic reasons. However, the reversible capacity observed under a very low charging rate is still far from the theoretical value. Therefore, I need to consider other reasons. As I discussed with TG and Raman data, PhQ molecules strongly interact with SWCNT-1.5 while PhQs are loosely bound with SWCNT-2.5. Due to the loose interaction, some PhQ molecules in SWCNT-2.5 cannot form a current flow path, and cannot work as electrode materials.

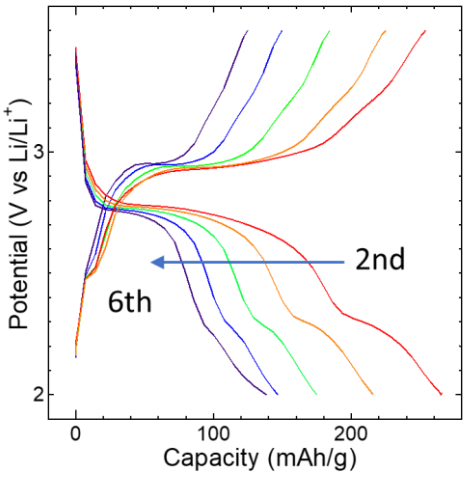

Fig. 3. 5: Charge-discharge curves of bulk PhQ electrode. The measurement was performed at a constant current density of 100 mA/g.

Next I will examine the charge–discharge curve profiles in more detail. Two clear plateaus at 2.8 and 2.4 V are seen on the discharge profile of the PhQ bulk sample (figure 3.5), and both are quite flat in shape. On the other hand, although two steps are observed on discharge profiles of PhQ@SWCNT-1.5 and PhQ@SWCNT-2.5 (figure 3.4), they are not quite flat, but rather have the form of gentle slopes. In particular, the gradient of the slope of SWCNT-1.5 is steeper than that of SWCNT-2.5. Also, the threshold potential of lithiation of PhQ@SWCNT-1.5 is slightly higher than that of

PhQ@SWCNT-2.5. These differences may be attributed to the difference in the interaction between the encapsulated molecules and their host SWCNTs.

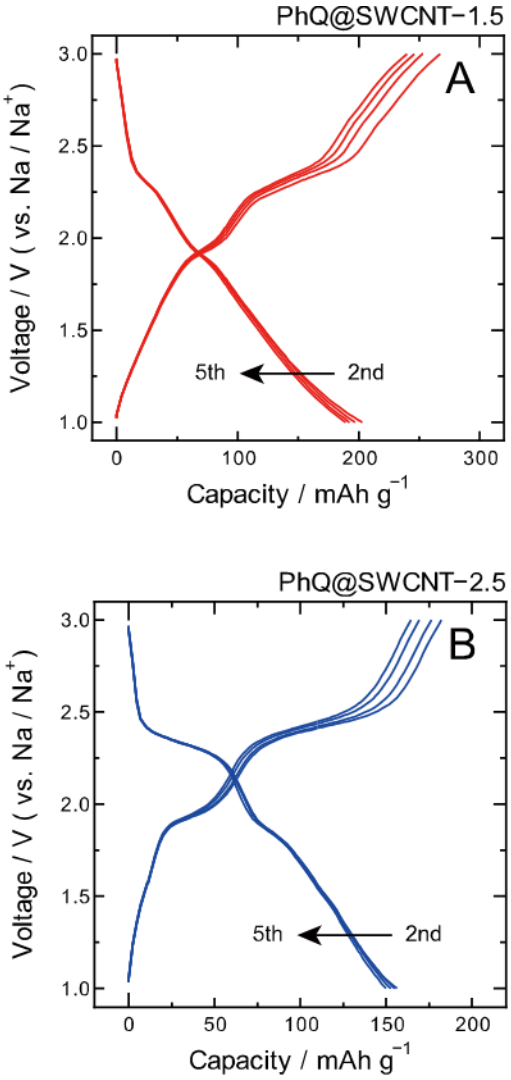

Fig. 3. 6: Charge-discharge curves of the (A) PhQ@SWCNT-1.5 and (B) PhQ@SWCNT-2.5 electrodes used for SIB. The measurements were performed at room temperature. Horizontal axes are calculated from the weight of PhQ molecules in the electrodes. All the measurements were performed at a constant current density of 100 mA/g.

One of the purposes of my investigation is to elucidate the SIB electrode properties of PhQ@SWCNT. As shown in Fig. 3.6, both PhQ@SWCNT-1.5 and -2.5 can work as SIB electrodes. Their Na ion adsorption properties (reversible capacities and discharge

profiles) are quite similar to their Li ion adsorption properties. Although many materials are known to work as both Li and Na ion battery electrodes, the adsorption properties for Li and Na ions are usually very different [70,71]. In particular, the electrode materials using nanospace or alloy reactions often show very different properties for Li and Na ions, because their ion storage reactions are strongly affected by the ion size [72]. However, the present PhQ@SWCNT electrodes show almost the same ion adsorption properties for both Li and Na ions. This would be explained by ion adsorption path of PhQ@SWCNT. Ions in electrolyte should be inserted into SWCNTs through the tube edge and migrate inside the tubes. Since the diameter of the present SWCNTs are much greater than the Li and Na ion sizes, the adsorption path does not discriminate between these two ions. Therefore, the reversible capacities and the charge–discharge profiles of PhQ@SWCNT are quite similar for Li and Na ions. It indicates that PhQ@SWCNT might be applicable to other kinds of ion battery electrodes as well. As shown in figure 3.6, it was found that the charge capacities were slightly greater than the discharge capacities in each cycle. It was also observed that the decrease of the charge capacity with cycle was much greater than that of the discharge capacity. These results indicate that not only a Na ion extraction reaction but also other kinds of irreversible reactions should be occurr in the discharge process and that the amount of the materials causing the irreversible reaction decreased with the charge–discharge cycles. Although I could not reveal what caused the irreversible reaction, it would be plausible that some kinds of impurities might be included in the electrolyte used in the Na ion experiments because such an over-charge phenomenon was not observed in the case of the Li ion experiments.

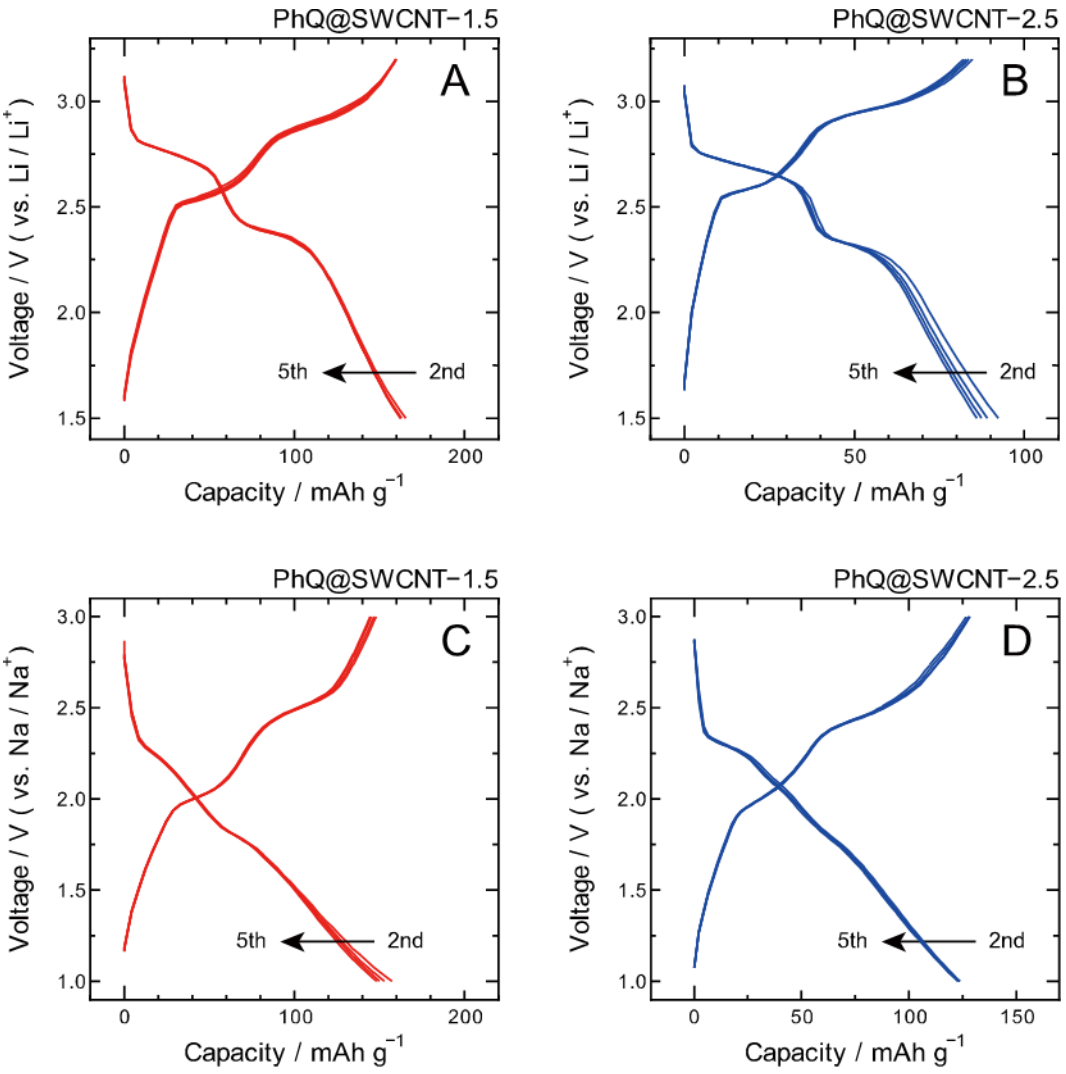

Fig. 3. 7: Charge-discharge curves of the (A, C) PhQ@SWCNT-1.5 and (B, D) PhQ@SWCNT-2.5 electrodes observed at 0°C. Panel A and B shows Li-ion storage properties. Panel C and D shows Na-ion storage properties. Horizontal axes are calculated from the weight of PhQ molecules in the electrodes. All the measurements were performed at a constant current density of 100 mA/g.

Fig.3.7 shows Li and Na ion charge–discharge curves of PhQ@SWCNT observed at a low temperature of 0°C. Firstly, for Li ions, both PhQ@SWCNT-1.5 and PhQ@SWCNT-2.5 can adsorb and desorb ions reversibly. It is well known that low temperature battery performance of commercial LIBs is not very good. Therefore, the encapsulation system would be a good approach to solve the low temperature problem. However, the reversible capacities of PhQ@SWCNT-1.5 and PhQ@SWCNT-2.5

observed at 0°C are much smaller than those at RT. The capacity decrease might be due to kinetic problems, such as the increase of the internal resistance. In fact, the capacity observed under a very slow charging rate was as high as the theoretical capacity even at 0°C. Interestingly, the capacity decrease at low temperatures for Na ions is very small for both PhQ@SWCNT-1.5 and PhQ@SWCNT-2.5, especially the reversible capacity of PhQ@SWCNT-2.5 at 0°C, which is almost as high as that at RT. It is probable that Na ions can diffuse in SWCNT-2.5 easily even at a low temperature. Although I do not have any experimental evidence that supports such facilitated diffusion, the present results clearly suggest that PhQ@SWCNT-2.5 would be a good candidate for low temperature SIB electrode materials.

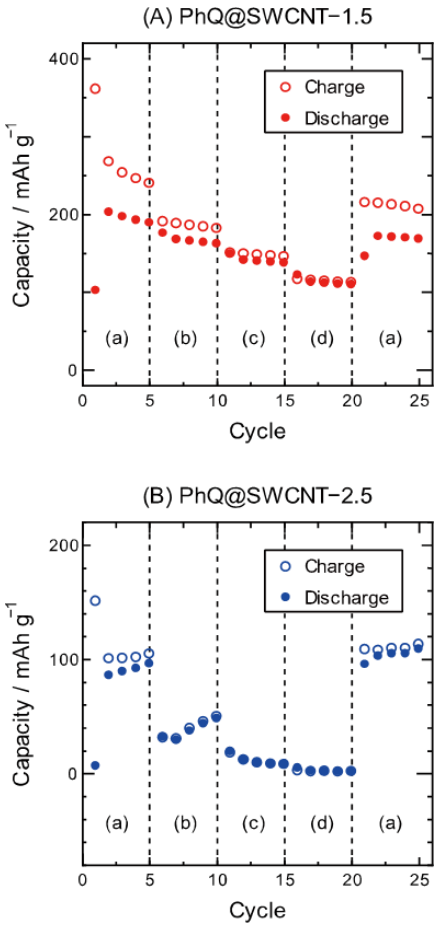

Fig. 3. 8: Room temperature cycling performance of the (A) PhQ@SWCNT-1.5 and (B) PhQ@SWCNT-2.5 electrodes used for SIB at current densities of (a) 100, (b) 200, (c) 400, (d) 800 mA g/1

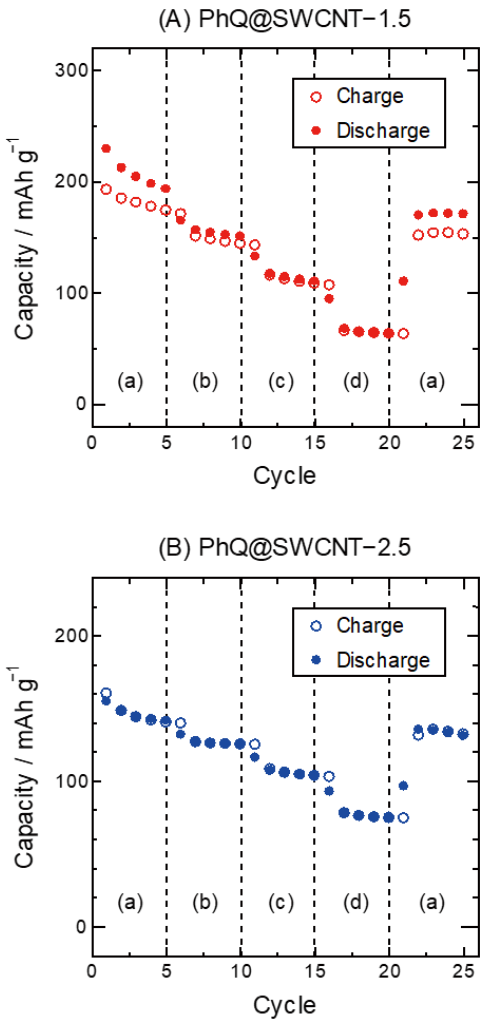

Fig. 3. 9: Room temperature cycling performance of the (A) PhQ@SWCNT-1.5 and (B) PhQ@SWCNT-2.5 electrodes used for LIB at current densities of (a) 100, (b) 200, (c) 400, (d) 800 mA/g

In order to further understand the SIB electrode behavior of PhQ@SWCNT samples, I investigated their rate and cycle performance. As shown in Fig. 3.8 and Fig. 3.9, PhQ@SWCNT-1.5 shows a monotonous capacity decrease with the charge–discharge cycle regardless of the charging rate, while PhQ@SWCNT-2.5 shows an increase in the capacity with cycle for some charging rates. As discussed already, PhQ molecules in SWCNT-2.5 are loosely bound with SWCNTs. Some of the molecules do not provide current flow path and are not used for ion storage. However, during charge–discharge cycles, such inactive PhQ molecules might become activated. The weak

interaction between PhQ molecules and SWCNTs in SWCNT-2.5 would allow the position changes of the encapsulated PhQ molecules.

3.4 Conclusions

In conclusion, I have performed Li and Na ion charge–discharge experiments of PhQ molecules encapsulated in SWCNT-1.5 and -2.5, at RT and 0°C. In order to understand the manner at which PhQ molecules are stabilized in SWCNTs, I investigated the threshold temperature of sublimation of PhQ molecules encapsulated in SWCNTs by TG measurements. It was found that the threshold temperature of PhQs in SWCNT-1.5 is higher than that of PhQs in SWCNT-2.5. It was also found by analysis of the Raman G-band peak profiles, that charge transfer from metallic SWCNTs to PhQ molecules should occur in the case of SWCNT-1.5. The electrostatic interaction between charged SWCNTs and PhQ molecules, induced by the charge-transfer reaction, would partly contribute to the stabilization of PhQ molecules in SWCNTs. For Li-ion charge–discharge experiments, the observed reversible capacity of PhQ@SWCNT-1.5 was almost as high as the theoretical capacity of the PhQ molecules, while that of PhQ@SWCNT-2.5 was about half of the theoretical capacity. On the other hand, the two samples showed similar behavior for Na ions storage. Since the Na ion reversible capacity of PhQ@SWCNT-2.5 measured at a low temperature of 0°C remained as high as that measured at RT, PhQ@SWCNT-2.5 should be an interesting candidate as an electrode material for a low temperature Na ion battery.

Chapter 4

Alkali Metal Ion Storage of Quinone Molecules Grafted on Single-walled Carbon Nanotubes at Low Temperature

4.1 Overview

On the chapter 3, the encapsulation treatment of PhQ molecules in single-walled carbon nanotubes (SWCNTs) was a good method to prevent the dissolution and improve the cycle performance of PhQ electrode. However, unfortunately, this method could not stop the capacity fading completely. On the chapter 4, I tried to graft PhQ molecules onto SWCNTs in order to obtain higher stability.

4.2 Experimental Methods

I purchased all the chemicals used in the present study: 9,10-anthraquinone (AQ) (Wako pure chemical industries), and 9,10-PhQ (Sigma-Aldrich). Two kinds of SWCNT samples SWCNTs-1.0 and SWCNTs-2.5 were also purchased (SWCNTs-1.0: NanoIntegris Inc., SWCNTs-2.5: Meijo Nanocarbon). For SWCNT samples, I performed purification treatment using acid and annealing treatment to obtain higher crystallinity. The detailed purification procedure is described in chapter 2.

As SWCNTs having huge π-conjugation system should be chemically very stable, it is not very easy to do chemical modification for SWCNTs. First, PhQ powder sample was refluxed with nitric acid at 130°C for 1 h to obtain nitrated PhQ. Then the obtained nitrated PhQ was dissolved in 2% NaOH aqueous solution, and excess amount of sodium hydrosulfite was added to the solution to replace the nitro groups by amino groups. Subsequently, PhQs were grafted onto SWCNTs by diazo coupling reactions

as shown in Fig. 4.1 (a). For comparison, I also prepared PhQ encapsulated SWCNTs (PhQ@SWCNTs) using a process described in chapter 3

PhQ derivatives were characterized by Fourier transform infrared spectroscopy (FT-IR) and nuclear magnetic resonance (NMR) measurements. The final products (PhQ/SWCNT composites) were thoroughly investigated by high resolution transmission electron microscope (HRTEM), scanning electron microscopy (SEM), Raman spectroscopy, XRD, thermogravimetric (TG) analysis, and X-ray photoelectron spectroscopy (XPS) measurements.

The paper-form PhQ/SWCNT sample obtained by vacuum filtration was used for Li and Na ion charge-discharge experiments. Li and Na metal foils were used as counter electrodes. 1 mol L^{-1} $LiClO_4$ dissolved in a mixture of ethylene carbonate (EC) and diethyl carbonate (DEC) solution (EC : DEC = 1 : 1 in volume ratio) and $NaClO_4$ dissolved in a mixture of EC and DEC solution (EC : DEC = 1 : 1 in volume ratio) were used as electrolytes for Li and Na ion charge-discharge experiments, respectively. The charge-discharge measurements using a conventional two-electrode-type cell (Hohsen, HS-Cell) were conducted using a galvanostat (Toyo System, TOSCAT-3200). The cell was assembled in an Ar-filled glove box in order to avoid air exposure and contamination. Charge-discharge experiments were done inside a thermostatic chamber (Espec, SU-241) to control the temperature of the test cell.

Density functional theory (DFT) calculations were performed using Gaussian 09 software [73]. Here, I used the B3PYP exchange-correlation hybrid functional [74] with Dunning's double-zeta correlation consistent basis sets [75] (cc-pVDZ).

4.3 Results and discussion

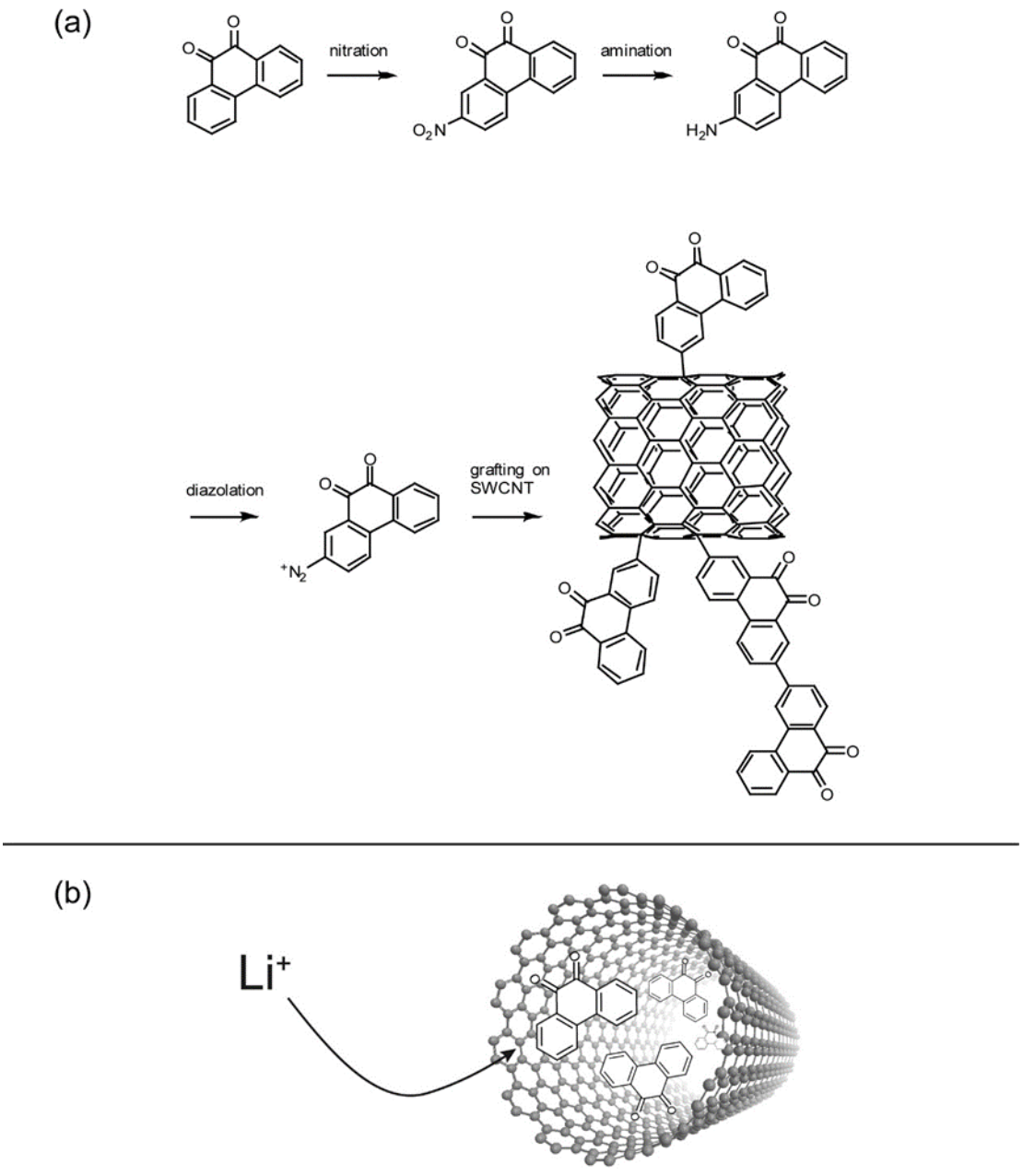

Fig. 4. 1: (a) Preparation of PhQ-grafted SWCNT using diazo coupling reaction. (b) Schematic structure of PhQ@SWCNT electrode.

As shown in the Fig. 4.1. In the case of encapsulation system (Fig. 4.1 (b)), electrolyte ions should approach to the encapsulated quinone molecules through open tube-edges. On the other hand, the grafted quinone molecules (Fig. 4.1 (a)) seem to be more easily accessible to the ions. I investigated the Li ion and also the Na ion storage

properties of the synthesized sample of PhQ grafted on SWCNT (PhQ/SWCNT). If PhQ/SWCNT can store Na ion effectively, it can be used as Na ion battery (SIB) electrode material. I also investigated the low temperature performance of PhQ/SWCNT electrode for Li and Na ions. Furthermore, density functional theory (DFT) calculations were performed to understand the detailed features of charge-discharge profiles of PhQ/SWCNT electrode. Based on the calculation, I discussed the discharge potential difference for Li and Na ions.

Although I performed AQ and PhQ grafting treatments for the two samples, in this chapter, I discuss mainly the electrode properties of PhQ-grafted SWCNT-2.5 sample (PhQ/SWCNT-2.5) in comparison with other combinations. As discussed on chapter 2, since SWCNT-2.5 has less defective, narrow diameter distribution, and well bundled form, its physical characterization reveals a weak Raman D-band peak and very clear X-ray diffraction peaks (Fig. 2.4 and Fig. 2.5). The high purity was also confirmed by TEM observation (Fig. 2.6). I analyzed the bundle diameter size using the TEM picture and estimated a mean bundle diameter of about 35 nm (Fig. 4.2).

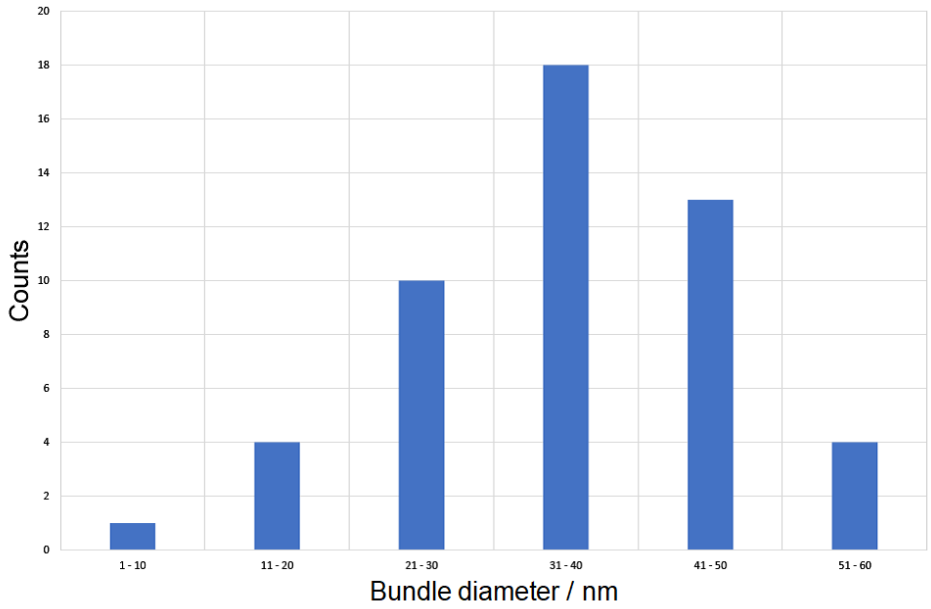

Fig. 4. 2: Diameter distribution of bundled SWCNT-2.5 obtained by an analysis of TEM images.

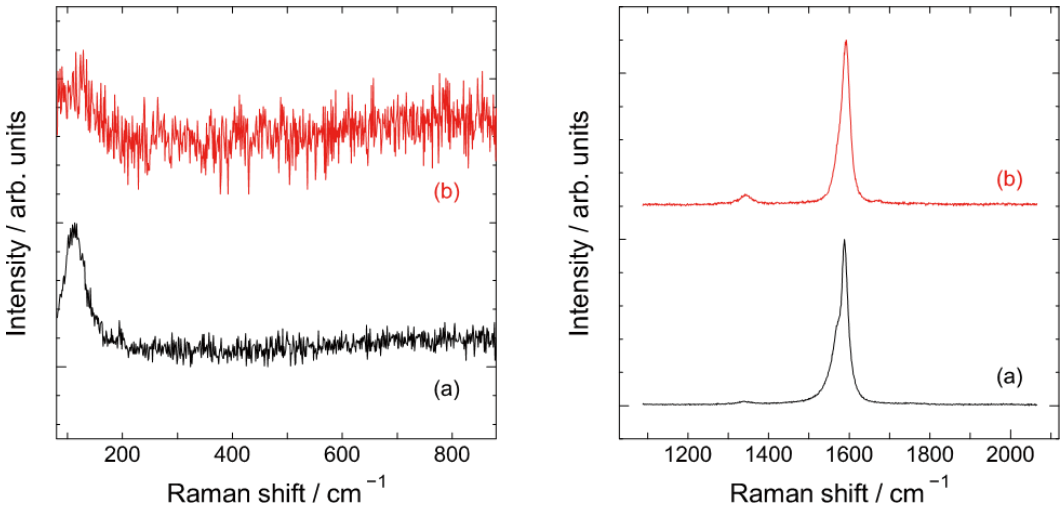

Fig. 4. 3: Raman spectra of (a) SWCNT-2.5 and (b) PhQ/SWCNT-2.5

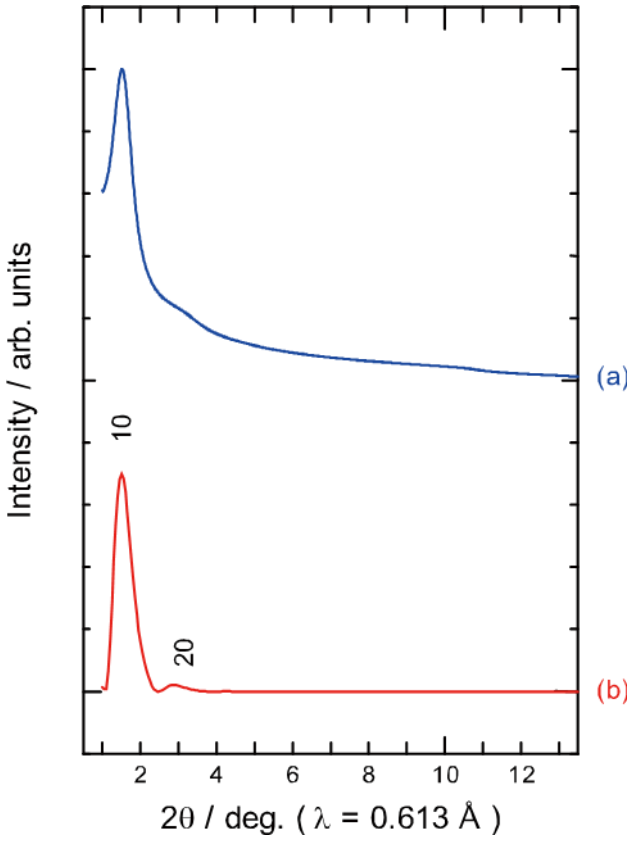

Fig. 4. 4: (a) Observed and (b) simulated synchrotron powder XRD pattern of SWCNT-2.5.

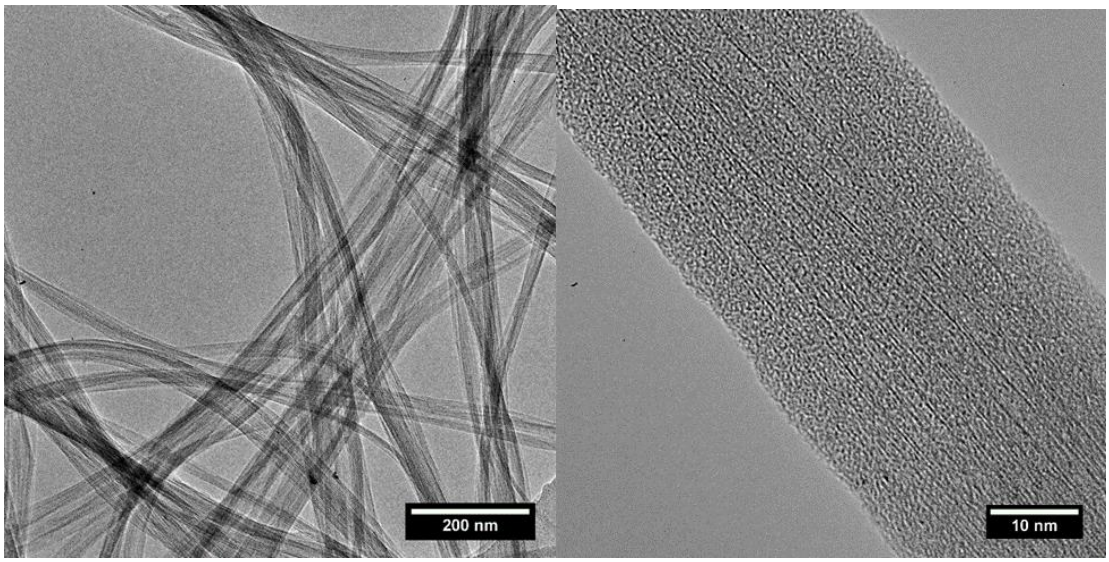

Fig. 4. 5: HRTEM images of PhQ/SWCNT-2.5.

Fig. 4.3 shows that the intensity of the D-band peak of SWCNT-2.5 increases by the PhQ grafting treatment. This increase indicates the formation of sp^3 carbon on the surface of SWCNTs by the reaction with diazo-PhQ molecules. On the other hand, I could not observe any significant changes in XRD pattern of the quasi two-dimensional hexagonal lattice of SWCNT-2.5 bundle after the grafting treatment, which means that the bundle form is maintained after the PhQ grafting treatment. Judging from these observations, I conclude that PhQ molecules were grafted on the outer SWCNTs of the bundle surface, and that the inner SWCNTs were kept as they were. I also performed TEM observation of PhQ/SWCNT-2.5 sample. However, I could not see the PhQ grafted phase in the HRTEM pictures of PhQ/SWCNT-2.5 (Fig. 4.5).

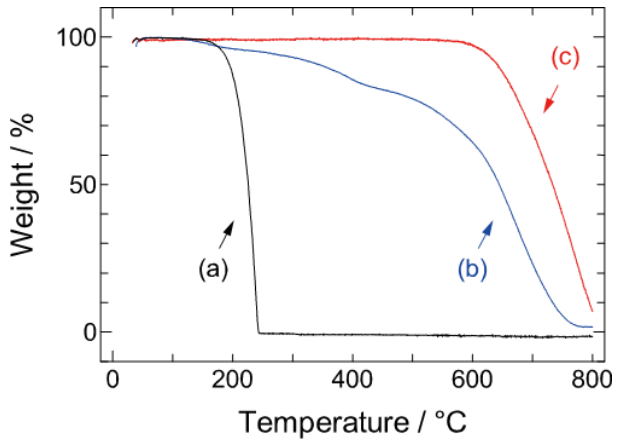

Fig. 4. 6: TG curves of (a) bulk PhQ, (b) PhQ/SWCNT-2.5, and (c) SWCNT-2.5.

The amount of PhQ grafted on SWCNTs was evaluated by two approaches: TG and XPS. The sublimation temperature of PhQ molecule is about 200°C, and the drastic weight loss from 200°C was clearly observed in TG curve in the case of PhQ crystal (Fig. 4.6). On the other hand, the oxidation temperature of the untreated SWCNT-2.5 is about 590°C as shown in Fig. 4.6. The rather high oxidation temperature also confirms the high crystallinity of SWCNT-2.5. Since the temperature difference of the two TG threshold temperatures of PhQ and SWCNT is very large (~400°C), the amount of PhQ in PhQ/SWCNT-2.5 sample should be evaluated by TG measurement. In fact, a two-step TG curve was observed for PhQ/SWCNT-2.5 as expected. However, the observed two steps are not very clear because PhQ molecules are stabilized by the connection with SWCNTs, and the crystallinity of SWCNTs should be lowered by the grafting. Therefore, it is very difficult to determine the critical temperature needed to evaluate the PhQ content in the sample. If I assume the SWCNT oxidation threshold temperature of PhQ/SWCNT-2.5 to be 590°C as that of the untreated SWCNT-2.5, the PhQ content can be determined as 33 wt.%. Although this value overestimates the amount of grafted PhQ, because some of the SWCNTs of PhQ/SWCNT-2.5 should have lower oxidation temperature due to the defects formed by PhQ grafting, I can treat this value as the maximum PhQ content in the sample.

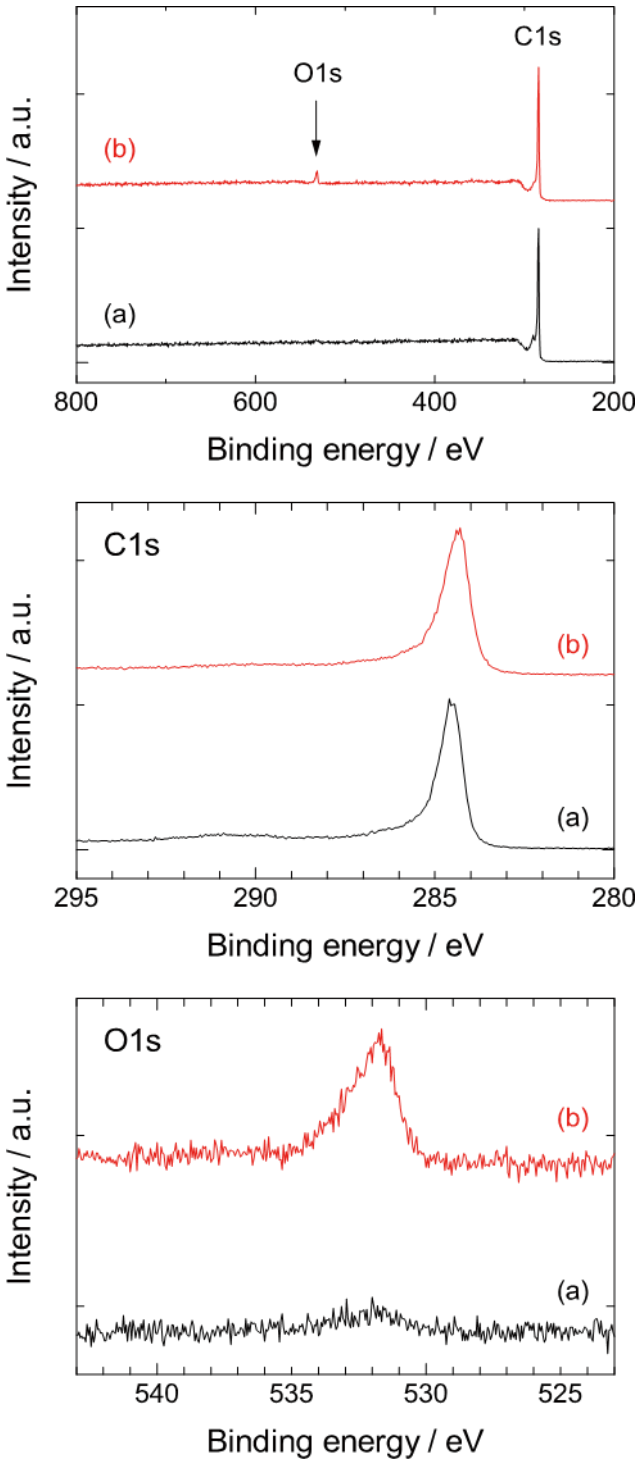

Fig. 4. 7: XPS spectra of (a) SWCNT-2.5 and (b) PhQ/SWCNT-2.5.

I also performed XPS measurements to evaluate the PhQ content as I did for the SWCNT encapsulation sample (Fig. 4.7). As explained in chapter 3, the PhQ content can be estimated by the increase of O/C atomic ratio. The O1s peak on the XPS spectrum of SWCNT-2.5 drastically changed by PhQ grafting. For PhQ/SWCNT-2.5,

the O1s peak corresponding to oxygen atoms of PhQ, namely oxygen atoms of C=O. The signal from C=O group was observed at around 284.8 eV in the C1s spectra. On the other hand, slightly included impurity oxygen atoms such as oxygen atom of C-O-H group were observed for the untreated SWCNT-2.5 at around 286.7 eV. The PhQ amount of PhQ/SWCNT-2.5 evaluated by the increase of O/C ratio is 28.1%. Although this value is very close to the value determined by TG measurement, I should note that the value determined by XPS also overestimates the PhQ content, because of the following reason: as mentioned above, PhQ molecules are grafted only on the outer SWCNTs of the bundles having mean diameter of 35 nm. Since Al Kα X-ray was used for the XPS measurement, I could not get any information from SWCNTs in the inner part of the bundle. Therefore, although I could not obtain the correct PhQ amount value by either TG or XPS measurements, I estimate that the PhQ content should be less than 33 wt.%.

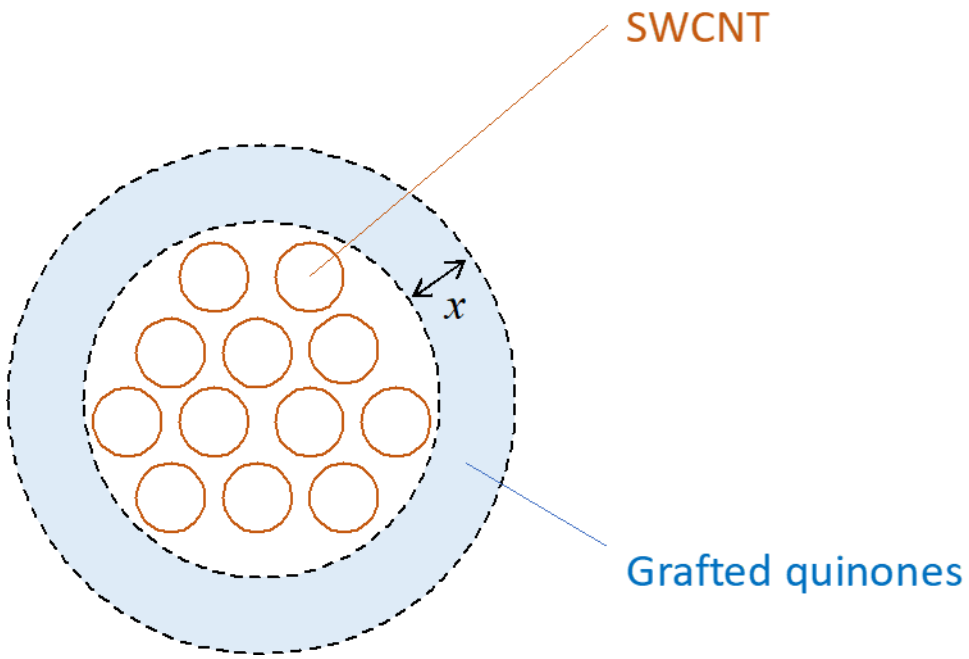

Fig. 4. 8: Schematic structure of quinone molecules grafted on SWCNTs.

Now I discuss how PhQ molecules are grafted on SWCNT-2.5. The mean tube diameter D and lattice constant *a* of the quasi two-dimensional bundle hexagonal lattice

were determined from XRD simulation, and had the values of 2.5 and 2.8 nm, respectively (Fig. 4.4). The tube-to-tube distance, calculated from *D* and *a*, is 0.3 nm, and the value is very reasonable for a SWCNT bundle. Using these values, I calculated the bundle to contain one SWCNT per 6.79 nm^2 of its cross section. Therefore, an average bundle having diameter of 35 nm should consist of about 142 SWCNTs. Here I think about a structural model of PhQ/SWCNT-2.5 such that a layer of PhQ *x* nm in thickness covers the SWCNT bundle of 35 nm diameter (Fig. 4.8). Assuming the PhQ content to be 33 wt.% and the density of PhQ layer to be 1.4g cm^{-3} as that of PhQ crystal, the layer thickness x is calculated to be 1.3 nm. Since this *x* value is much larger than PhQ molecular size, the PhQ layer should not be a monolayer. The grafting method used in the present study can create bonds not only between PhQ molecules and SWCNTs, but also between PhQ molecules themselves. Namely, polymerized PhQ molecules having average thickness of 1.3 nm are attached to the outer surface of the SWCNT bundle. Unfortunately, the thickness of the PhQ polymer is too thin to be observed by HRTEM (Fig. 4.5).

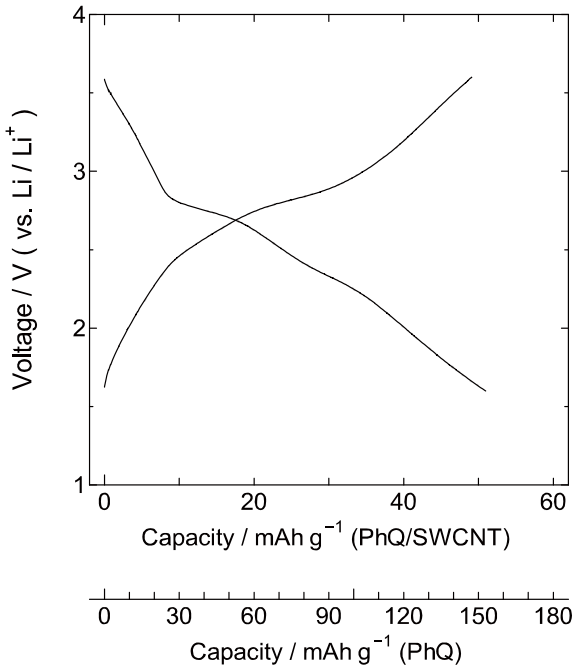

Fig. 4. 9: Room temperature charge/discharge curves of PhQ/SWCNT-2.5 used for LIB. The measurement was performed at a constant current density of 100mA/g, where "g" means total weight of the composite electrode (PhQ/SWCNT-2.5).

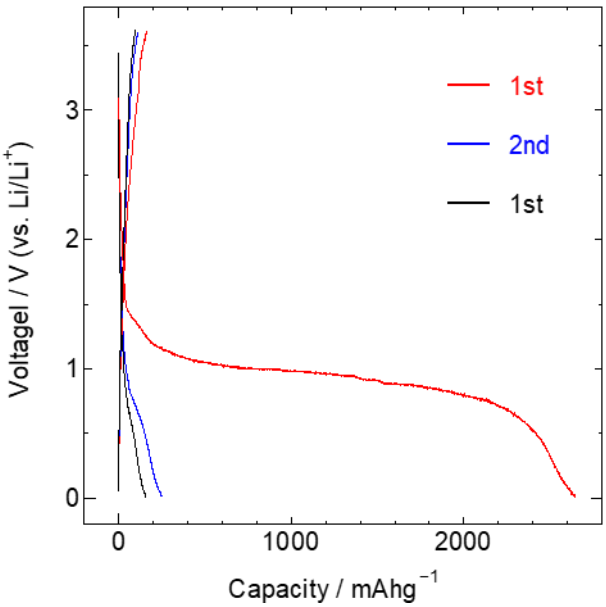

Fig. 4. 10: Room temperature galvanostatic charge/discharge curves of SWCNT-2.5 used for LIB.

From here I discuss the electrode properties of PhQ/SWCNT-2.5. First, I found that PhQ/SWCNT-2.5 can adsorb/desorb Li ions reversibly as shown in Fig. 4.9. Two step plateaus are clearly visible on the charge-discharge profiles at around 2.4 and 2.8V, which are characteristic features of PhQ electrode, indicating that the PhQ molecules grafted on SWCNTs can work as Li ion battery electrode materials. Here I note that lithium storage capacity of SWCNTs in this voltage region is negligible because lithium insertion/extraction to/from carbon materials generally occurs at a lower potential region less than 1.0 V vs. Li/Li^+ (see Fig. 4.10). In Fig. 4.9, the charge-discharge capacity values per the total amount of electrode and also per unit PhQ weight are shown. The capacity value per PhQ weight is calculated assuming 33wt.% PhQ content. Although the reversible capacity of 150 mAh/g shown in Fig. 4.9 was smaller than the theoretical capacity of PhQ molecule (258 mAh/g), it should be noted that the 33wt.% used for the Fig. 4.9 is probably overestimated. Taking that into account, I can assume that most of PhQ molecules even in their polymerized form could adsorb Li ions, and that electron transfer through the polymer to SWCNT should be possible as well.

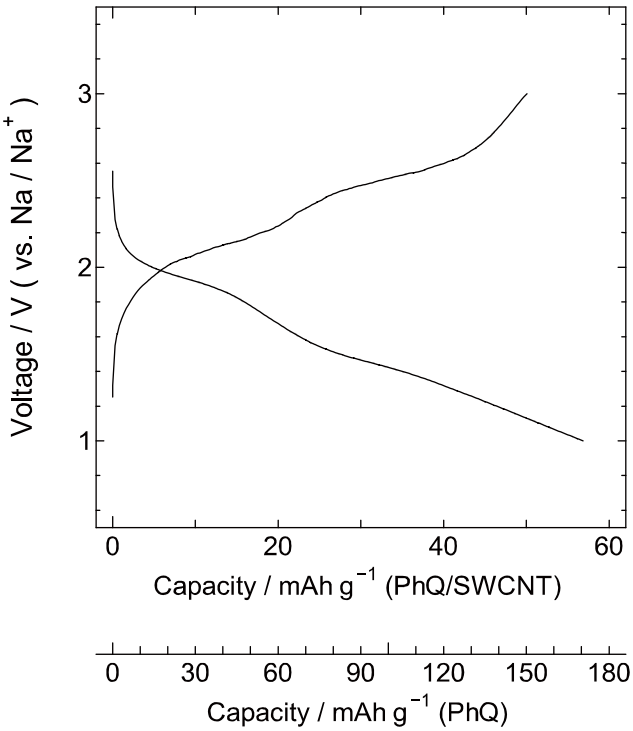

Fig. 4. 11: Room temperature charge/discharge curves of PhQ/SWCNT-2.5 used for SIB. The measurement was performed at a constant current density of 100mA/g, where "g" means total weight of the composite electrode (PhQ/SWCNT-2.5).

As shown in Fig. 4.11, the charge-discharge curves of PhQ/SWCNT-2.5 observed for Na ions are almost similar to those observed for Li ions. Using the redox potentials of Li/Li^+ (−3.05 V) and Na/Na^+ (−2.73 V), I can compare the plateau potential of the discharge curves of PhQ/SWCNT-2.5 for Li and Na ions. It was found by this analysis that the discharge potential for Na ion is about 700 mV lower than that for Li ion, although the discharge profiles for Li and Na ions are quite similar. The discharge potential difference will be discussed later.

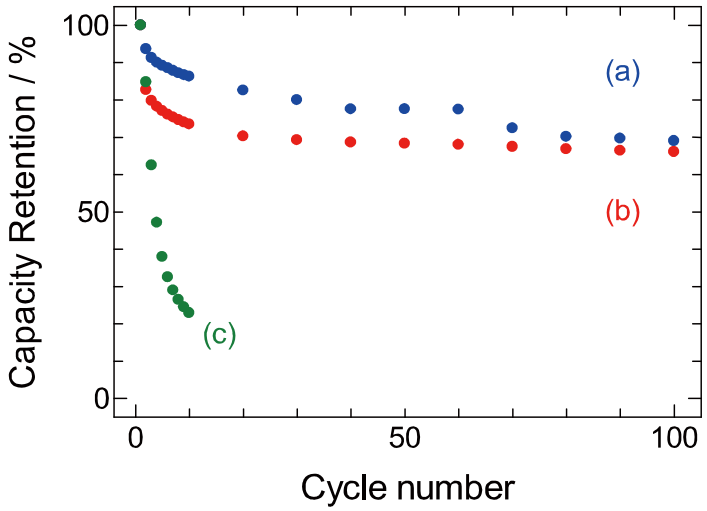

Fig. 4. 12: Cycle performance of (a) PhQ/SWCNT-1.0, (b) PhQ@SWCNT-2.5, and (c) simple mixture of PhQ and carbon black electrode used for LIB.

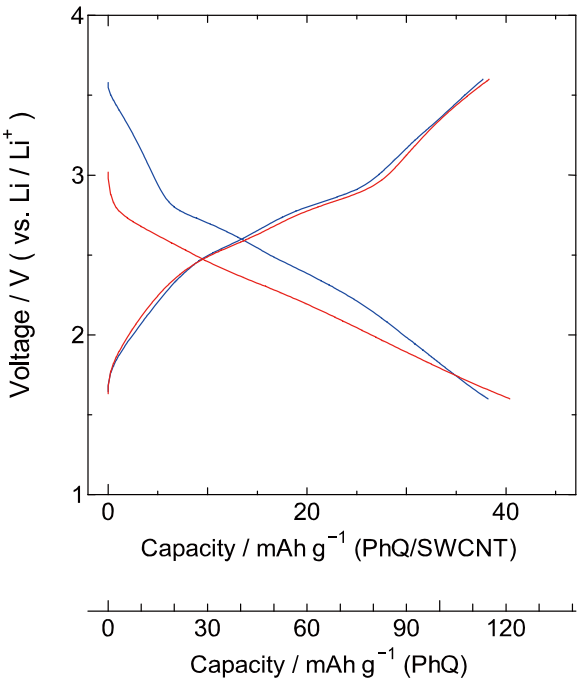

Fig. 4. 13: Room temperature galvanostatic charge/discharge curves of PhQ/SWCNT-1.0 used for LIB. Red and blue lines shows 1st and 50th cycle data, respectively. The measurement was performed at a constant current density of 100mA/g, where "g" means total weight of the composite electrode (PhQ/SWCNT-1.0).

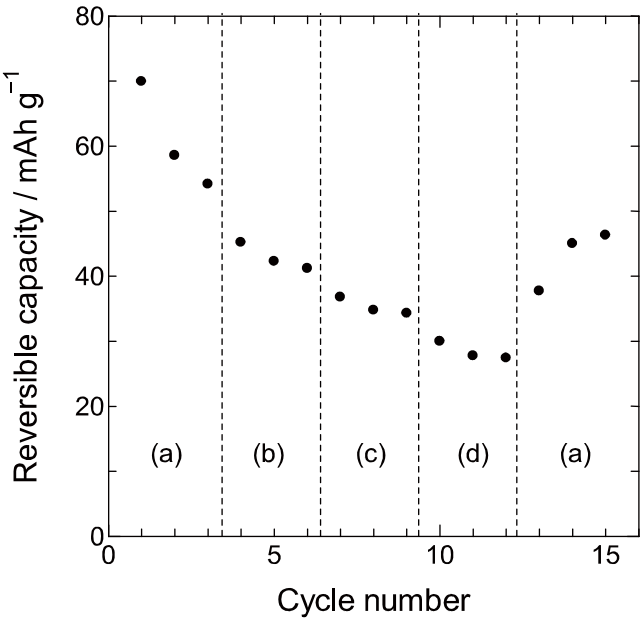

Fig. 4. 14: Room temperature charge/discharge performance of PhQ/SWCNT-2.5 used for SIB at current densities of (a) 20, (b) 50, (c) 100, and (d) 200 mA/g. Capacity values are calculated from the total weight of the composite electrode (PhQ/SWCNT-2.5).

Fig. 4.12 shows the 100 cycles charge-discharge data of PhQ/SWCNT-2.5 for Li-ion battery. In the case of bulk PhQ sample with carbon black conductive additive, severe capacity fading was observed in a few cycles because of the dissolution of PhQ molecules into electrolyte. In the chapter 3, The dissolution of PhQ molecules was suppressed by the encapsulation treatment. The capacity loss of PhQ/SWCNT-2.5 is much smaller than that of PhQ@SWCNT-2.5, because PhQs are covalently connected to SWCNTs. as shown in Fig. 4.12, it was found that the PhQ grafting is much more effective for the improvement of cycle performance than the encapsulation treatment. Clear plateaus originating from the electrochemical behavior of grafted PhQ molecules were maintained even after 50 cycles as shown in Fig. 4.13. On the other hand, the rate performance of PhQ/SWCNT-2.5 shown in Fig. 4.14 is not very good, although it is reported that the redox reactions of quinone molecules including PhQ are very fast [76-79]. The internal resistance of PhQ/SWCNT-2.5 probably increases due to the long-winded electron path through polymerized PhQs. As shown in Fig. 4.12(a), a small

capacity drop was observed between 50 and 60 cycles. The reason why the capacity dropped is not clarified. However, PhQ/SWCNT showed higher capacity than PhQ@SWCNT after the capacity drop.

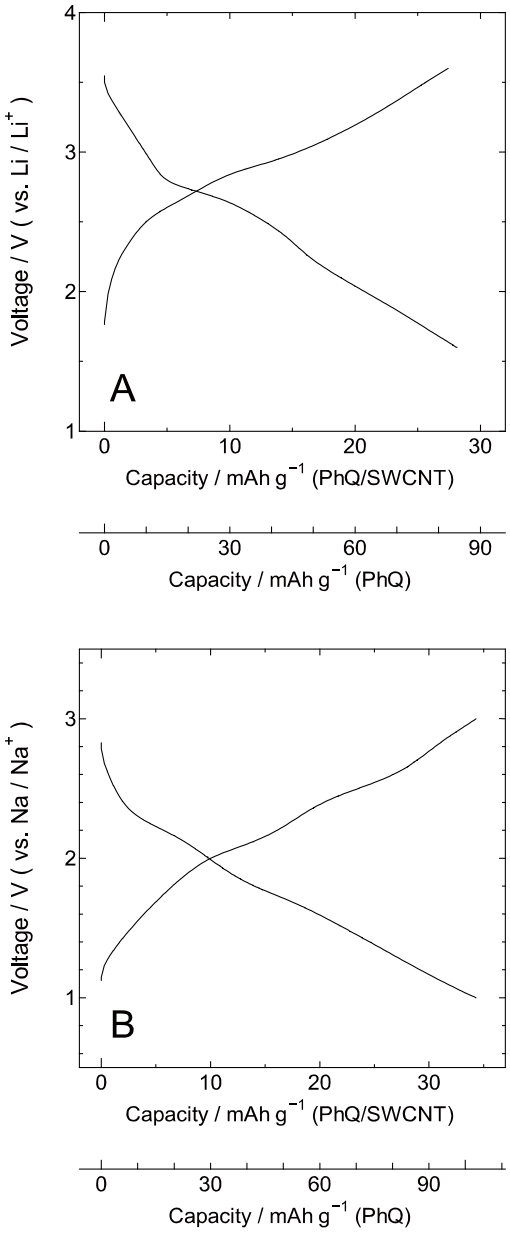

Fig. 4. 15: Galvanostatic charge-discharge curves of PhQ/SWCNT-2.5 used for (A) LIB and (B) SIB. The measurements were performed at 0°C and a constant current density of 100mA/g, where "g" means total weight of the composite electrode (PhQ/SWCNT-2.5).

Interestingly, the low temperature performance of PhQ/SWCNT electrodes is very good. The present commercial LIB using intercalation reactions shows a reduction in its cell performance at low temperature. The redox reactions of quinone molecules would not be affected very much by decreasing temperature. Figs. 4.15(A) and 4.15(B) show Li and Na ion charge-discharge curves of PhQ/SWCNT-2.5 at 0°C. As shown in Figs. 4.15(A) and 4.15(B), although the reversible capacities of PhQ/SWCNT-2.5 for both Li and Na ions are about 60% of the values observed at the room temperature (RT), almost the same charge-discharge profiles are kept at low temperature, except for slight increases in the charge-discharge hysteresis. This indicates that ion adsorbing sites are kept at low temperature while the activation energy for ion adsorption depends on temperature. This profile change at low temperature looks quite like the change with the increase in charging rate. Both profile changes can be explained by the increase in the over-potential for ion adsorption due to iR drop. Of course, the increase in the current and internal resistance lead to the larger hysteresis with the increase in the charging rate and the decrease in temperature, respectively. Although the increase in the internal resistance at low temperature should be related to various reasons, the change in ion mobility would be the main reason. In the case of PhQ@SWCNT encapsulation electrode, ion diffusion into the inner tube space of SWCNTs is necessarily for ion adsorption to occur. On the other hand, PhQ/SWCNT-2.5 does not require the diffusion process because PhQs are attached to the outer surface of the SWCNT bundle. That would be the reason for the better low-temperature performance.

I also performed DFT calculation to discuss the electrode properties of PhQ/SWCNT-2.5. It is well known that the open circuit voltage of a battery can be predicted by DFT calculations [80-84]. This approach is applicable to the present quinone electrode batteries. I denote the quinone electrode by Qsolid. The total reaction of quinone battery can be expressed as follows.

$$Q_{solid} + 2Li_{solid} \rightarrow Li_2Q_{solid} \quad (4.1)$$

Therefore, the open circuit voltage (electromotive force) E can be calculated by the following equation.

$$E = -\frac{\mathrm{G(Li_2Q_{solid})} - \mathrm{G(Q_{solid})} - 2\mathrm{G(Li_{solid})}}{2\mathrm{F}} \quad (4.2)$$

Where G(M) expresses the Gibbs free energy of M, and F denotes Faraday constant.

However, it is very difficult to discuss Gibbs free energy of PhQ/SWCNT-2.5, because the exact structure of PhQ/SWCNT-2.5 is not known. However, it would be meaningful to calculate the free energy difference ΔG of molecular entities in reactions (4.3) and (4.4) below, instead of calculating ΔG for the undefined solid-state structures in equation (4.2).

$$\mathrm{PhQ + Li^+ + e^- \rightarrow LiPhQ} \quad (4.3)$$

$$\mathrm{LiPhQ + Li^+ + e^- \rightarrow Li_2PhQ} \quad (4.4)$$

In this case, however, it is very hard to perform quantitative comparison between the calculated values and experimentally observed data. Furthermore, it should be noted that equation (4.2) can predict the open circuit voltage, while kinetic parameters should be considered when discussing discharge potentials. In this paper, I calculated molecular base reaction energies such as (4.3) and (4.4) for several combinations of electrode molecules (AQ and PhQ) and electrolyte ions (Li and Na) to gain a qualitative insight into the observed discharge potentials. The values of Gibbs free energy obtained by the DFT calculation are summarized in Table 4.1.

Tab. 4. 1: Gibbs free energies obtained by the DFT calculations.

	G / Hartree particle^{-1}		G / Hartree particle^{-1}
AQ	-688.7	LiPhQ	-696.3
LiAQ	-696.2	Li_2PhQ	-703.9
Li_2AQ	-703.8	NaPhQ	-851.1
NaAQ	-851.0	Na_2PhQ	-1013.4
Na_2AQ	-1013.4	Li	-7.3
PhQ	-688.7	Na	-162.1

First, I discuss the very different charge-discharge profiles of AQ and PhQ, although these two molecules have the same chemical formula. AQ and PhQ show one-step and two-step plateau discharge curves, respectively (see Fig. 4.15 and 9).

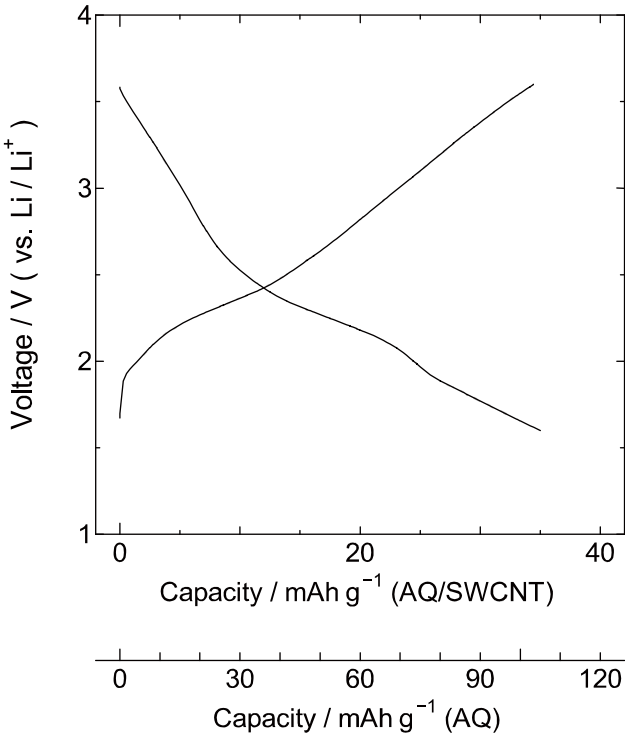

Fig. 4. 16: Room temperature charge-discharge curves of AQ/SWCNT-2.5 used for LIB. The measurement was performed at a constant current density of 100mA/g, where "g" means total weight of the composite electrode.

For PhQ, the difference between the two ΔG values for reaction (4.3) and (4.4) is quite large for both Li and Na. On the other hand, the difference for AQ is very small. Namely, AQ can adsorb the second Li or Na ion very easily after capturing the first ion, while PhQ requires relatively high energy to catch the second ion, probably due to the repulsion between adsorbed alkaline ions (Fig. 4.17).

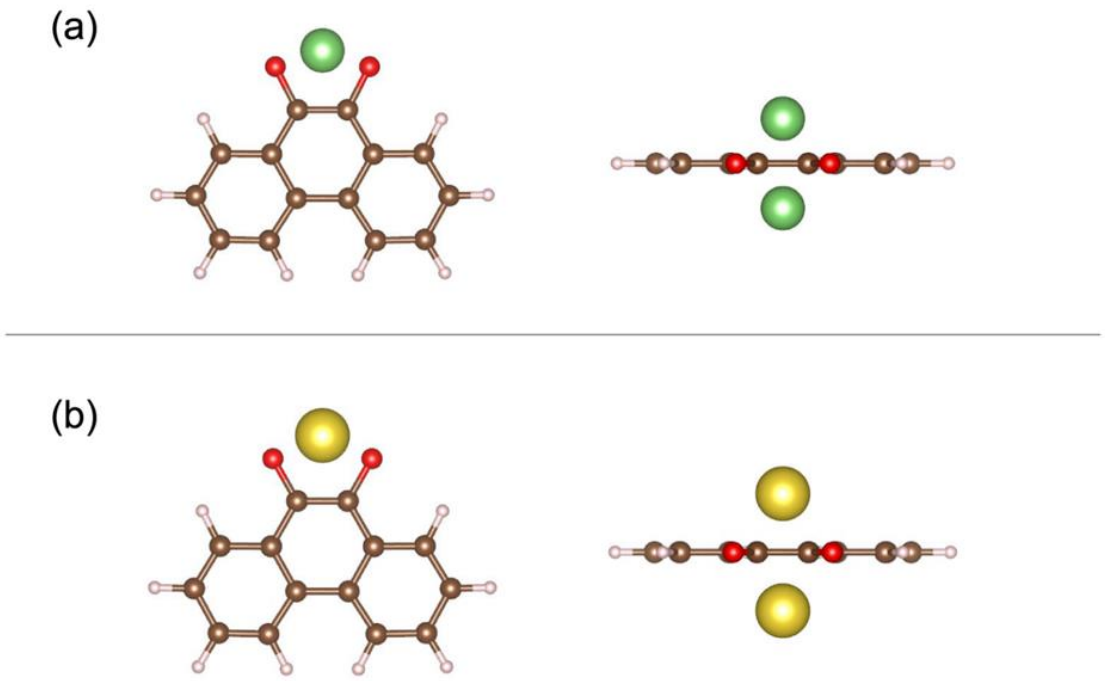

Fig. 4. 17: Molecular structure of (a) Li_2PhQ and (b) Na_2PhQ obtained by DFT calculations. (C: brown; O: red; H: white; Li: green; Na: yellow)

Next, I compare the discharge potentials of PhQ/SWCNT-2.5 for Li and Na ions. As discussed in the previous paragraph, it was found that the discharge potential for Na ion is about 700 mV lower than that for Li ion. Of course, I should consider the kinetic parameters. However, it is well known that Na ion has smaller solvation energy and larger ion mobility than Li ion has. So, if the discharge potential difference is caused by kinetic effects, the potential for Li ion should be lower. Therefore, I should think about another reason. According to our calculations, the stabilization energies of the reaction products (LiPhQ and Li_2PhQ) are larger than those of NaPhQ and Na_2PhQ, probably because Li should have stronger covalent bond with PhQ than Na. The stabilization energy difference would lead to the observed discharge potential difference.

Finally, I discuss the discharge profiles of PhQ/SWCNT-2.5. The discharge profiles of PhQ/SWCNT-2.5 show two step plateaus similar to those of PhQ bulk crystal and PhQ@SWCNT samples. However, the plateaus of PhQ/SWCNT-2.5 are not very flat compared to other PhQ samples. In the cases of PhQ bulk crystal and PhQ@SWCNT samples, all the PhQ molecules are equivalent and the discharge potentials should be determined by reaction (4.3) or (4.4). However, PhQ molecules in PhQ/SWCNT-2.5 form a variety of polymers and are therefore not equivalent. Each molecule should have slightly different redox potential from the values determined by (4.3) or (4.4). Therefore, PhQ/SWCNT-2.5 should have a non-flat plateau in the discharge profile.

4.4 Conclusion

In conclusion, I prepared AQ and PhQ derivatives having amino groups and grafted quinone molecules onto SWCNTs by diazo coupling reactions. The coupling reactions introduced bonds not only between quinone molecule and SWCNT, but also between the quinone molecules themselves. Consequently, polymerized quinone molecules were connected to SWCNTs. The structural details of PhQ/SWCNT-2.5 sample were analysed by XRD and Raman measurements. It was discussed that a few nanometres thick layer of polymerized PhQs covered the outside of SWCNT bundles. The obtained PhQ/SWCNT-2.5 work very well as LIB and SIB electrodes not only at RT but also at 0°C. It should be noted that the cycle performance of PhQ/SWCNT-2.5 electrode is much better than PhQ@SWCNT encapsulation electrode. I also calculated the molecular base reaction energies by DFT calculations to offer a qualitative insight into the factors influencing the observed discharge potentials of PhQ/SWCNT-2.5 electrode.

Chapter 5

Safe, economical and fast-charging secondary batteries using single-walled carbon nanotubes

5.1 Overview

I propose a new secondary battery having the following three specifications to solve the three problems mentioned above in chapter 1 (Fig. 5.1): (i) The new battery uses alkali metal halide aqueous electrolytes instead of the flammable organic electrolytes used in LIBs. The use of aqueous electrolytes is not only much safer than organic electrolytes, but also advantageous to cost and fast-charging, because alkali metal halides such as NaCl, LiCl, NaI consist only of abundant elements, and the ion mobilities of both alkali metal ions and halogen ions in water are much faster than those in organic electrolytes. (ii) As a negative electrode in the new battery, I use quinone molecules. (iii) Empty SWCNTs are used as a positive electrode. Halogen ions are oxidized inside the empty SWCNTs and caught as a form of diatomic molecule inside SWCNTs. The redox reactions of halogen ions inside SWCNTs are much faster than the intercalation reaction in LIBs. By combining (i)-(iii), a safe, economical and fast-charging secondary battery developed.

The above-mentioned electrode reactions (ii) and (iii) are explained in the chapter 2 and chapter 3 as follows. I chose iodide ion redox reaction as the positive electrode reaction. Chapter 2 reported that diatomic iodine molecules (I_2) are effectively encapsulated in SWCNTs by oxidizing iodide ions (I^-) at SWCNT electrode. I succeeded in preparing electrolyte redox capacitor using the redox reaction of iodide ions in SWCNTs. In this chapter, I use the similar electrode reaction as the electrolyte redox capacitor. On the other hand, Chapter 3 and chapter 4 reported that AQ and PhQ encapsulated in SWCNTs (AQ@SWCNT and PhQ@SWCNT) work as LIB electrodes.

Namely, AQ@SWCNT and PhQ@SWCNT can catch/release Li ions reversibly in LIB electrolyte. Here, I investigate whether or not those two molecules can work in aqueous electrolyte. If either molecule can work, I can develop the safe, economical and fast-charging secondary battery by combining the quinone electrode and the iodine electrode.

The energy density of the new aqueous electrolyte battery using AQ or PhQ as quinone electrode is estimated to be about 50 Wh/kg which is much smaller than that of LIBs, because the EMF obtained by the combinations of the quinone electrode and iodine electrode would be very small (< 0.5 V). However, I can improve the energy density of the new battery by developing new quinone molecules which have lower redox potentials than AQ and PhQ. Then, the expected energy density of the safe, economical and fast-charging aqueous electrolyte battery would be comparable to that of the LIBs tuned for high power usage.

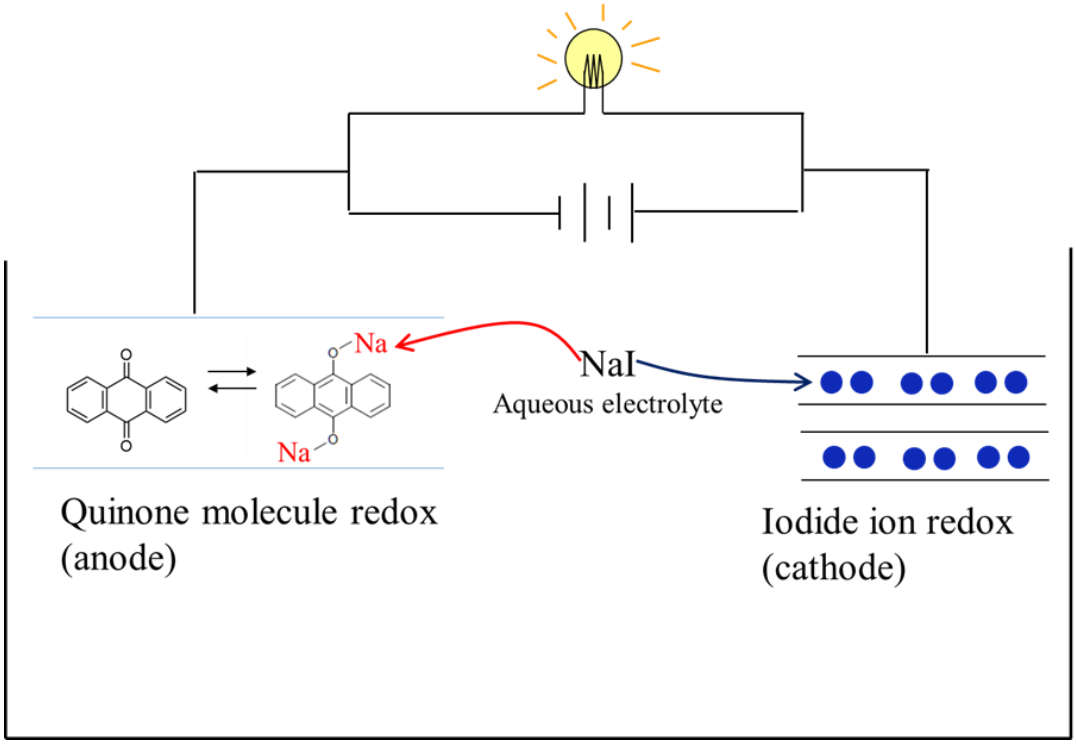

Fig. 5. 1: Schematic picture of new concept aqueous electrolyte secondary battery

5.2 Experimental methods

I used a SWCNT-2.5 and reagent-grade AQ and PhQ powder samples were purchased from Wako Pure Chemical Industries. SWCNT and quinone (AQ or PhQ) powder samples were sealed in a vacuum glass tube, and heated at 200℃ for 10 h. During that time, quinone molecules were sublimed and introduced into SWCNTs. After the heat treatment, the recovered samples were washed with organic solvents (N,N-dimethylformamide for AQ, acetone for PhQ) to remove any excess quinones deposited on the outer surface of the SWCNTs. Self-supported films (buckypaper) were obtained in this step.

The nanostructure of the obtained samples was observed using a transmission electron microscope (TEM; JEOL JEM-z2500) operated at 100 kV, and a scanning electron microscope (SEM; JEOL JSM-6010LA) operated at 10 kV. Fourier transform infrared (FTIR) spectra were measured by means of a spectrometer (JASCO, FT/IR-6300) using the attenuated total reflection (ATR) method. A ZnSe single crystal was used for the ATR measurement. Raman spectrum measurements were performed using a JASCO NRS-3300 spectrometer equipped with a 532 nm-wave length laser source. Synchrotron powder X-ray diffraction measurements were performed using the beam line BL-18C at the photon factory (PF) in High-Energy Accelerator Research Organization (KEK), Tsukuba, Japan. The X-ray beam was monochromatized by a Si(111) double crystal monochromator and collimated by a pinhole collimator of 100 mm in diameter. In the measurements, the incident X-ray wavelength was set to λ = 0.0614 nm (20 keV).

The electrochemical measurements were performed using a potentiostat/galvanostat (Autolab PGSTAT) in a three electrodes cell. AQ@SWCNT or PhQ@SWCNT samples (anodes) were paired with an empty SWCNT electrode (cathode). For CV measurements, I used Ag/AgCl reference electrode. Aqueous

electrolytes of 1 mol/L LiI or NaI were used. All the measurements were performed at room temperature.

5.3 Results and discussion

The encapsulation of AQ, PhQ molecules in SWCNTs has previously been confirmed not only by TEM observation but also by other spectroscopic measurements such as FT-IR, XRD, XPS and other measurement techniques in chapter 3. The observed data are shown in chapter 3 [34]. The content of encapsulated molecules per SWCNT weight was determined by TG measurements, and found to be 50.0 and 38.0 wt% for AQ and PhQ molecules, respectively.

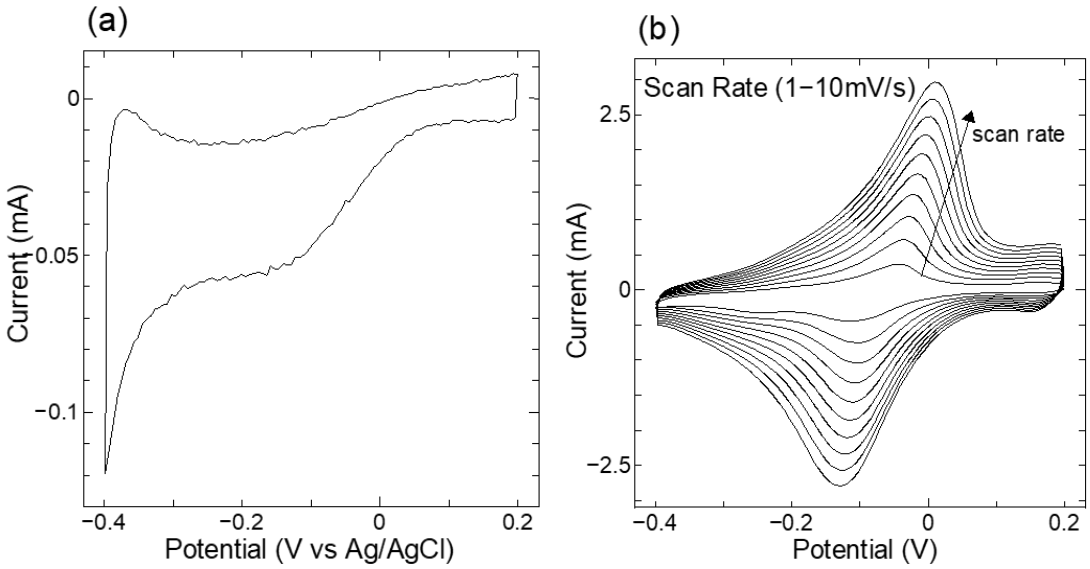

Fig. 5. 2: CV curves of (a) AQ@SWCNT measured at a scan rate of 1 mV/s and (b) PhQ@SWCNT measured at scan rates of 1-10 mV/s in LiI aqueous electrolyte.

Fig. 5.2 shows the cyclic voltammograms (CVs) of AQ@SWCNT and PhQ@SWCNT measured in LiI aqueous electrolyte. The measurements were done to judge whether these quinone molecules can catch/release alkali metal ions reversibly in aqueous electrolyte within the potential window of water. In the case of AQ@SWCNT (Fig. 5.2 (a), sweep rate: 1 mV/s), hydrogen evolution peak profile overlaps with the

tail of reduction peak corresponding to Li ion addition to AQ. Therefore, AQ molecule is not appropriate for the proposed battery shown in Fig. 5.1. On the other hand, reversible reduction/oxidation peaks were observed for PhQ molecule as shown in Fig. 5.2 (b). Since the peak current values for the reduction (Li ion addition) and oxidation (Li ion removal) are almost the same regardless of the potential sweep rate, the reversibility of PhQ electrode is quite high. However, I should think about the partial irreversibility of the process because the peak separation between reduction and oxidation potentials increases with increasing sweep rate. The remaining measurements were performed only for the PhQ@SWCNT electrode.

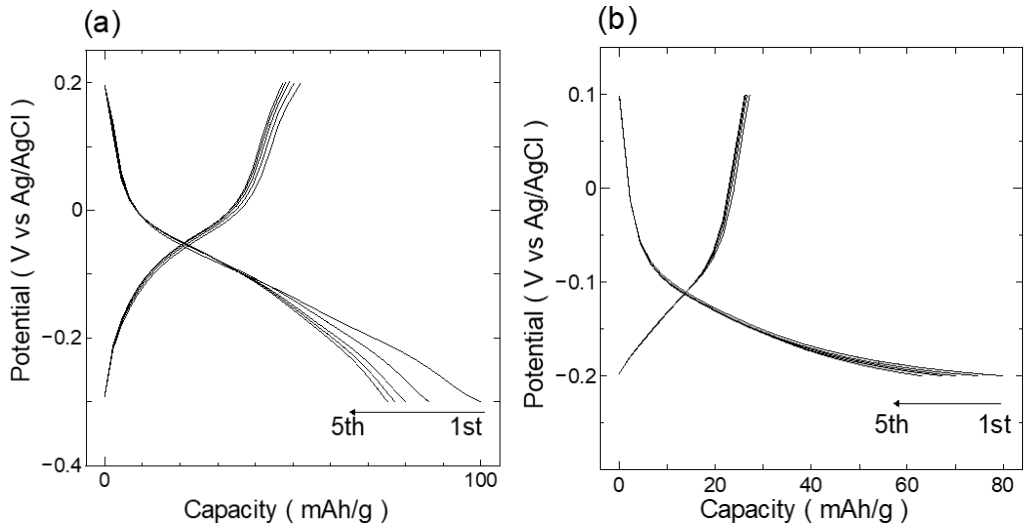

Fig. 5. 3: Charge/discharge curves of (a) AQ@SWCNT and (b) PhQ@SWCNT in LiI aqueous electrolyte. Five cycle charge/discharge data are shown.

Using LiI aqueous electrolyte, Li ion charge/discharge curves (chronopotentiograms) were observed for PhQ@SWCNT electrode (Fig. 5.3 (a)). The capacity value (mAh/g) in Fig. 5.3 (a) was calculated based on the weight of the encapsulated PhQ molecules. Assuming that two Li ions are caught by one PhQ molecule, the capacity limit of PhQ electrode is calculated to be 258 mAh/g. Compared to the calculated value, the observed reversible capacity (ca. 50 mAh/g) is quite small. In the case of organic electrolyte, it was observed that PhQ@SWCNT can store Li ions as much as the calculated value. One possible explanation for such a small reversible

capacity in aqueous electrolyte is that the aqueous electrolyte does not easily penetrate inside SWCNTs because of the hydrophobic nature of SWCNTs. It should be noted that PhQ@SWCNT electrode showed a two-step discharge potential plateau in organic electrolyte, while one plateau was observed in aqueous electrolyte. The two-step plateau observed in organic electrolyte is probably due to the redox potential difference of two oxygen atoms of PhQ molecule. On the other hand, only one plateau was observed in aqueous electrolyte. If only one of the two oxygen atoms of PhQ molecule worked to catch Li ion in aqueous electrolyte, the observed one-step plateau and small capacity could be explained. Large irreversible capacity and large capacity decrease in the few initial cycles were also observed in the present aqueous electrolyte experiments. The unstable phenomena would be caused by dissociation of the encapsulated PhQ molecules.

I also performed chronopotentiometry for PhQ@SWCNT electrode in NaI aqueous electrolyte. The observed Na ion charge/dis-charge curves are basically similar to the Li ion curves. However, the observed discharge potential for Na ion is about 0.1 V lower than that for Li ion. The cathode reaction of the proposed battery (Fig. 5.1) is the redox reaction of iodide ions, and the redox potential of I^-/I^2 is about +0.45 V vs. Ag/AgCl [85]. Therefore, a lower redox potential of the quinone anode is better to obtain higher EMF from the proposed battery. Namely, NaI electrolyte is better than LiI electrolyte in terms of the potential. On the other hand, the reversible capacity measured with NaI is smaller than that with LiI. As mentioned above, the discharge potential for NaI is lower than that for LiI, which indicates that PhQ molecule attached to Na ion (PhQ-Na) is chemically more active than PhQ-Li. The instability of PhQ-Na causes the dissociation of PhQ-Na from the electrode and leads to the large irreversible capacity and small reversible capacity observed.

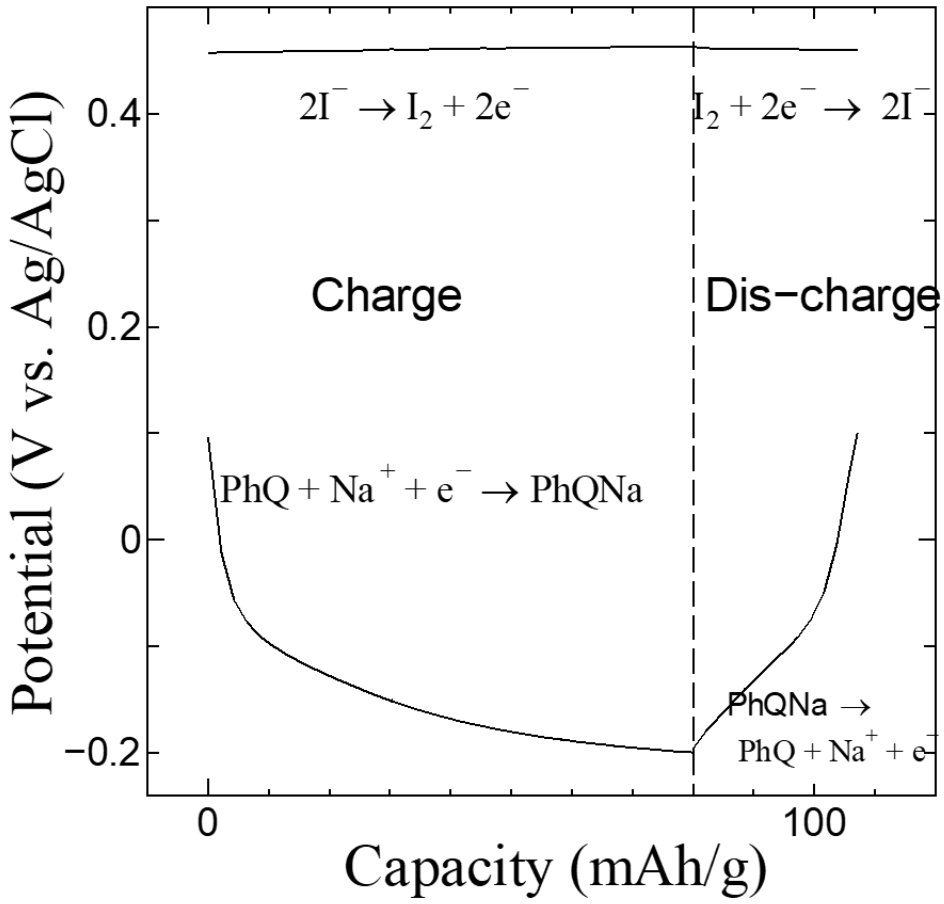

Fig. 5. 4: Charge/discharge curves of the anode and cathode, measured in NaI aqueous electrolyte.

Fig. 5.4 shows the potential changes for both the anode and cathode during charge/discharge measurements. As shown in Fig. 5.4, the cathode potential was kept at iodine redox potential. It has already been discussed in chapter 2 that the redox reaction of iodide ions in SWCNTs occurs very effectively and that the formed I_2 molecules are firmly kept inside SWCNTs. In the chapter 2, I used alkali metal ion physisorption, in other words electric double layer formation, as the anode reaction. Instead of the physisorption, PhQ redox reaction is used in the present study. By using the redox reaction, the energy density of the cell was greatly improved compared to the previous case.

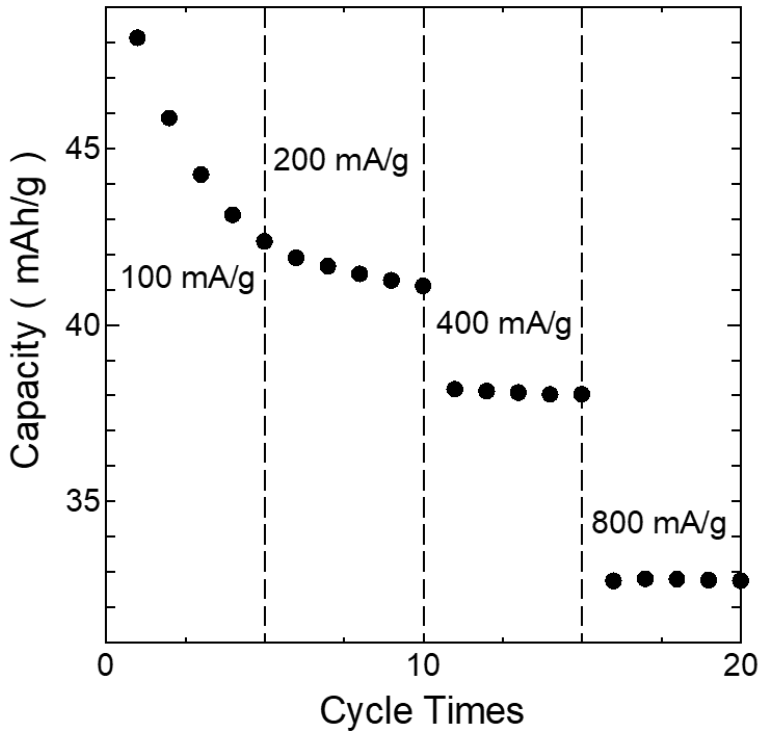

Fig. 5. 5: Reversible capacity values of PhQ@SWCNT electrode in NaI aqueous electrolyte, measured at current densities of 100, 200, 400, and 800 mA/g.

Fig. 5.5 summarizes the cycle and rate performance of the proposed battery (Fig. 5.1) in NaI aqueous electrolyte. In the few initial cycles, the capacity greatly decreased with cycle number, probably due to the dissociation of PhQ molecules. However, the capacity decrease became smaller after five cycles. It means that the cycle performance should be greatly improved if the initial dissociation of PhQ molecules could be reduced.

5.4 Conclusions

In summary, I developed a new concept aqueous electrolyte secondary battery by combining redox reactions of iodide ions in single-walled carbon nanotubes (SWCNTs) and alkali metal ions with quinone molecules. Both electrode reactions were investigated by CV and charge/discharge experiments in LiI and NaI aqueous electrolytes.

Chapter 6

Conclusion

In chapter 2, polyiodide ion formation in SWCNTs at low temperature is investigated and the obtained results are summarized as follows. First, I_2 molecules are encapsulated in SWCNTs and they start to aggregate by inter-molecular interactions. Charge-transfer from SWCNTs to the aggregated I_2 molecules adsorbed on the inner surface of SWCNTs produces polyiodide ions. At low temperature, the aggregation and polyiodide ion formation are promoted because the formation reaction is exothermic. The polyiodide ions, on the whole, would have a chain-like structure along to the hollow core of SWCNTs while the microscopic structures of the polyiodide ions should be written as small units (e.g. I_3^-, I_5^-, I_7^-).

An electrolyte redox electrochemical capacitor (EREC) using the redox reaction of bromide ions in single-walled carbon nanotubes (SWCNTs) was demonstrated. I was able to increase the cell voltage of Br EREC up to about 1.5 V without oxygen evolution. The energy density of EREC was greatly improved by using the redox reaction of bromide ions instead of iodide ions used in a previous work. It was found by monitoring the capacity retention, that SWCNT electrode can firmly hold the inserted Br molecules. I also investigated the structure and insertion site of the Br molecules inserted in SWCNTs by Raman and XRD measurements. Raman measurements revealed the existence of $(Br_2)_n$ chain-like molecule and Br_3^- ions. The Br molecules are likely to be inserted into the triangular lattice space of SWCNT bundles, because the diffraction lines of SWCNT bundle structure disappeared after the Br insertion.

In chapter 3, I have performed Li and Na ion charge–discharge experiments of PhQ molecules encapsulated in SWCNT-1.5 and -2.5, at RT and 0°C. In order to understand the manner at which PhQ molecules are stabilized in SWCNTs, I investigated the threshold temperature of sublimation of PhQ molecules encapsulated

in SWCNTs by TG measurements. It was found that the threshold temperature of PhQs in SWCNT-1.5 is higher than that of PhQs in SWCNT-2.5. It was also found by analysis of the Raman G-band peak profiles that charge transfer from metallic SWCNTs to PhQ molecules should occur in the case of SWCNT-1.5. The electrostatic interaction between charged SWCNTs and PhQ molecules, induced by the charge-transfer reaction, would partly contribute to the stabilization of PhQ molecules in SWCNTs. For Li-ion charge–discharge experiments, the observed reversible capacity of PhQ@SWCNT-1.5 was almost as high as the theoretical capacity of the PhQ molecules, while that of PhQ@SWCNT-2.5 was about half of the theoretical capacity. On the other hand, the two samples showed similar behaviour for Na ion storage. Since the Na ion reversible capacity of PhQ@SWCNT-2.5 measured at 0°C remained as high as that measured at RT, PhQ@SWCNT-2.5 should be an interesting candidate as an electrode material for a low temperature Na ion battery.

In chapter 4, I prepared AQ and PhQ derivatives having amino groups and grafted quinone molecules onto SWCNTs by diazo coupling reactions. The coupling reactions introduced bonds not only between quinone molecule and SWCNT, but also between the quinone molecules themselves. Consequently, polymerized quinone molecules were connected to SWCNTs. The structural details of PhQ/SWCNT-2.5 sample were analysed by XRD and Raman measurements. It was discussed that a few nanometres thick layer of polymerized PhQs covered the outside of SWCNT bundles. The obtained PhQ/SWCNT-2.5 work very well as LIB and SIB electrodes not only at RT but also at 0°C. It should be noted that the cycle performance of PhQ/SWCNT-2.5 electrode is much better than PhQ@SWCNT encapsulation electrode. I also calculated the molecular base reaction energies by DFT calculations to offer a qualitative insight into the factors influencing the observed discharge potentials of PhQ/SWCNT-2.5 electrode.

In chapter 5, I developed a new concept aqueous electrolyte secondary battery by combining redox reactions of iodide ions in single-walled carbon nanotubes (SWCNTs)

and alkali metal ions with quinone molecules. Both electrode reactions were investigated by CV and charge/discharge experiments in LiI and NaI aqueous electrolytes.

List of Publication

1. **Canghao Li**, Yosuke Ishii, Shunya Inayama and Shinji Kawasaki. Quinone molecules encapsulated in SWCNTs for low-temperature Na ion batteries, Nanotechnology, 2017, 28, 355401.
2. **Canghao Li**, Yosuke Ishii, and Shinji Kawasaki. Safe, economical and fast-charging secondary batteries using single-walled carbon nanotubes, Japanese Journal of Applied Physics, accepted.
3. **Canghao Li**, Yukihiro Yoshida, Remi Date, Kazuki Matsushita, Yosuke Ishii, and Shinji Kawasaki. Bromine aqueous electrolyte redox capacitor using carbon nanotube, Materials Express, accepted.
4. **Li, Canghao**, Nakamura Motoumi, Inayama Shunya, Ishii Yosuke, Kawasaki Shinji, Al-zubaidi Ayar, Sagisaka Kento, Hattori Yoshiyuki. Alkali Metal Ion Storage of Quinone Molecules Grafted on Single-walled Carbon Nanotubes at Low Temperature, J. Am. Chem. Soc. Omega, accepted.
5. Yukihiro Yoshida, Yosuke Ishii, Nao Kato, **Canghao Li**, and Shinji Kawasaki. Low-Temperature Phase Transformation Accompanied with Charge-Transfer Reaction of Polyiodide Ions Encapsulated in Single-Walled Carbon Nanotubes, J. Phys. Chem. C, 2016, 120, 20454−20461.

Reference:

[1] Tae Hoon Hwang, Yong Min Lee, et al., Electrospun Core–Shell Fibers for Robust Silicon Nanoparticle-Based Lithium Ion Battery Anodes. Nano Lett., 2012, 12 (2): 802–807.
[2] Dunn B, Kamath H, Tarascon J M., Electrical energy storage for the grid: a battery of choices. Science, 2011, 334(6058): 928-935.
[3] Liu C, Li F, Ma L P, et al., Advanced materials for energy storage. Advanced materials, 2010, 22(8): E28-E62.
[4] Scrosati, B.; Garche, J., Lithium batteries: Status, prospects and future. J. Power Sources, 2010, 195 (9): 2419-2430.
[5] Etacheri V., Marom R., et al., Challenges in the development of advanced Li-ion batteries: a review. Energy Environ. Sci., 2011, 4 (9): 3243-3262.
[6] Dunn B., Kamath H., Tarascon J. M., Electrical Energy Storage for the Grid: A Battery of Choices. Science, 2011, 334 (6058): 928-935.
[7] Scrosati B., Lithium rocking chair batteries: An old concept?. Journal of The Electrochemical Society, 1992, 139(10): 2776-2781.
[8] Tarascon J. M., Armand M., Issues and challenges facing rechargeable lithium batteries//Materials for Sustainable Energy: A Collection of Peer-Reviewed Research and Review Articles from Nature Publishing Group. 2011: 171-179.
[9] Bruce P G, Scrosati B, Tarascon J M. Nanomaterials for rechargeable lithium batteries. Angewandte Chemie International Edition, 2008, 47(16): 2930-2946.
[10] Norton J J. Lithium, cesium, and rubidium–the rare alkali metals. United States mineral resources: US Geological Survey Professional Paper, 1973, 820: 365-378.
[11] Palomares V., Serras P., Villaluenga I., et al., Na-ion batteries, recent advances and present challenges to become low cost energy storage systems. Energy & Environmental Science, 2012, 5(3): 5884-5901.
[12] Kim S. W., Seo D. H., Ma X., et al., Electrode materials for rechargeable sodium‐ion batteries: potential alternatives to current lithium‐ion batteries. Advanced Energy Materials, 2012, 2(7): 710-721.
[13] Slater M. D., Kim D., Lee E., et al., Sodium‐ion batteries. Advanced Functional Materials, 2013, 23(8): 947-958.
[14] Conway B. E., Electrochemical supercapacitors: scientific fundamentals and technological applications. Springer Science & Business Media, 2013.
[15] Yao M., Senoh H., Yamazaki S., et al., High-capacity organic positive-electrode material based on a benzoquinone derivative for use in rechargeable lithium batteries. Journal of Power Sources, 2010, 195(24): 8336-8340.
[16] Frackowiak E., Khomenko V., Jurewicz K., et al., Supercapacitors based on conducting polymers/nanotubes composites. Journal of Power Sources, 2006, 153(2): 413-418.
[17] Liang Y., Tao Z., Chen J., Organic electrode materials for rechargeable lithium batteries. Advanced Energy Materials, 2012, 2(7): 742-769.

[18] Li L., Jeon M., Kim S. Y., Synthesis, characterization and ethylene polymerisation of 9, 10-phenanthrenequinone-based nickel (II)-α-diimine complexes. Journal of Molecular Catalysis A: Chemical, 2009, 303(1): 110-116.
[19] Wu Y., Zeng R., Nan J., et al., Quinone electrode materials for rechargeable lithium/sodium ion batteries. Advanced Energy Materials, 2017, 7(24): 1700278.
[20] Dresselhaus G., Riichiro S., Physical properties of carbon nanotubes. World Scientific, 1998.
[21] Han J., Structures and properties of carbon nanotubes//Carbon nanotubes. CRC Press, 2004: 16-45.
[22] Dresselhaus M. S., Dresselhaus G., Saito R., Physics of carbon nanotubes. Carbon, 1995, 33(7): 883-891.
[23] Smith B. W., Monthioux M., Luzzi D. E., Encapsulated C_{60} in carbon nanotubes. Nature, 1998, 396(6709): 323.
[24] Maniwa Y., Kataura H., Abe M., et al., Phase transition in confined water inside carbon nanotubes. Journal of the Physical Society of Japan, 2002, 71(12): 2863-2866.
[25] Takenobu T., Takano T., Shiraishi M., et al., Stable and controlled amphoteric doping by encapsulation of organic molecules inside carbon nanotubes. Nature materials, 2003, 2(10): 683.
[26] Yanagi K., Miyata Y., Kataura H., Highly Stabilized β‐Carotene in Carbon Nanotubes. Advanced Materials, 2006, 18(4): 437-441.
[27] Sakane Y., Mouri K., Shintani K., Morphology of a columnar stack of coronene molecules encapsulated in a single-walled carbon nanotube. AIP Advances, 2015, 5(11): 117113.
[28] Kawasaki S., Iwai Y., Hirose M., Electrochemical lithium ion storage properties of single-walled carbon nanotubes containing organic molecules. Carbon, 2009, 47(4): 1081-1086.
[29] Song H., Ishii Y., Al-zubaidi A., et al., Temperature-dependent water solubility of iodine-doped single-walled carbon nanotubes prepared using an electrochemical method. Physical Chemistry Chemical Physics, 2013, 15(16): 5767-5770.
[30] Taniguchi Y., Ishii Y., Al-Zubaidi A., et al., New type of pseudo-capacitor using redox reaction of electrolyte in single-walled carbon nanotubes. Journal of Nanoscience and Nanotechnology, 2017, 17(3): 1901-1907.
[31] Fujimori T., Morelos-Gómez A., Zhu Z., et al., Conducting linear chains of sulphur inside carbon nanotubes. Nature communications, 2013, 4: 2162.
[32] Xu J., Guan L., Toward understanding the active site for oxygen reduction reaction on phosphorus-encapsulated single-walled carbon nanotubes. Rsc Advances, 2013, 3(16): 5577-5582.
[33] Yudasaka M., Ajima K., Suenaga K., et al., Nano-extraction and nano-condensation for C60 incorporation into single-wall carbon nanotubes in liquid phases. Chemical physics letters, 2003, 380(1-2): 42-46.
[34] Ishii Y., Tashiro K., Hosoe K., et al., Electrochemical lithium-ion storage properties of quinone molecules encapsulated in single-walled carbon nanotubes. Physical

Chemistry Chemical Physics, 2016, 18(15): 10411-10418.
[35] Ishii Y., Sakamoto Y., Song H., et al., Alkali metal ion storage properties of sulphur and phosphorous molecules encapsulated in nanometer size carbon cylindrical pores. AIP Advances, 2016, 6(3): 035112.
[36] H. Huang, C. Huang, C. Hsieh, H. Teng, Electric double layer capacitors of high volumetric energy based on ionic liquids and hierarchical-pore carbon, Journal of Materials Chemistry A, 2014, 2: 14963-14972.
[37] Z. Jiang, A. Al-Zubaidi, S. Kawasaki, Unusual increase in the electric double-layer capacitance with charge-discharge cycles of nitrogen doped single-walled carbon nanotubes, Materials Express, 2014, 4: 331-336.
[38] A. Al-zubaidi, Y. Ishii, et al., Spectroscopic evidence for the origin of the dumbbell cyclic voltammogram of single-walled carbon nanotubes, Phys. Chem. Chem. Phys., 2013, 15: 20672-20678.
[39] A. Al-zubaidi, T. Inoue, et al., Cyclic voltammogram profile of single-walled carbon nanotube electric double-layer capacitor electrode reveals dumbbell shape, J. Phys. Chem. C, 2012, 116: 7681-7686.
[40] A. Al-Zubaidi, T. Inoue, et al., Ion adsorption on the inner surface of single-walled carbon nanotubes used as electrodes for electric double-layer capacitors, Phys. Chem. Chem. Phys., 2012, 14: 16055-16061.
[41] Y.-T. Kim, K. Tadai and T. Mitani, Highly dispersed ruthenium oxide nanoparticles on carboxylated carbon nanotubes for supercapacitor electrode materials, J. Mater. Chem., 2005, 15: 4914-4921.
[42] Rinzler, A. G., et al., Large-Scale Purification of Single-Wall Carbon Nanotubes: Process, Product, and Characterization. Appl Phys A, 1998, 67, 29-37.
[43] Frisch, M. J., et al., Gaussian 09, Revision C.01, Gaussian, Inc.: Wallingford, CT, USA, 2009.
[44] Peterson, K. A., Figgen, D., et, al., Systematically Convergent Basis Sets with Relativistic Pseudopotentials. Ii. Small-Core Pseudopotentials and Correlation Consistent Basis Sets for the Post-D Group 16–18 Elements. J. Chem. Phys. 2003, 119: 11113-11123.
[45] Milnera M., Kürti J., Hulman M., Kuzmany H., Periodic Resonance Excitation and Intertube Interaction from Quasicontinuous Distributed Helicities in Single-Wall Carbon Nanotubes. Phys. Rev. Lett. 2000, 84: 1324-1327.
[46] Jorio A., Saito R., et al., Structural (N, M) Determination of Isolated Single-Wall Carbon Nanotubes by Resonant Raman Scattering. Phys. Rev. Lett. 2001, 86: 1118-1121.
[47] Dresselhaus M. S., Dresselhaus G., et al., Raman Spectroscopy of Carbon Nanotubes. Phys. Rep. 2005, 409: 47-99.
[48] Thess A., et al., Crystalline Ropes of Metallic Carbon Nanotubes. Science, 1996, 273: 483-487.
[49] Yoshida Y., Tsutsui M., Al-zubaidi A., Ishii Y., Kawasaki S., In Situ Synchrotron X-Ray Diffraction Studies of Single-Walled Carbon Nanotubes for Electric Double-

Layer Capacitors. J. Chem. Chem. Eng. 2015, 9: 509-513.
[50] Kataura H., Kumazawa Y., et al., Optical Properties of Single-Wall Carbon Nanotubes. Synth. Met. 1999, 103: 2555-2558.
[51] Brown S. D. M., Jorio A., et, al., Origin of the Breit-Wigner-Fano Lineshape of the Tangential G-Band Feature of Metallic Carbon Nanotubes. Phys. Rev. B 2001, 63: 155414.
[52] Corio P., Santos P. S., et al., Potential Dependent Surface Raman Spectroscopy of Single Wall Carbon Nanotube Films on Platinum Electrodes. Chem. Phys. Lett. 2003, 370: 675-682.
[53] Chan C. T., Ho K. M., Kamitakahara W. A., Zone-Center Phonon Frequencies for Graphite and Graphite Intercalation Compounds: Charge-Transfer and Intercalate-Coupling Effects. Phys. Rev. B 1987, 36: 3499-3502.
[54] Das A., Sood A. K., et al., Doping in Carbon Nanotubes Probed by Raman and Transport Measurements. Phys. Rev. Lett. 2007, 99: 136803.
[55] Tristant D., Puech P., Gerber I. C., Theoretical Study of Polyiodide Formation and Stability on Monolayer and Bilayer Graphene. Phys. Chem. Chem. Phys. 2015, 17: 30045-30051.
[56] Tristant D., Puech P., Gerber I. C., Theoretical Study of Graphene Doping Mechanism by Iodine Molecules. J. Phys. Chem. C 2015, 119, 12071-12078.
[57] Grigorian L., Williams K. A., et al., Reversible Intercalation of Charged Iodine Chains into Carbon Nanotube Ropes. Phys. Rev. Lett. 1998, 80: 5560-5563.
[58] Sharp S. B., Gellene G. I., Ab Initio Calculations of the Ground Electronic States of Polyiodide Anions. J. Phys. Chem. A 1997, 101: 2192-2197.
[59] Noltemeyer M., Saenger W., X-Ray Studies of Linear Polyiodide Chains in Alpha-Cyclodextrin Channels and a Model for the Starch-Iodine Complex. Nature 1976, 259: 629-632.
[60] Teitelbaum R. C., Ruby S. L., Marks T. J., A Resonance Raman/Iodine Moessbauer Investigation of the Starch-Iodine Structure. Aqueous Solution and Iodine Vapor Preparations. J. Am. Chem. Soc. 1980, 102: 3322-3328.
[61] Michel T., Alvarez L., et al., Exafs Investigations of Iodine-Doped Carbon Nanotubes. Phys. Rev. B 2006, 73: 195419.
[62] Takahashi Y., Kumano T., Nishikawa S., Crystal Structure of B-Amylose. Macromolecules 2004, 37: 6827-6832.
[63] Popov D., Buléon A., et al., Crystal Structure of a-Amylose: A Revisit from Synchrotron Microdiffraction Analysis of Single Crystals. Macromolecules 2009, 42: 1167-1174.
[64] Nishiyama Y., Putaux J., et al., B→A Allomorphic Transition in Native Starch and Amylose Spherocrystals Monitored by in Situ Synchrotron X-Ray Diffraction. Biomacromolecules 2010, 11: 76-87.
[65] Kong L., Lee C., et al., Characterization of Starch Polymorphic Structures Using Vibrational Sum Frequency Generation Spectroscopy. J. Phys. Chem. B 2014, 118: 1775-1783.

[66] Mulazzi E., Pollini I., et al., Selective Resonant Raman Enhancement in Polyiodide Chains. Phys. Rev. B 1981, 24: 3555-3563.
[67] A. L. Aguiar, E. B. Barros, et al., Pressure Tuning of Bromine Ionic States in Double-Walled Carbon Nanotubes, J. Phys. Chem. C, 2017, 121: 10609-10619.
[68] Y. Maniwa, Y. Kumazawa, et al., Anomaly of X-ray Diffraction Profile in Single-Walled Carbon Nanotubes, Jpn. J. Appl. Phys., 1999, 38, L668.
[69] J. Chmiola, G. Yushin, et al., Anomalous increase in carbon capacitance at pore sizes less than 1 nanometer, Science, 2006, 313: 1760-1763.
[70] Wang L, Yang C, Dou S, et al., Nitrogen-doped hierarchically porous carbon networks: synthesis and applications in lithium-ion battery, sodium-ion battery and zinc-air battery. Electrochimica Acta, 2016, 219: 592-603.
[71] Zhou Q., Liu L., Tan J., et al., Synthesis of lithium titanate nanorods as anode materials for lithium and sodium ion batteries with superior electrochemical performance. Journal of Power Sources, 2015, 283: 243-250.
[72] Zhou M., Xu Y., Xiang J., et al., Understanding the orderliness of atomic arrangement toward enhanced sodium storage. Advanced Energy Materials, 2016, 6(23): 1600448.
[73] Frisch M. J., Trucks G. W., et al., Gaussian 09, Revision C.01. Gaussian 09, Revision C.01 2009.
[74] Becke A. D., Density‐functional thermochemistry. III. The role of exact exchange. J. Chem. Phys. 1993, 98 (7): 5648-5652.
[75] Dunning T. H., Gaussian basis sets for use in correlated molecular calculations. I. The atoms boron through neon and hydrogen. J. Chem. Phys. 1989, 90 (2): 1007-1023.
[76] Lee M., Hong J., et al., Organic nanohybrids for fast and sustainable energy storage. Adv. Mater. 2014, 26 (16): 2558-65.
[77] Liang Y., Jing Y., et al., Universal quinone electrodes for long cycle life aqueous rechargeable batteries. Nat. Mater. 2017, 16: 841.
[78] Jaffe A., Saldivar Valdes A., Karunadasa H. I., Quinone-Functionalized Carbon Black Cathodes for Lithium Batteries with High Power Densities. Chem. Mater. 2015, 27 (10): 3568-3571.
[79] Huskinson B., Marshak M. P., et al., A metal-free organic–inorganic aqueous flow battery. Nature 2014, 505: 195.
[80] Reynolds Christopher A., Density functional calculation of quinone electrode potentials. International Journal of Quantum Chemistry 1995, 56 (6): 677-687.
[81] Namazian M., Density functional theory response to the calculation of electrode potentials of quinones in non-aqueous solution of acetonitrile. Journal of Molecular Structure: THEOCHEM 2003, 664-665, 273-278,
[82] Namazian M., Almodarresieh H. A., et al., DFT calculation of electrode potentials for substituted quinones in aqueous solution. Chem. Phys. Lett. 2004, 396 (4): 424-428.
[83] Yao M., Senoh H., et al., High-capacity organic positive-electrode material based on a benzoquinone derivative for use in rechargeable lithium batteries. J. Power Sources 2010, 195 (24): 8336-8340.

[84] Ding Y., Li Y., Yu G., Exploring Bio-inspired Quinone-Based Organic Redox Flow Batteries: A Combined Experimental and Computational Study. Chem 2016, 1 (5): 790-801.
[85] Zhao Y., Wang L., Byon H. R., High-performance rechargeable lithium-iodine batteries using triiodide/iodide redox couples in an aqueous cathode. Nature communications, 2013, 4: 1896.